APPLICATION-SPECIFIC OPTIMIZATION OF QUANTITATIVE SUSCEPTIBILITY MAPPING FOR CLINICAL IMAGING

A Dissertation

Presented to the Faculty of the Graduate School

of Cornell University

in Partial Fulfillment of the Requirements for the Degree of

Doctor of Philosophy

by

Alexey Victorovich Dimov

December 2017

APPLICATION-SPECIFIC OPTIMIZATION OF QUANTITATIVE SUSCEPTIBILITY MAPPING FOR CLINICAL IMAGING

Alexey Victorovich Dimov, Ph.D.

Cornell University 2017

Magnetic resonance imaging (MRI) is a noninvasive clinical imaging modality with very rich contrasts based on the physical properties of the imaged tissues. MRI can be used for quantification of volumetric distributions of various biomolecules and chemical elements - such as triglycerides, calcium and iron - that regarded as participants in normal tissue biochemistry, and whose dysregulations are often manifested in pathologic processes. This dissertation reports optimization steps undertaken to overcome technical challenges in quantitative susceptibility mapping (QSM) in different parts of human body.

Often in QSM it is assumed that susceptibility is the only contributor to the observed field inhomogeneity, which may be a valid assumption for neuroimaging applications. However, multiple molecules found in biological tissues (e.g., triglycerides of fat) have a resonance frequency different from that of water, and this resonance frequency offset is referred to as chemical shift. This chemical shift affects the phase of the MRI signal. Although ways to estimate field inhomogeneity in the presence of chemical shift have been proposed, they often rely on the a priori knowledge of the chemical spectrum. Unfortunately, variability of chemical spectra have been reported. In this dissertation, an automated joint estimation of the chemical shift and the susceptibility from an MRI dataset is reported, where the chemical shift is also treated as an unknown variable subject to optimization.

QSM may become a useful diagnostic tool for noninvasive assessment of bone health without the use of ionizing radiation, however this application has been a challenging task challenging because QSM requires complete measurements of phase everywhere within the region of interest, and cortical bone typically has very low or no signal at conventional echo times in gradient echo (GRE) imaging. An additional problem arises from intermingling of fat and water protons in the bone marrow, necessitating the application of waterfat separation techniques for field mapping. In this dissertation, a novel signal model is proposed, feasibility of using QSM for measuring bone MRI signal is investigated, and the inherent technical issues involved in this application are highlighted.

QSM has been widely applied in neuroimaging. In particular, due to its ability to accurately map iron deposits in deep brain nuclei, QSM promises precise targeting of the subthalamic nucleus (STN) in deep brain stimulation surgery (DBS). This dissertation reports results of comparison between QSM and standard-of-care T2w imaging of the STN, and their performance in high-resolution presugrical anatomic imaging.

BIOGRAPHICAL SKETCH

Alexey V. Dimov was born in Kirov, Russia in 1988. He received the Bachelor of Science degree in Physics (2009) and Master of Science degree in Radiophysics (2011) from N.I. Lobachevsky State University of Nizhny Novgorod. In the same year, he joined the graduate program in Biomedical Engineering at Cornell University, and received the Master of Science degree in Biomedical Engineering in 2014.

In memory of Nikolay Fyodorovich Goroshkin (1923-1944), Yevgeny Aleksandrovich Sadakov (1922-1944), and Ivan Lukich Boldakov (1915-1944).

ACKNOWLEDGEMENTS

First, I would like to thank my advisor and mentor Dr. Yi Wang for his invaluable lessons in rigorous and systematic scientific thinking. His expertise in the fields of physics and MR imaging combined with passion for technical and clinical research, his collaborative skills and receptiveness to new ideas greatly influenced my work and have allowed me to succeed in conducting original research.

I would also like to extend my gratitude to my two minor advisors, Prof. Peter Charles Doerschuk (Cornell Univeristy) and Dr. Martin Prince (Weill Cornell Medical College) for all their assistance throughout my graduate program. Prof. Doerschuks encouragement during my first year at Cornell together with his further advice on coursework and my PhD thesis were vital for my professional development. Martin Princes extensive knowledge of clinical and engineering aspects of MRI has greatly influenced my research, and his ability to recognize new problems and applications has been crucial to my work. I am grateful for his enthusiasm.

I am deeply grateful to Prof. Pascal Spincemaille for his constant guidance throughout my research. His knowledge in mathematics, physics, programming and scanner operating played an essential role in practical realization of my projects. I would also like to thank Prof. Spincemaille for all the discussions and brain stormings weve had over these years, his patience and kindness. I would like to thank Prof. Thanh Nguyen for his help in understanding of MR physics and concepts in pulse sequence design. I am also thankful for his valuable advices on scientific paper reviewing. I owe a special debt of gratitude to Tian Liu, PhD, for his mentoring and introduction to the area of magnetic susceptibility mapping. He was an inspirational figure, and his insight into the

field has greatly aided my work.

I would like to thank Huan Tan, PhD (University of Chicago) for providing clinical breast MRI data used in chemical QSM project, Prof. Jiang Du (University of California San Diego) for providing UTE sequence used in bone susceptibility project, Dr. Brian Harris Kopell and Dr. Jonathan Rasouli (Mount Sinai Health System, New York) for their collaboration and valuable insights on STN QSM project. My special gratitude goes to my colleague, Zhe Liu, for his willingness to assist in multiple experiments and volunteer in numerous rounds of MR data acquisition. I would like to thank, in no particular order, my other colleagues and friends who on many occasions provided valuable assistance, advices and feedback on my work: Jingwei Zhang, Cynthia Wisnieff, Mitch A. Cooper, Keigo Kawaji, Bo Xu, Dong Zhou, Carlo Salustri, Kofi Deh, Sarah Eskreis-Winkler, Yan Wen, Junghun Cho, Ramin Jafari, Youngwook Kee, Yan Zhang, Yihao Yao, Silvina Dutruel, Nanda Thimmappa, Carsten Stüber, Anna Varentsova and many others.

I would like to thank the Meinig School of Biomedical Engineering (Cornell University), and the Department of Radiology (Weill Cornell Medical College) for giving me the opportunity and other necessary means to join and complete the graduate program. I am grateful to Belinda Ann Floyd for her indispensable help in multitude of practical aspects of the graduate school from enrollment to graduation. I also thank Rebecca Cramer, Shannon Michel, Andrew J. Luzzi, and Kelly McCabe Gillen for all their tremendous work in the lab.

Finally, I would like to thank my parents, Natalya and Victor Dimov, my brother Alexander, and my girlfriend, Lina Mercedes Sanchez Botero, for their continuous support and encouragement through my graduate study.

TABLE OF CONTENTS

Biographical Sketch . . . iii
Dedication . . . iv
Acknowledgements . . . v
Table of Contents . . . vii
List of Tables . . . ix
List of Figures . . . x

1 Introduction **1**
1.1 Summary of contributions . . . 1

2 Background **4**
2.1 MRI physics . . . 4
2.1.1 Spin behavior in a magnetic field . . . 4
2.1.2 Bloch equation . . . 5
2.1.2.1 Precession . . . 5
2.1.2.2 Relaxation . . . 6
2.1.2.3 Excitation . . . 7
2.2 Signal detection . . . 8
2.3 Spatial encoding . . . 9
2.4 Sampling trajectories in k-space . . . 10
2.4.1 Cartesian sampling . . . 11
2.4.2 Radial sampling . . . 12
2.4.2.1 Basic structure . . . 13
2.4.2.2 Ultra-short TE imaging . . . 14
2.5 Image reconstruction . . . 14
2.5.1 Gridding reconstruction . . . 15
2.5.2 Parallel imaging . . . 16
2.6 Quantitative susceptibility mapping . . . 18
2.6.1 Susceptibility-induced magnetic fields . . . 18
2.6.2 Susceptibility mapping . . . 19
2.7 Chemical shift and water/fat separation . . . 21
2.7.1 Iterative decomposition of water and fat signals . . . 23

3 Joint estimation of chemical shift and quantitative susceptibility mapping **25**
3.1 Introduction . . . 26
3.2 Theory . . . 27
3.2.1 Challenges in previous attempts for estimating f_s . . . 28
3.3 Methods . . . 30
3.3.1 Iterative correction of the fat chemical shift . . . 30
3.3.2 Numerical phantom simulations . . . 34
3.3.3 Lard phantom experiment . . . 37

3.3.4 Bovine tissue experiment . . . 38
3.3.5 Volunteer breast scan . . . 39
3.3.6 Image processing and analysis . . . 39
3.4 Results . . . 40
3.4.1 Numerical experiments . . . 40
3.4.2 Lard phantom results . . . 42
3.4.3 Bovine tissue experiment results . . . 44
3.4.4 Volunteer breast scan . . . 46
3.5 Discussion . . . 49

4 Bone quantitative susceptibility mapping using a chemical species specific R_2^* signal model with ultrashort and conventional echo data 53
4.1 Introduction . . . 54
4.2 Theory . . . 55
4.3 Methods . . . 57
4.3.1 Pulse sequence . . . 57
4.3.2 Porcine specimen experiment . . . 57
4.3.3 Volunteer MR imaging . . . 59
4.3.4 Image processing and analysis . . . 59
4.4 Results . . . 61
4.4.1 Porcine phantom results . . . 61
4.4.2 Volunteer results . . . 62
4.5 Discussion . . . 66

5 High resolution QSM for functional and structural depiction of subthalamic nuclei in DBS pre-surgical mapping 71
5.1 Introduction . . . 72
5.2 Methods . . . 73
5.3 Results . . . 77
5.3.1 Healthy subjects study . . . 77
5.3.2 Patient study . . . 79
5.4 Discussion . . . 79

6 Conclusions and recommendations 85
6.1 Joint estimation of chemical shift and quantitative susceptibility mapping . . . 85
6.2 Bone quantitative susceptibility mapping . . . 85
6.3 High resolution QSM for STN imaging . . . 86

Bibliography 88

LIST OF TABLES

4.1 Measured susceptibility values of cortical bone in the distal femur, proximal tibia, and distal radius of 7 healthy volunteers . . 66

5.1 Imaging parameters. 74
5.2 Characterization of the STN quadrants contrast-to-noise ratios (CNR) relative to adjacent tissue. (*) indicates statistically significant difference ($p<0.05$) between resolutions. 78
5.3 STN inter-quadrant contrast ratios 79

LIST OF FIGURES

2.1 (A) Fast spoiled gradient recalled echo (FSPGR) pulse sequence. (B) k-space trajectory of the standard gradient echo pulse sequence. Solid line indicates the current readout trajectory, dashed line indicates k-space line acquired in other readout. Dotted lines are used to indicate the trajectory of the offset gradients. 11

2.2 (A) Pulse sequence for radial acquisition; there is no phase encoding, and the amplitude of G_x and G_y vary to produce different spokes. (B) k-space trajectory in radial sampling. 13

2.3 (A) Magnitude, (B) raw field map and (C) corrected field map. Subcutaneous and interstitial fat regions (arrows) manifest themselves in the raw field map with apparent frequency offsets due to chemical shift. 22

3.1 Flowchart of the proposed algorithm. Symbols are defined in the text. Note that local field is updated at step 4 compared to step 2. 33

3.2 Results of the numerical experiments: comparison of QSM maps reconstructed using conventional T_2^*-IDEAL and proposed algorithm (first row: one-peak fat spectrum, second row: multi-peak fat spectrum). (A), (E): T2*-weighted images of the simulated phantoms. (B), (F): QSM images reconstructed from the susceptibility field fs estimated with assumption of the chemical shift value f_1 = -3.46 ppm. (C), (G): QSM images reconstructed from the susceptibility field f_s estimated with proposed iterative algorithm. (H), (I): Difference between QSM maps reconstructed from the susceptibility fields fs estimated with proposed algorithm and the true susceptibility maps. Note that significant suppression of the streaking artifacts was achieved using the proposed algorithm in (C) and (G). 36

3.3 Results of the numerical experiments: comparison of local field maps reconstructed using conventional T_2^*-IDEAL and proposed algorithm. (A): local field map reconstructed with the true spectrum. (B): local field map reconstructed with assumption of the chemical shift value f_1 = -3.46 ppm. (C): local field map reconstructed using the proposed algorithm. (D), (E): Difference between (A) and (B), and (A) and (C), respectively. It can be seen that frequency offset in regions with high fat content is reduced after correction of the chemical shift in (C) and (E). 41

3.4 Results of the numerical experiments: comparison of fat fraction maps reconstructed with different assumed spectra. A: true fat fraction map. B: fat fraction maps reconstructed with assumption of the chemical shift value f_1 = -3.46 ppm. C: fat fraction maps reconstructed using the proposed chemical shift update. D, E: Difference between A and B, and A and C, respectively. Both B and C showed similar fat fraction maps with respect to the truth. 42
3.5 Lard experiment. (A): Dependence of the lard susceptibility field variation on the susceptibility of the Gd solution. (B): Results of the piece-wise estimation of the lard susceptibility relative to the background solution for different concentrations of Gd. (C): Results of the lard susceptibility using the proposed algorithm for different concentrations of Gd. The susceptibility values of lard estimated using three different techniques were in good agreement. 43
3.6 Reconstructed local field maps and QSM of the lard experiment. (A), (D): Magnitude image. (B), (E): QSM image reconstructed from the susceptibility field f_s estimated with assumption of the chemical shift value f_1 = -3.46 ppm. (C), (F): QSM image reconstructed from the susceptibility field fs estimated with proposed iterative algorithm. (G), (I): local field map corresponding to (B), (E), and (H), (J): the local field map corresponding to (C), (F). Images (A)-(C), (G), and (H) are coronal views. Images (D)-(F), (I), and (J) are sagittal views. Note the frequency offset in the lard region in the local field (G), (I) and the resulting artifact in the susceptibility map (B), (E) for the fixed chemical shift reconstruction. These are similar to those observed in numerical simulations in Fig. 3.3, and the artifacts are suppressed using the proposed algorithm as shown in (C) and (F). 45
3.7 Results of the bovine tissue experiment: comparison of QSM maps reconstructed using conventional T_2^*-IDEAL and the proposed algorithm from 15 and 6 echo data. A: T_2^*-weighted image. (B), (D): QSM image reconstructed from the susceptibility field f_s estimated with assumption of the chemical shift value f_1 = -3.46 ppm using 15 and 6 echoes, respectively. (C), (E): QSM image reconstructed using the proposed iterative algorithm using 15 and 6 echoes, respectively, (F)-(I) are the local fields corresponding to (B)-(E), respectively. The proposed chemical shift update suppresses streaking artifacts for both datasets, although the use of more echoes resulted in a higher quality susceptibility map. . . . 46

3.8 Comparison of mammogram (A) with minimal intensity projections of breast QSMs reconstructed without (B) and with (C) the proposed algorithm. Arrows point to the detected calcifications, which are better seen in the map reconstructed with the proposed method as compared to that reconstructed with the fixed chemical shift reconstruction. 47
3.9 Results of a volunteer breast contrast exam (post Gd injection images are shown): comparison of QSM maps reconstructed using a fixed chemical shift (B) and the proposed algorithm (C). A T_2^*-weighted image (A) is provided as a reference. Arrows point to the location of a biopsy clip. Note the more homogeneous distribution of the fat susceptibility values and the brighter appearance of the metal object relative to fat after application of the chemical shift correction. 48
3.10 Model residual as a function of the chemical shift; the + symbols indicate the location of the successive iterations of the proposed algorithm for the data in Fig. 3.9. This demonstrates that the proposed method finds the global minimum of the combined fat, water and chemical shift minimization problem. 48

4.1 Top: Dual echo gradient echo acquisition for acquiring one ultra-short echo and one conventional echo image. Both echoes are shifted between successive TRs to acquire four unique echo time values. Echoes acquired in the same TR are shown using the same line type. The images below compare the magnitudes and phases of two of the acquired echoes. The phase of the first echo is set to zero during coil combination to eliminate phase offsets of different channels. 58
4.2 Regression of QSM vs. CT for the ROI values in the porcine hoof phantom. Good correlation was observed between estimated susceptibility and Hounsfield units. 61
4.3 Comparison of CT images (A,C) with correspondent planes of reconstructed QSM (B,D) and ultra-short (40 μs) echo magnitude (E,F). Note the homogeneous diamagnetic appearance of cortical bones and overall fair correspondence between regions of high HU and low susceptibility values. 62
4.4 Results of field map reconstruction (A), susceptibility (B), and magnitude of the ultra-short (40 μs) echo (C) using femur data from a healthy volunteer. Note the homogeneous diamagnetic appearance of the cortical bone and the visible trabeculation in both the field map and QSM (*), and strong diamagnetism of the quadriceps tendon (**). Please refer to Fig. 4.5 for further details on the selected area (dashed line). 63

4.5 Comparison of fat and water fraction maps, field maps, QSM and estimated tissue signal decay rates for different signal models, including single- and multi-peak fat spectrum and common and water-only R_2^* modeling 64
4.6 Local field (left) and thin slab maximum intensity projection of knee joint QSM (right), reconstructed using the proposed technique. A minimum intensity projection of the reconstructed QSM of the knee joint is shown in one healthy subject. Note the delineation of cortical areas of the femur and tibia (yellow arrows), the depiction of trabeculation, the epiphyseal line (red arrow), and the area of transition from diaphyseal to metaphyseal bone (blue arrow) in the femur, and reduced contrast between the bone and surrounding joint tissue. 65

5.1 Axial and coronal views of the STN in T2w (A,C) and QSM (B,D) images from a healthy 25-year-old man showing the subthalamic nucleus (STN), substantia nigra (SN) and red nucleus (RN). Border points indicated by (x) were used to create bilateral masks of the nuclei (A) and to define the four STN quadrants: anterolateral (AL), anteromedial (AM), posterolateral (PL) and posteromedial (PM) (A). STN susceptibility gradient (shown with arrows) is clearly visible in the QSM images. 76
5.2 Effects of slice thickness on STN-vs-tissue contrast in T2w and QSM images in a healthy 33 year-old man. Left column T2w (A) and QSM (C) images with slice thickness of 0.5 mm; (B) and (D) T2w and QSM images, respectively, with slice thickness of 2 mm. Visibility of STN in T2w is relatively insensitive to slice thickness, as indicated by CNR measurements and the T2w image scores given by the radiologist. However, low resolution results in susceptibility underestimation in QSM, led to significantly reduced contrast in the posterolateral quadrant (dashed arrows). Unlike T2w, QSM demonstrates a clearly visible gradient towards the caudal STN pole (-0.024 ppm/mm) in both hemispheres. 80
5.3 Comparison of intensity profiles extracted from sub-millimeter resolution QSM (A, B) and T2w (C, D) images of STN along the rostro-caudal axis. (A, C) left STN; (B, D) right STN. QSM consistently indicates a linear decrease in iron concentration (red dashed line), with an average susceptibility gradient of -0.022 ppm/mm. 81

5.4 QSM of STN (arrows) in axial (A) and coronal (B) planes in a 58 year-old male with PD. QSM provided good spatial definition of STN geometry; ability to differentiate between STN, SN and surrounding white matter; and visualized a decrease in iron towards the dorsolateral portion of the nucleus. 82

CHAPTER 1

INTRODUCTION

Magnetic resonance imaging (MRI) is a noninvasive imaging modality that has found its uses in a multitude of clinical applications. The fundamental physical principle laid in foundation of MRI is nuclear magnetic resonance (NMR) acquired signal originate from the interaction of magnetic fields and radio frequency pulses with magnetic moments (spins) of protons. Based on proton density, relaxation times, off-resonance effects and manipulation of magnetic moments, MRI is able to provide a rich variety of tissue contrasts.

Majority of currently present MRI techniques are qualitative in nature. Quantitative approaches capable of giving insight into tissue composition and function can fundamentally transform scientific and clinical investigations.

1.1 Summary of contributions

This dissertation is focused on technical development and potential applications of quantitative susceptibility mapping (QSM). In short, the main goal of QSM is to solve an inverse field-to-source problem to generate a volumetric map of magnetic susceptibility sources distribution within a region of interest. Its physical and mathematical principles will be discussed in greater details in Chapter 2.

Chapter 2 also provides the background for water/fat separation an MRI-based technique that is used in conjuction with QSM in the current thesis and ultra-short echo time (UTE) imaging. Chapter 3 presents a work to address the unsolved problem of quantitative susceptibility mapping (QSM) of tissue

with fat where both fat and susceptibility change the MR signal phase. The chemical shift of fat was treated as an additional unknown and was estimated jointly with susceptibility to provide the best data fitting using an automated iterative algorithm. A simplified, piece-wise susceptibility model was used to calculate an updated value of the chemical shift based on the local magnetic field in each iteration. Numerical simulation, phantom experiments and in vivo imaging were performed. Using the proposed method, artifacts on the QSM images were markedly suppressed in all tested datasets compared with results generated using fixed chemical shifts. Accuracy of the estimated susceptibility was also improved in numerical simulation and phantom experiments.

Chapter 4 proposes a signal model tissue-specific R2* decay factor to model water/fat MR signals. Three-dimensional radial UTE acquisition was employed to acquire data which was then fit with the proposed bone-specific signal model to map the chemical species and susceptibility field. Experiments were performed ex vivo and on healthy human subjects. For water/fat separation, a bone-specific model assigning R2* decay mostly to water was compared with the standard models that assigned the same decay for both fat and water. In the ex vivo experiment, bone QSM was correlated with CT. Compared with standard models, the bone-specific R2* significantly reduced errors in the fat fraction within the cortical bone in all tested data sets, leading to reduced artifacts in QSM. Good correlation was found between bone CT and QSM values in the ex vivo specimen. Bone QSM was successfully generated in all subjects. The QSM of bone was shown to be feasible using UTE with a conventional echo time GRE acquisition

Chapter 5 develops a QSM acquisition protocol for deep brain stimulation

(DBS) surgery planning. Faithful depiction of the subthalamic nucleus (STN) is critical for surgery in patients with Parkinsons disease (PD). Quantitative susceptibility mapping has shown to be superior to traditional T2 weighted spin echo imaging (T2w). The aim of the study was to describe sub-millimeter QSM for DBS preoperative imaging of STN. 7 healthy volunteers were included in this study. T2w and QSM were obtained for all healthy volunteers, and images of different resolutions were reconstructed. Image quality and visibility of STN anatomical features were analyzed by a radiologist using a 5 point scale, and contrast properties of the STN and surrounding tissue were calculated. Additionally, data from 10 retrospectively and randomly selected patients with PD who underwent 3T MRI for DBS was used for STN size and susceptibility gradient measurements. Results were compared with the healthy volunteers. Higher contrast-to-noise (CNR) values were observed in both high and low resolution QSM images. Inter-resolution comparison demonstrated improvement in CNR for QSM, but not for T2w images. QSM provided higher inter-quadrant contrast ratios (CR) within the STN, and depicted a gradient in the distribution of susceptibility sources not visible in T2w images. It was shown that foor 3T MRI, sub-millimeter QSM provides accurate delineation of the functional and anatomical STN features for DBS targeting.

CHAPTER 2

BACKGROUND

2.1 MRI physics

2.1.1 Spin behavior in a magnetic field

MRI is based on NMR nuclear magnetic resonance. Particularly, the main interest in the field of MRI physics in focused on hydrogen nucleus due to its abundance in human body as a part of water and other molecules.

On the quantum level, a hydrogen nucleus (single unpaired proton) has a fundamental property its intrinsic angular momentum $\vec{s}$, commonly referred to as *spin*. It is a vector property that, in a way, describes orientation of the particle relative to a chosen direction of a z-axis. Each spin orientation can be viewed as a *quantum state* with a distinct *energy level* associated with it. Protons have a one-half spin, and, therefore, only two such states exist - *"spin up"* ($s_z = \frac{1}{2}$, with z-axis oriented along the field) and *"spin down"* ($s_z = -\frac{1}{2}$).

Under normal conditions, no energy difference exists between these states (i.e., energy levels are *degenerate*), and number of spins in each state is approximately equal and zero net magnetization is created. However, this symmetry is broken once the sample is introduced into an external magnetic field $\vec{B}_0$ the spin-up state becomes preferential due to the lower potential energy. Thus, a small bias in spin energy distribution will be created, producing a net magnetic moment.

2.1.2 Bloch equation

The evolution of the net magnetization $\vec{M}$ in a magnetic field $\vec{B}$ is described by the phenomenological differential equation, proposed by Felix Bloch (1946):

$$\frac{d\vec{M}}{dt} = [\gamma\vec{M} \times \vec{B}] - \frac{(M_z - M^0)\hat{z}}{T_1} - \frac{(M_x\hat{x} + M_y\hat{y})}{T_2} \tag{2.1}$$

Here, M^0 is the equilibrium magnetization created when the sample is placed in the field $\vec{B}$, and M_x, M_y and M_z are the projections of $\vec{M}$ onto the coordinate axes at a given moment of time. M_z is commonly referred to as the *longitudinal* magnetization component, while M_x and M_y are said to form the *transverse* component in the plain perpendicular to $\vec{B}$. Proportionality constant γ included into the first right-hand side term is known as the *gyromagnetic ratio*, a nucleus-specific constant (in case of ^1H, $\gamma = 42.58$ MHz/T). Time constants T_1 and T_2 describe the rates of longitudinal (due to spin-lattice interactions) and transverse (due spin-spin energy exchange) magnetization relaxations. These constants, being different for different tissues, play crucial role in conventional clinical MRI as a foundation to so-called *T1w* and *T2w contrasts*.

2.1.2.1 Precession

The first term in the Eq. 2.1 describes the process known as Larmor precession of magnetization about $\vec{B}$.

Indeed, if the magnetic field $\vec{B}$ is oriented entirely along longitudinal direction and relaxation processes are omitted for simplicity, then Eq. 2.1 can be

re-written in the following form:

$$\frac{dM_x}{dt} = \gamma M_y B_z$$
$$\frac{dM_y}{dt} = -\gamma M_x B_z \tag{2.2}$$

For a set of initial conditions on variables, M_x^0 and M_y^0, solution to this dynamic system can be easily obtained:

$$M_x(t) = M_x^0 cos(\gamma B_z t) + M_y^0 sin(\gamma B_z t)$$
$$M_y(t) = -M_x^0 sin(\gamma B_z t) + M_x^0 cos(\gamma B_z t) \tag{2.3}$$

This solution 2.3 indicates that $\vec{M}$ precesses about the external magnetic field with angular frequency of $\omega_0 = \gamma B_z$.

2.1.2.2 Relaxation

The second and the third terms in the Eq. 2.1 describe two fundamental magnetization relaxation properties.

Projecting Eq. 2.1 onto z-axis, once can write:

$$\frac{dM_z}{dt} = \frac{(M_z - M^0)\hat{z}}{T1} \tag{2.4}$$

This is a trivial differential equation, for which the solution is

$$M_z(t) = M^0 + (M_z^0 - M^0)e^{-\frac{t}{T_1}} \tag{2.5}$$

where M_z^0 is the initial condition. This solution suggests that longitudinal magnetization of a system tipped away from equilibrium will eventually return to its fully aligned equilibrium state.

Similarly, using a frame of reference rotating about z-axis with frequency of ω_0, it is possible to extract the following equation for transverse component $M_\perp = M_x\hat{x} + M_y\hat{y}$ from Eq. 2.1:

$$\frac{d\vec{M}_\perp}{dt} = -\frac{\vec{M}_\perp}{T_2} \tag{2.6}$$

It follows that transverse magnetization decays according to

$$\vec{M}_\perp = \vec{M}^0_\perp e^{-\frac{t}{T_2}} \tag{2.7}$$

In other words, any magnetization component $\vec{M}^0_\perp$ that exists in transverse plane at the moment of time $t = 0$, will eventually disappear as $t \to \infty$.

In addition to T_2 relaxation, in many practical applications it is necessary to account for the signal decay due to phase dispersion created by magnetic field imperfection within a given volume. Resulting relaxation time is known as T_2^*, or apparent relaxation time. Relation between T_2 and T_2^* can be written in the following form:

$$\frac{1}{T_2^*} = \frac{1}{T_2} + \frac{1}{T_2'} \tag{2.8}$$

As can be seen from the Eq. 2.8, T_2^* is always shorter than T_2.

2.1.2.3 Excitation

If magnetic field $\vec{B}$ in Eq. 2.1 has a dynamic term $\vec{B}_1$ (i.e., $\vec{B} = \vec{B}_0 + \vec{B}_1$, where $\vec{B}_0$ is the static magnetic field), then behavior of magnetization can be manipulated to create transverse magnetization component.

In particular, if applied $\vec{B}_1$ has a projection onto x-y plane $\vec{B}_{1\perp}$, then cross-product $[\gamma\vec{M} \times \vec{B}]$ yields a non-zero term for M_z. As a result, $\vec{M}$ will start tipping

away from the longitudinal axis in the vertical plane orthogonal to $\vec{B}_{1\perp}$. Due to the aforementioned effects of static field $\vec{B}_0$, however, further precession of $\vec{M}$ will break this state of orthogonality which will result in flipping magnetization back towards $\hat{z}$ with no net magnetization.

If the field $\vec{B}_1$ will rotate about $\hat{z}$ with the angular frequency of $\omega_0 = \gamma B_0$ (*on resonance*), orthogonality of $\vec{M}$ and $\vec{B}_{1\perp}$ can be preserved, causing magnetization to rotate towards the transverse plane. The angle of such rotation (*flip angle*) will be dependent on the value of $\vec{B}_{1\perp}$ and duration of $\vec{B}_1$ application.

In MRI, $\vec{B}_1$ is introduced by application of electromagnetic pulses. Since precession ω_0 is required, the carrier frequency of such pulses lies in radiofrequency diapason, and the pulses themselves are usually referred to as *RF pulses*.

2.2 Signal detection

Transverse magnetization $M_\perp$ evolving according to Bloch equation does produce a harmonic electromagnetic field that can be detected using a reception coil. If $\vec{b}$ is the generated magnetic field, then a nearby conductive coil A will experience the *magnetic flux*:

$$\Phi = \int_A (\vec{b} \cdot d\vec{A}) \tag{2.9}$$

In agreement with Faradays law, this flux will induce an electromotive force u in the coil:

$$u = -\frac{d\Phi}{dt} = (for\ harmonic\ \vec{b}) = i\omega_0\Phi \tag{2.10}$$

The flux through the coil depends on the magnetization $M_\perp$ and the coil sen-

sitivity function $c(\vec{r})$. Thus,

$$u = i\omega_0 c(\vec{r}) M_\perp \tag{2.11}$$

Realistically, we always deal with large distributions of spins, and both ω and $M_\perp$ should be treated as functions of coordinate $\vec{r}$. Additionally, T_2 effects (omitted in our analysis for simplicity) should be accounted for. Accordingly, *signal equation* Eq. 2.11 can be written in the general form as

$$U(t) = i \int_{\vec{r}} \omega(\vec{r}) M_\perp(\vec{r}) c(\vec{r}) e^{-i\omega t} e^{-\frac{t}{T_2}} d^3\vec{r} \tag{2.12}$$

This electric signal is amplified, digitized, demodulated and filtered. Typically, an array of receiver coils is used in this case, Eq. 2.12 should be considered written for a single coil element.

2.3 Spatial encoding

In practice, it is desirable to be able to resolve spins (*spin isochromats*) at different locations, thus obtaining information about their distribution. In MR, this goal is achieved through application of *encoding schemes*.

If in addition to $\vec{B}_0$ a linear gradient field $\vec{G}(t)$ exists, i.e. the total magnetic field along $\hat{z}$ can be written as

$$B(\vec{r}) = B_0 + (\vec{G} \cdot \vec{r}) \tag{2.13}$$

At different locations, spins will experience slightly different values of magnetic field. As a result, a spatial distribution of precession rates will be achieved:

$$\omega(\vec{r}) = \gamma B_0 + \gamma(\vec{G} \cdot \vec{r}) = \omega_0 + \gamma(\vec{G} \cdot \vec{r}) \tag{2.14}$$

Plugging Eq. 2.14 to Eq. 2.12, one can obtain:

$$\begin{aligned} U(t) &= i \int_{\vec{r}} M_{\perp}(\vec{r}) \left(\omega_0 + \gamma(\vec{G} \cdot \vec{r})\right) c(\vec{r}) e^{-i\omega_0 t} e^{-i\gamma(\vec{G}\cdot\vec{r})t} e^{-\frac{t}{T_2}} d^3\vec{r} \approx \\ &\approx i\omega_0 e^{-i\omega_0 t} e^{-\frac{t}{T_2}} \int_{\vec{r}} M_{\perp}(\vec{r}) c(\vec{r}) e^{-i\gamma(\vec{G}\cdot\vec{r})t} d^3\vec{r} \end{aligned} \tag{2.15}$$

Here the fact that $\omega_0 \gg \gamma(\vec{G} \cdot \vec{r})$ is used. With substitution $\vec{k} = \frac{\gamma}{2\pi}\vec{G}t$, Eq. 2.15 becomes

$$U(\vec{k}) = \widetilde{U} \int_{\vec{r}} [M_{\perp}(\vec{r}) c(\vec{r})] e^{-i2\pi(\vec{k}\cdot\vec{r})} d^3\vec{r} \tag{2.16}$$

Equation 2.16 suggests that signal acquired during an MRI scan represents the *Fourier transform* of the objects transverse magnetization $M_{\perp}(\vec{r})$ modulated by the coil sensitivity function $c(\vec{r})$. Accordingly, unknown $m_{\perp}(\vec{r}) = M_{\perp}(\vec{r})c(\vec{r})$ can be reconstructed through the inverse Fourier transform of the acquired signal:

$$m_{\perp}(\vec{r}) = \mathcal{F}^{-1}\left[U\left(t(\vec{k})\right)\right] \tag{2.17}$$

The vector $\vec{r}$ is interpreted as the *spatial frequency* vector. In MRI, signal sampled at the moment of time t corresponds to coefficient of the point $\vec{r}$ in the multidimensional *k-space* which is navigated by adjusting gradient field $\vec{G}(t)$. Depending on application, different sampling strategies can be designed by using different $\vec{G}(t)$.

2.4 Sampling trajectories in k-space

Multiple acquisition schemes have found their application in MRI. Described here are two common ones Cartesian and radial sampling trajectories, both of which are used in the present thesis.

2.4.1 Cartesian sampling

The most common way in MRI to traverse k-space is using Cartesian trajectories. In this approach, individual lines of k-space are sampled one by one. A typical *pulse sequence* diagram and corresponding k-space trajectory is shown in Fig. 2.1.

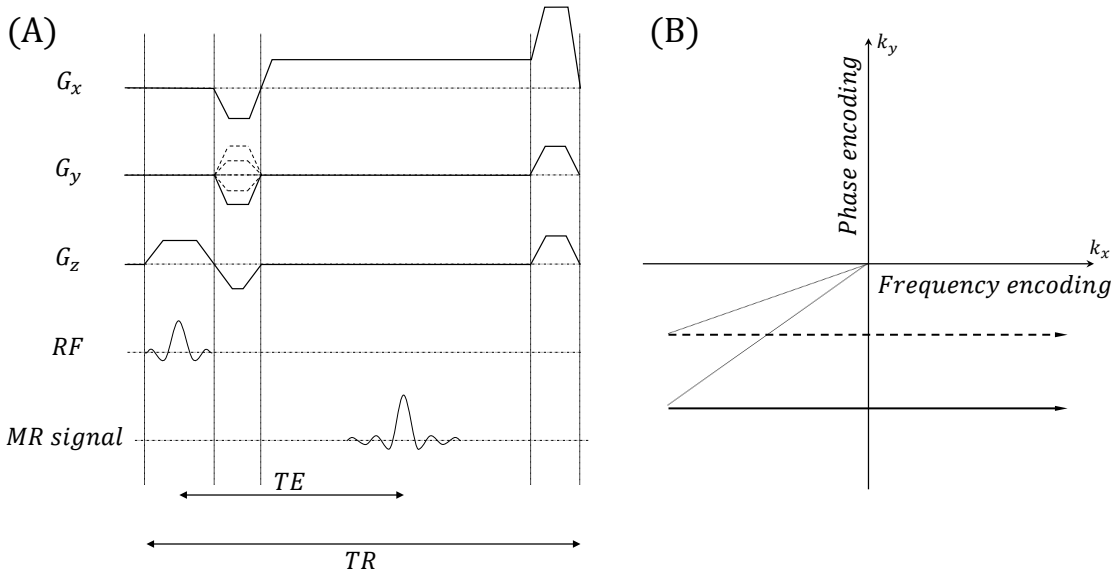

Figure 2.1: (A) Fast spoiled gradient recalled echo (FSPGR) pulse sequence. (B) k-space trajectory of the standard gradient echo pulse sequence. Solid line indicates the current readout trajectory, dashed line indicates k-space line acquired in other readout. Dotted lines are used to indicate the trajectory of the offset gradients.

The pulse sequence is initiated with application of an excitation RF pulse and simultaneous slice selection gradient (G_z). This gradient creates resonant condition only for a spins within a certain section of the object of interest. Slice selection gradient is followed by a *rephasing gradient lobe* that creates an offset to the appropriate position along the k-space z axis and helps to correct for the

phase dispersion of transverse magnetization. Particularly, without this lobe, intravoxel phase dispersion would occur resulting in unwanted signal loss. Simultaneously with rephasing gradient, two *prewinder* gradient pulses (often called as *frequency* and *phase encoding gradients*) are played along x and y axes to offset to the appropriate coordinate of k-space. After this, the readout gradient is activated (G_x), and when it ramps up to the maximum value, the receiver is turned on. Area accumulated under the readout gradient with the progression of time forms a trajectory that traverses k-space along a k_y line. After acquisition is complete, *rewinding* gradients are applied along y and z axes, returning the trajectory to the origin point. Concurrently with rewinders, a *spoiler* gradient is applied on the axis to obliterate any residual transverse magnetization. Application of the spoiler guarantees that in the next repetition comes primarily from the longitudinal component.

Cartesian pulse sequence showcases important time parameters used in description of MRI acquisitions. The total duration of a single k-space line acquisition (including RF excitation and accompanying gradients) is called *repetition time*, or simply *TR*. Period of time between the middle of RF pulse and readout passing closest to the center of k-space is referred to as *echo time*, or *TE*.

2.4.2 Radial sampling

In Cartesian acquisition scheme, all spatial frequencies are equally covered. However, for a typical real-world image most of the energy is concentrated in the center of the k-space. Therefore, it appears to be more efficient to spend extra time finely sampling low frequency area at the expense of sampling less

informative high frequencies. This idea is realized in radial sampling.

2.4.2.1 Basic structure

In radial sampling, the k-space is mapped by a set of radial spokes acquired sequentially. Each spoke is a k-space line as in Cartesian sampling but they all cross the center of k-space. Two consecutive *spokes* are rotated by a defined angle ϕ relative to each other. Fig. 2.2 shows the pulse sequence diagram and k-space trajectory used in 2D radial sampling.

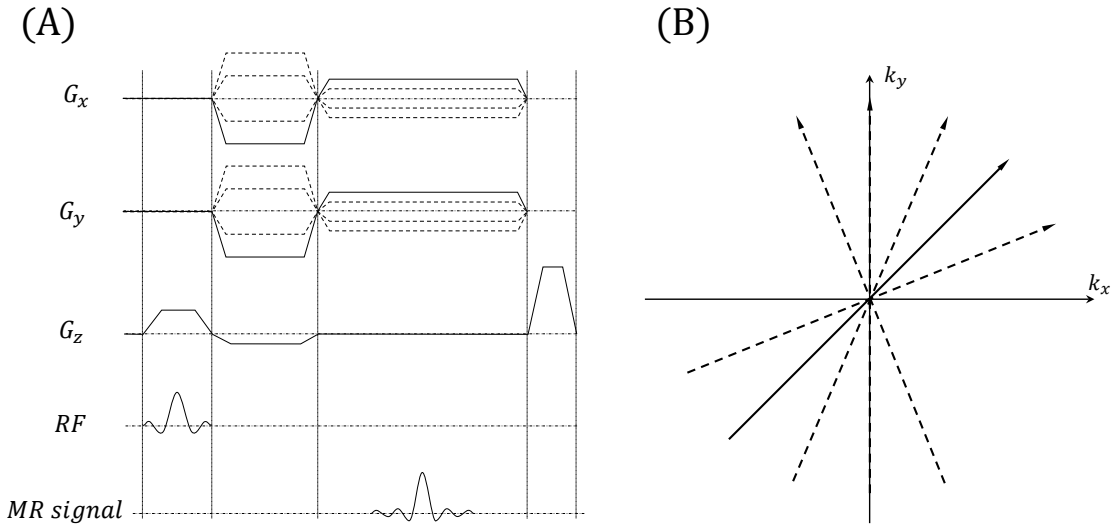

Figure 2.2: (A) Pulse sequence for radial acquisition; there is no phase encoding, and the amplitude of G_x and G_y vary to produce different spokes. (B) k-space trajectory in radial sampling.

To achieve the radial pattern, frequency encoding gradients are applied in different physical directions with varying amplitudes. The rest of the sequence structure closely resembles Cartesian scheme.

2.4.2.2 Ultra-short TE imaging

Because no phase encoding gradient is used in radial imaging, the minimum achievable TE can be very short. This advantage can be further combined with sampling of partial spokes only by moving solely from the center of the k-space to the periphery. This leads to a shorter pathway in k-space and allows for imaging at higher sampling rates. If the nonselective volume excitation, radial sampling can produce TE around several of microseconds. This modification allows to acquire signals from biological tissue with extremely short T_2^* (sub-millisecond) relaxation times cortical bone, tendons, menisci, etc invisible to other imaging sequences.

2.5 Image reconstruction

For the data acquired using Cartesian acquisition scheme with sampling density satisfying *Nyquist condition*, the inverse Fourier transform is sufficient to reconstruct the image (Eq. 2.17). In MRI, k-space sampling is not continuous, and, therefore, discrete version of Fourier transform (DFT) is used:

$$\hat{m}_{\perp}(x,y,z) = \frac{1}{\sqrt{N_x N_y N_z}} \sum_{n=0}^{N_z-1} \sum_{m=0}^{N_y-1} \sum_{l=0}^{N_x-1} U(l,m,n)\, e^{\frac{i2\pi lx}{N_x}} e^{\frac{i2\pi my}{N_y}} e^{\frac{i2\pi nz}{N_z}} \tag{2.18}$$

Here $\hat{m}_{\perp}$ is the sought magnetization distribution modulated by coil sensitivity function, x, y and z are real space coordinates; l, m and n are indices of a point in k-space; N_x, N_y and N_z are total number of points in three directions.

If the sampling grid is equidistant, then equation can be efficiently evaluated using fast Fourier transform (FFT) algorithm. This brings down complexity of

the problem from $O\left(N_x^2 N_y^2 N_z^2\right)$ to $O\left(N_x N_y N_z \cdot log(N_x N_y N_z)\right)$, allowing for real-time image reconstruction.

While switching from Cartesian to radial acquisition might seem like a minor technical step, it brings significant changes to the reconstruction process. Particularly, the k-space points sampled along spokes do not lie on a regular grid are not equidistant, making FFT inapplicable in the straightforward fashion. Direct Fourier inversion is very computationally expensive and thus infeasible in clinical imaging. Further on, since during radial acquisition the central area of k-space is traversed more often than any other region, collected samples are not equally distributed. This leads to overestimation of low spatial frequencies components and image blurring. To avoid these issues, advanced reconstruction techniques like *gridding* are used.

2.5.1 Gridding reconstruction

In gridding, measured spokes are interpolated onto a Cartesian coordinate grid, after which FFT can be utilized.

First, the original data is weighted by a density compensation function (DCF) that depends on employed k-space sampling scheme. In case of radial sampling, the density of samples is inversely proportional to the distance from the center, and analytic representation of DCF for radial sampling can be written as

$$DCF(\vec{k}) = \begin{cases} \dfrac{|\vec{k}|}{n}, & |\vec{k}| \neq 0 \\ \dfrac{1}{2n}, & |\vec{k}| = 0 \end{cases} \tag{2.19}$$

where n is the total number of spokes acquired.

At the next stage, interpolation is performed. Since during the interpolation information from measured samples is "diffused" to non-visited points, the process can be viewed as a convolution between the original data and a predefined kernel. For a given point of interest in k-space $\vec{k}$, interpolated value will be:

$$U(\vec{k}) = \sum_n Kernel(|\vec{k} - \vec{k}_n|) \cdot U_n \tag{2.20}$$

where summation is performed over n sampled points.

The optimal interpolation kernel is a properly scaled sinc function. However, computation of convolution with the sinc is costly and impractical due to its unlimited support. Because of that, approximations of sinc, such as *Kaiser-Bessel kernel*, are typically used in MR reconstruction. The size of the kernel is usually chosen to correspond to doubled field of view (FOV) in image space to avoid aliasing artifacts.

An image, reconstructed this way, suffers from an unwanted spatial modulation due to convolution with the finite interpolation kernel. To minimize this effect, a *roll-off correction* is performed as the last step the image is divided by the kernels Fourier transform.

2.5.2 Parallel imaging

As was briefly mentioned in 2.2, multiple channel coil arrays are often employed. One of the major reasons for this is spatially limited sensitivity $c(\vec{r})$ of an individual coil that would prevent imaging of large volumes. In this case, Eq. 2.16 can be re-written:

$$U_j(\vec{k}) = \int_{\vec{r}} [M_\perp(\vec{r}) c_j(\vec{r})] e^{-i2\pi(\vec{k}\cdot\vec{r})} d^3\vec{r} \tag{2.21}$$

where U_j is the signal received by the j^th coil element, $c_j(\vec{r})$ its spatial sensitivity.

Acquisition with multiple coils results in *redundancy* of the acquired data signal generated at the position $\vec{r}$ is sampled by several receivers. This redundancy can be exploited to reduce the acquisition time.

If Cartesian acquisition uniformly undersamples data with an acceleration factor R, then each voxel of reconstructed image will contain signals from R aliased voxels in the fully sampled image, each weighted by the coil spatial sensitivity:

$$\hat{\rho}_l = \sum_{i=1}^{R} c_{l,i}\rho_i \tag{2.22}$$

where $\hat{\rho}_l$ is the voxel in the undersampled image from the l^{th} coil, ρ_i is a voxel in a fully sampled image, and $c_{l,i}$ is sensitivity of the l^{th} coil at all locations of ρ_i. If N_c coils are used, Eq. 2.22 can be formulated in the matrix form:

$$\begin{pmatrix} \hat{\rho}_1 \\ \vdots \\ \hat{\rho}_{N_c} \end{pmatrix} = \begin{pmatrix} c_{1,1} & \cdots & c_{1,R} \\ \vdots & \ddots & \vdots \\ c_{N_c,1} & \cdots & c_{N_c,R} \end{pmatrix} \begin{pmatrix} \rho_1 \\ \vdots \\ \rho_R \end{pmatrix} \tag{2.23}$$

or

$$\hat{\rho} = \mathbf{C}\rho \tag{2.24}$$

If this linear system is critically determined ($N_c = R$) or overdetermined ($N_c > R$), and the coil sensitivities are distinct, the pseudoinverse of $\mathbf{C}$ exists, and accurate estimation of the each image voxel can be obtained as

$$\rho = \left(\mathbf{C^H C}\right)^{-1} \mathbf{C^H} \hat{\rho} \tag{2.25}$$

This approach is referred to as sensitivity encoding, or *SENSE*.

2.6 Quantitative susceptibility mapping

When matter interacts with the magnetic field, an internal magnetization is created, primarily due to alignment of electron spins and orbits. The strength of such magnetization relative to the external field is characterized by *magnetic susceptibility*. Biological tissues can be broadly classified based on their susceptibility into *paramagnetic* and *diamagnetic*.

Diamagnetic tissues and materials (bone, cartilage, myelin, tissue calcifications) consist of atoms that do not have permanent magnetic moments. In this case, magnetic moments are created by induce magnetization of the electron orbits, and they oppose the external magnetic field. Paramagnetic tissues (fat, blood) contain atoms with constant magnetic moments that orient themselves along the applied field. Biological paramagnetism is typically much stronger than diamagnetism.

The main goal of quantitative susceptibility mapping (QSM) is to estimate the distribution of susceptibility sources within the given region of interest (ROI).

2.6.1 Susceptibility-induced magnetic fields

For an object with known magnetic susceptibility distribution $\chi(\vec{r})$, the longitudinal field perturbation b_z induced by external field B_0 can be expressed as a convolution:

$$\frac{b_z(\vec{r})}{B_0} = \frac{\mu}{4\pi} \int_{\mathbb{R}^3, \vec{r}' \neq \vec{r}} \frac{3cos^2\theta - 1}{|\vec{r}' - \vec{r}|} \chi(\vec{r}') d^3\vec{r}' = (d * \chi)(\vec{r}) \tag{2.26}$$

Here $\vec{r}$ is an observation point, $\vec{r}'$ - source location, θ is the angle between the difference vector $\vec{r}' - \vec{r}$ and $\vec{B}_0$.

This variation of the field will be observed by surrounding protons as will be indicated by changes in phase of their precession. Signal Eq. 2.15 can be modified for this case:

$$S\left(t(\vec{k})\right) \propto \int_{\vec{r}} [M_{\perp}(\vec{r})c(\vec{r})] e^{-i\gamma B_0 (d*\chi)t} e^{-i2\pi(\vec{k}\cdot\vec{r})} e^{-\frac{t}{T_2}} d^3\vec{r} \tag{2.27}$$

With realistic assumptions that readout time is much shorter that T_2, and that readout gradient is much stronger that ∇b_z, relation 2.27 can be modified for a signal acquired from a vicinity δ of a point $\vec{r}$ at the echo time $t = TE$:

$$\begin{aligned} S(\vec{r}, TE) &\propto e^{-\frac{TE}{T_2}} \int_{\delta(\vec{r})} M_{\perp}(\vec{r}) c(\vec{r}) e^{-i\omega_0 (d*\chi)(\vec{r}')TE} d^3\vec{r}' \approx \\ &\approx \overline{M}_{\perp} V_{\delta} e^{-\frac{TE}{T_2^*}} e^{-i\gamma \bar{b}_z TE} \end{aligned} \tag{2.28}$$

Here $\overline{M}_{\perp}$ is an average volumetric density of proton around $\vec{r}$, V_{δ} is the volume of the considered neighborhood δ of $\vec{r}$, T_2^* is the apparent relaxation time. Obtained equation 2.28 signifies that phase of the MRI signal allows measurement of the magnetic field generated by distribution of magnetic sources. By acquiring images at multiple echo times, phase changes over time can be used to determine the frequency at each voxel in the image, yielding the magnetic field shift at each location.

2.6.2 Susceptibility mapping

Susceptibility field can be measured using gradient echo (GRE) sequence. In order to recover the susceptibility distribution, a deconvolution problem has to

be solved. One possible approach is to utilize a property of Fourier transform that states that convolution in image space corresponds to multiplication in k-space, and vice versa. With this, the following can be derived from the equation:

$$\chi(\vec{r}) = \mathcal{F}^{-1}\left(\frac{\mathcal{F}(b_z/B_0)}{\mathcal{F}(d)}\right) = \mathcal{F}^{-1}\left(\left(\frac{1}{3} - \frac{k_z^2}{k^2}\right)^{-1} \mathcal{F}(b_z/B_0)\right) \tag{2.29}$$

Despite the seeming simplicity, deconvolution Eq. 2.29 is complicated by the structure of the Fourier transform $\mathcal{F}(d)$ it has a zero cone surface at the magic angle of $\alpha = \pm arccos(\sqrt{1/3}) = \pm 54.7^\circ$ (from the condition $k^2 = 3k_z^2$) with respect to the main magnetic field. This makes the inversion problem an ill-posed one with no unique solution.

Several techniques have been proposed to address this problem and back-calculate $\chi(\vec{r})$ given field distribution.

1. *Piecewise constant field inversion* simplifies the inversion problem assuming existence of regions of uniform susceptibility that can be segmented from MRI images. While being useful in simple cases, this approach is difficult to apply in realistic situations where the susceptibilities of interest often non-uniform and distributions have complex geometries.
2. *Calculation of susceptibility through multiple orientation sampling (COSMOS)* utilizes the fact that with rotation of the object in B_0, zero cone in k-space rotates as well. Thus, multiple (≥ 3) orientation sampling allows to recover points in $\mathcal{F}(\chi)$ that are not available from a single orientation data. Although often considered a golden standard, COSMOS is limited in clinical applications due to prolonged acquisition time and necessity of rotation of a subject inside the MRI scanner.

3. *Truncated k-space division (TKD)* uses substitutes all values of $\mathcal{F}(d)$ that a smaller than a predetermined threshold with a small non-zero value. While computationally efficient and easy to implement, this approach suffers from streaking artifacts and susceptibility underestimation due to improper kernel modeling.

4. *Morphology enabled dipole inversion (MEDI)* incorporates available anatomic information into the inversion problem. One of the main assumptions in MEDI is that edges in χ are very likely to be co-located with the edges in the corresponding magnitude images. This allows formulation of a minimization problem:

$$\chi(\vec{r}) = argmin_{\chi} \|w(b - d * \chi)\|_2^2 + \lambda \|M\nabla\chi\|_1 \tag{2.30}$$

Here, b is the measured field, w weighting matrix used to compensate for noise variation in the field measurements, M structural weighting matrix derived from gradients of magnitude image, λ is so-called regularization parameter.

In essence, this formulation of the inversion problem 2.30 allows to filter out non-realistic susceptibility distribution that still satisfy the Eq. 2.29, and bias the solution towards having desirable properties.

2.7 Chemical shift and water/fat separation

In diamagnetism, formation of a magnetic moment opposite to B_0 can be viewed as induction of a current in electron cloud. This induced electron current, in turn, generates a magnetic field δB, that changes resonance frequency for the nuclei in the center of the electron cloud. This phenomenon is known

as *magnetic shielding*. The difference in resonance frequencies between free and shielded hydrogen nuclei increases with increasing magnetic field strength through a scaling factor called the *chemical shift*. In many cases, hydrogen nuclei within a molecule can experience various magnetic shielding depending on their locations. This leads to a formation of a *chemical shift spectrum* that can be considered a signature of the molecular structure.

One of the most common example of chemical shift spectrum within human body is that of triglyceride molecules in fat. The main chemical l peak of fat is estimated to have the chemical shift of -3.5 parts per million (ppm) relative to water. This results in a considerably slower phase accrual rate for nuclei in fat regions, that might appear to have large offsets relative to surrounding water-based tissues in field maps estimated from Eq. 2.28. These unphysical sharp jumps in apparent field preclude straightforward application of QSM since they do not reflect the true susceptibility field, and need to be corrected.

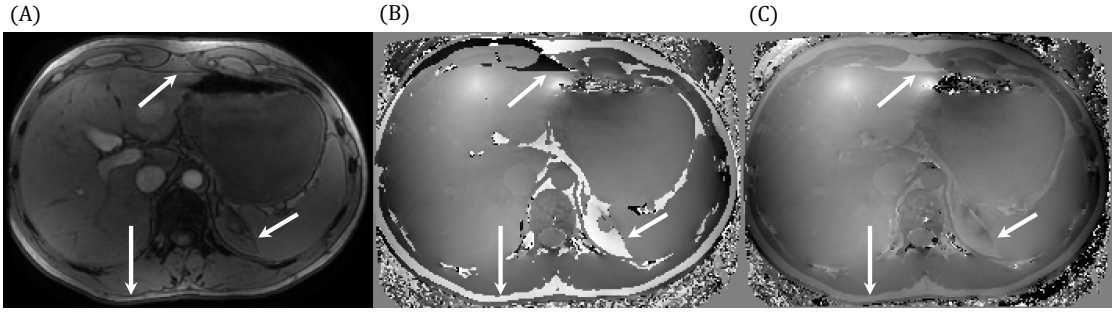

Figure 2.3: (A) Magnitude, (B) raw field map and (C) corrected field map. Subcutaneous and interstitial fat regions (arrows) manifest themselves in the raw field map with apparent frequency offsets due to chemical shift.

2.7.1 Iterative decomposition of water and fat signals

Eq. 2.28 can be extended for a case of multiple chemical species. If $f_s(\vec{r})$ is the total magnetic field induced by susceptibility sources, f_k chemical shift of the k^{th} species and $\rho_k(\vec{r})$ is its complex signal contribution at the voxel with coordinates $\vec{r}$, then the following can be written for the signal $s(\vec{r}, TE)$ at the moment of time TE:

$$s(\vec{r}, TE) = e^{-i2\pi f_s(\vec{r})TE} e^{-\frac{TE}{T_2^*(\vec{r})}} \sum_k \rho_k(\vec{r}) e^{-i2\pi f_k TE} \tag{2.31}$$

In a simplified case when only water (ρ_w) and fat (ρ_f) signals are modelled, and assuming fat has only a single component f_1 in its chemical spectrum, Eq. 2.31 becomes:

$$\begin{aligned} s(\vec{r}, TE) &= e^{-i2\pi f_s(\vec{r})TE} e^{-\frac{TE}{T_2^*(\vec{r})}} \left(\rho_w(\vec{r}) + \rho_f(\vec{r}) e^{-i2\pi f_1 TE}\right) = \\ &= e^{-i2\pi\left(f_s(\vec{r}) + i\frac{1}{2\pi T_2^*(\vec{r})}\right)TE} \left(\rho_w(\vec{r}) + \rho_f(\vec{r}) e^{-i2\pi f_1 TE}\right) = \\ &= e^{-i2\pi\psi(\vec{r})TE} \left(\rho_w(\vec{r}) + \rho_f(\vec{r}) e^{-i2\pi f_1 TE}\right) \end{aligned} \tag{2.32}$$

If N echoes are measured at specific set of TEs $(t_1, t_2, , t_N)$, Eq. 2.32 can be written in a matrix format:

$$\mathbf{s} = \mathbf{D}(\psi)\mathbf{A}\rho \tag{2.33}$$

where $\mathbf{s}$ is the $(N \times 1)$ vector of measurements

$$\mathbf{s} = \begin{pmatrix} s(t_1) \\ \vdots \\ s(t_N) \end{pmatrix} \tag{2.34}$$

diagonal $(N \times N)$ matrix $\mathbf{D}$ contains exponential terms modelling effects of $f_s(\vec{r})$

and $T_2^*(\vec{r})$

$$\mathbf{D} = \begin{pmatrix} e^{-i2\pi\psi(\vec{r})TE_1} & \cdots & 0 \\ \vdots & \ddots & \vdots \\ 0 & \cdots & e^{-i2\pi\psi(\vec{r})TE_N} \end{pmatrix} \tag{2.35}$$

$(N \times 2)$ matrix $\mathbf{A}$ describes signal temporal behavior due to chemical shift

$$\mathbf{A} = \begin{pmatrix} 1 & e^{-i2\pi f_1 TE_1} \\ \vdots & \vdots \\ 1 & e^{-i2\pi f_1 TE_N} \end{pmatrix} \tag{2.36}$$

and ρ is the (2×1) vector of signal components

$$\rho = \begin{pmatrix} \rho_w \\ \rho_f \end{pmatrix} \tag{2.37}$$

With sufficient number of echoes and an initial guess $\hat{\psi}$ for ψ, estimate for the signal from each chemical species can be obtained in the least-squares fashion by performing the Moore-Penrose pseudoinverse, i.e.:

$$\hat{\rho} = (\mathbf{A^H A})^{-1}\mathbf{A^H D}(-\hat{\psi})\mathbf{s} \tag{2.38}$$

Since $\hat{\psi}$ is only an approximation, relatively large errors might manifest in $\hat{\rho}$. To address these imperfections, the inversion process is usually repeated iteratively: the error $\Delta\psi$ is calculated based on $\hat{\rho}$, and $\hat{\psi}$ is updated; after this updated $\hat{\rho}$ can be estimated. The procedure is repeated until $\Delta\psi$ is small enough. As a result, a corrected field map $f_s(\vec{r})$ can be obtained and used further in QSM calculations.

In practical applications, signal model Eq. 2.32 is often extended to account for complex nature of chemical shift spectrum. In this dissertation, application-specific extensions of water/fat model are described.

CHAPTER 3

JOINT ESTIMATION OF CHEMICAL SHIFT AND QUANTITATIVE SUSCEPTIBILITY MAPPING

Purpose: The purpose of this work is to address the unsolved problem of quantitative susceptibility mapping (QSM) of tissue with fat where both fat and susceptibility change the MR signal phase.

Methods: The chemical shift of fat was treated as an additional unknown and was estimated jointly with susceptibility to provide the best data fitting using an automated and iterative algorithm. A simplified susceptibility model was used to calculate an updated value of the chemical shift based on the local magnetic field in each iteration. Numerical simulation, phantom experiments and in vivo imaging were performed. Artifacts were assessed by measuring the susceptibility variance in uniform regions. Accuracy was assessed by comparison with ground truth in simulation, and using a susceptibility matching approach in phantom.

Results: Using the proposed method, artifacts on the QSM image were markedly suppressed in all tested datasets compared to results generated using fixed chemical shifts. Accuracy of the estimated susceptibility was also improved in numerical simulation and phantom experiments.

Conclusion: A joint estimation of fat content and magnetic susceptibility using an iterative chemical shift update was shown to improve image quality and accuracy on QSM images.

3.1 Introduction

Quantitative susceptibility mapping (QSM) in MRI has received increasing clinical and scientific interest [1–14]. QSM contrast originates from the magnetic moments of the electrons orbiting around the nuclei in a molecule, and provides a valuable venue to exploit the full utility of the usually discarded phase images in MRI. It has shown promise in characterizing and quantifying molecular compositions such as iron, calcium, and gadolinium, making it relevant to the diagnosis and treatment of various neurological disorders [15–26].

Most of the existing QSM methods assume that susceptibility is the only contributor to the field inhomogeneity, which may be a valid assumption for applications in neuroimaging. However, the same orbiting electron cloud response to B0 in molecules also magnetically shields the nuclei inside the electron cloud [27–29]. The shielded protons in the molecule have a resonance frequency different from that of the unshielded ones, and this resonance frequency offset is referred to as chemical shift [30]. This chemical shift affects the complex MRI signal, particularly the signal phase, because the shielded protons contribute to signal generation as well. Although estimation of the field inhomogeneity in the presence of chemical shift has been proposed in various algorithms such as Iterative Decomposition of water and fat with Echo Asymmetry and Least squares estimation (IDEAL) [31, 32], these algorithms typically assume that the chemical spectrum is known a priori. Since the chemical spectrum may vary between subjects or even between organs within the same subject due to the differences in lipid compartmentalization and fatty acids content [33, 34], the assumed chemical spectrum may not be accurate enough for the subsequent determination of susceptibility. Moreover, even using multi-peak models, ambi-

guity exists in how to assign the main components of the spectrum: the location of the central line (containing 60-85% of the overall fat signal) reported in the literature varies within a 0.2 ppm range [35–37]. Another factor is the temperature dependence of the fat chemical shift [38]. The underdetermined chemical spectrum adds another layer of numerical difficulty for faithful field map estimation in water/fat separation. In this work, we present an automated joint estimation of the chemical shift and the susceptibility from an MRI dataset, where the chemical shift is also treated as an unknown variable subject to optimization. We refer to this method as chemical QSM. Through simulations, phantom validation, and in vivo data, it is demonstrated that this method yields higher quality QSM images, and enables QSM applications beyond neuroimaging.

3.2 Theory

The field inhomogeneity in MRI can be measured using a multi-echo gradient echo sequence [7,39]. The reconstructed image signal s of a voxel at a spatial location $\vec{r}$ measured at the n^{th} echo time TE_n may be expressed as:

$$s(\vec{r}, TE) = e^{-i2\pi f_s(\vec{r})TE_n} e^{-R_2^*(\vec{r})TE_n} \sum_k \rho_k(\vec{r}) e^{-i2\pi f_k TE_n} \tag{3.1}$$

where $f_s(\vec{r})$ is the spatially varying field induced by the susceptibility referred to as susceptibility field, $R_2^*(\vec{r})$ is the apparent transverse relaxation rate for the voxel, m is the number of chemical species present in the voxel, f_k is the chemical shift constant of the kth species, and $\rho_k(\vec{r})$ is the contribution of the k^{th} species to the complex signal of the voxel at $TE = 0$. After excitation, the signal experiences dephasing due to the chemical shift and the susceptibility field. For simplicity, the spatial index $(\vec{r})$ of any scalar field will be dropped hereafter when-

ever clarity is not affected. Each species is characterized by two parameters: ρ_k and f_k. The parameters of different species may be independent, such as water and fat, or correlated, such as different components of fat. In the scenario where only water [ρ_0, f_0] and a single fat peak [ρ_1, f_1] are present, Eq. 3.1 becomes:

$$s(\vec{r}, TE) = e^{-i2\pi f_s(\vec{r})TE_n} e^{-R_2^*(\vec{r})TE_n} \left(\rho_0(\vec{r}) + \rho_1(\vec{r}) e^{-i2\pi f_1 TE_n}\right) \tag{3.2}$$

Here, we assumed that the chemical shift of water is zero: $f_0 = 0$ as the water resonance frequency is used as the reference frequency, such that any deviation is absorbed into f_s.

3.2.1 Challenges in previous attempts for estimating f_s

Previous algorithms estimate f_s and $[\rho_k]_{k=0,1}$ by assuming f_k is known a priori and minimizing a cost function that is the residual between the modeled and the measured signals over N different TEs:

$$\begin{aligned} &f_s^*,\ R_2^{**},\ [\rho_k^*]_{k=0,1} = \\ &= argmin_{f_s,\ R_2^*,\ [\rho_k]_{k=0,1}} \sum_{n=1}^{N} \left\| s(TE_n) - e^{-i2\pi f_s(\vec{r})TE_n} e^{-R_2^*(\vec{r})TE_n} \left(\rho_0(\vec{r}) + \rho_1(\vec{r}) e^{-i2\pi f_1 TE_n}\right) \right\|_2^2 \end{aligned} \tag{3.3}$$

The fat frequency f_1 is often assumed to be between -3.5 and -3.4 parts per million (ppm) [35–37, 40]. The uncertainty in the fat chemical shift has a substantial effect on the estimation of f_s^*, the inhomogeneity field map. This can be best understood by examining the signal behavior in a voxel consisting of fat

only, where Eq. 3.3 reduces to the following:

$$f_s^* = argmin_{f_s} \sum_{n=1}^{N} \left\| s(TE_n) - |s(TE_n)| e^{-i2\pi(f_s+f_1)TE_n} \right\|_2^2 \tag{3.4}$$

Here any error $\Delta f1$ in the presumed chemical shift f_1 enters into the estimate f_s^*, because the cost function only depends on the sum of f_s and f_1. As the susceptibility under investigation is often on the order of 0.01 ppm to 0.1 ppm [4], a 0.1 ppm error in the field map is very large and complicates a meaningful measurement of susceptibility. Therefore, it is desirable to treat f_1 as an additional unknown variable to be optimized.

To formulate the problem where the chemical shift frequency f_1 is treated as an additional unknown, the following energy function is minimized:

$$\begin{aligned} &f_s^*,\ R_2^{**},\ f_1^*,\ [\rho_k^*]_{k=0,1} = \\ &= argmin_{f_s,\ R_2^*, f_1,\ [\rho_k]_{k=0,1}} \sum_{n=1}^{N} \left\| s(TE_n) - e^{-i2\pi f_s(\vec{r})TE_n} e^{-R_2^*(\vec{r})TE_n} \left(\rho_0(\vec{r}) + \rho_1(\vec{r}) e^{-i2\pi f_1 TE_n} \right) \right\|_2^2 \end{aligned} \tag{3.5}$$

This is a high dimensional non-linear data fitting problem. It is possible to solve it by discretizing f_1, solving Eq. 3.3 for all voxels for a fixed f_1, and selecting the f_1 with minimal energy. However, this brute force search is computationally intensive and the precision is still subject to the discretization error in f_1. Additionally, solving Eq. 3.3 for all voxels often involves smoothness assumption on f_s^*, which is not desirable for QSM. Instead, f_s^* is assumed to be generated by a physical susceptibility distribution according to the dipole convolution $f_s = d * \chi$, where d is the field of a unit dipole and χ is the susceptibility distribution [2,41,42]. When a non-dipole field exist in f_s, the mismatch between model and the input data f_s, leads to streaking artifacts in the reconstructed susceptibility map. The typical streaking artifacts can be found algorithmically

by detecting spurious edges that do not correspond to any anatomical features found in the magnitude image or in the T1- and T2-weighted images acquired in the same subject [8]. The anatomical features can be represented in various mathematical forms, such as edges. The correct f_s would have minimal artifacts. The mathematical formulation used in this work is:

$$f_1^*, \chi^* = \\ = argmin_{f_1,\chi} \lambda \sum_{n=1}^{N} \left\| s(TE_n) - e^{-i2\pi d*\chi TE_n} e^{-R_2^*(\vec{r})TE_n} \left(\rho_0(\vec{r}) + \rho_1(\vec{r}) e^{-i2\pi f_1 TE_n} \right) \right\|_2^2 + |MG\chi| \tag{3.6}$$

where ρ_0 and ρ_1 may be treated as variables depending on the susceptibility field $d*\chi$ and chemical shift f_1 through variable projection (VARPRO) [37], G is the 3D gradient operator, M is an edge mask derived from the gradient of an anatomical prior obtained from the same MRI dataset [8], and λ is the Lagrangian multiplier whose value may be determined using Morozovs discrepancy principle [43].

3.3 Methods

3.3.1 Iterative correction of the fat chemical shift

To avoid the brute force search over f_1, this highly nonlinear and multidimensional problem defined by Eq. 3.6 was solved iteratively by performing a susceptibility calculation at only a few selectively updated f_1 values through the following approximation. It has been shown that water and fat have a susceptibility difference around 0.6ppm, which is much greater than susceptibility variations (0.01 ppm ~ 0.1 ppm) reported in normal tissue [8]. Thus, the susceptibility map was approximated to have two types of major sources, namely,

water and fat, each having a constant but unknown susceptibility. This model was fit against the susceptibility field map estimated by a multi-echo Dixon water/fat separation method assuming a fixed chemical shift. Then any systematic discrepancy between the modeled and estimated susceptibility field map allows us to correct the chemical shift. Consequently, the reconstruction is split into two stages. In the first stage, we correct the presumed chemical shift based on the piece-wise constant model introduced above. In the second stage, we removed the piece-wise constancy constraint to allow per-voxel susceptibility mapping. A flowchart of the method is presented in Fig. 3.1, where images are from an actual phantom (see the lard experiment section below). The specific implementation of each step is as follows.

Step 0: As one of the cornerstones of the algorithm, the T_2^*-IDEAL algorithm [32] was used for the mapping of water, fat and susceptibility field. Since the nonlinear minimization performed in IDEAL may converge to a local minimum, it is important to select an initial susceptibility field that is reasonably close to the true solution. Here, we used the observation that the susceptibility field measured in MRI is typically dominated by the background field [13, 44], which was defined here as the field generated by sources of susceptibility outside the region of interest. An important example of this is the air-tissue interface, which represents a susceptibility shift of around 9 ppm. In QSM, it is necessary to estimate the background field such that the local field can be obtained, defined here as the field generated by sources of susceptibility inside the region of interest. Consequently, the relationship was written as $f_s = f_B + f_L$, with f_B and f_L the background and local field, respectively. Several algorithms have been developed to separate the background field f_B from f_L [13, 44]. Since we assumed that $f_L \ll f_B$, we used the obtained background field f_B as the initial

susceptibility field for the T_2^*-IDEAL algorithm.

Before background field estimation was carried out, a preliminary field map was estimated assuming a single species. Using the finding that discontinuities between neighboring voxels on this preliminary field map were generally caused by either the limited dynamic range determined by the finite echo spacing ΔTE, or the chemical shift f_1, these discontinuities were removed by unwrapping field jumps $\frac{n}{\Delta TE} + mf_1^0$, where $\frac{n}{\Delta TE}$ is the standard 2π wrap-around with n an integer, and mf_1^0 is the chemical shift jump with $m = 0$ or 1. This unwrapping was performed with a magnitude-guided field unwrapping algorithm [45] and used an initial guess of the fat chemical shift value $f_1^0 = -3.5ppm \cdot \gamma B_0$ Hz. The background field was then obtained by applying the projection onto dipole field (PDF) [44] method on the unwrapped field.

Step 1: In this step, an initial guess $f_1^{(k-1)}$ for the chemical shift was assumed and kept fixed. The water fraction map, defined as $\rho_0/(\rho_0 + \rho_1)$, the fat fraction map, defined as $\rho_1/(\rho_0 + \rho_1)$, and the susceptibility map $f_s^{(k)}$ were calculated using T_2^*-IDEAL [31]. Note that no final smoothing of the field map $f_s^{(k)}$ was performed, in contrast to what is done conventionally.

Step 2: A local field $f_L^{(k)}$ was estimated from the susceptibility field $f_s^{(k)}$ again using the Projection onto Dipole Fields (PDF) method(44).

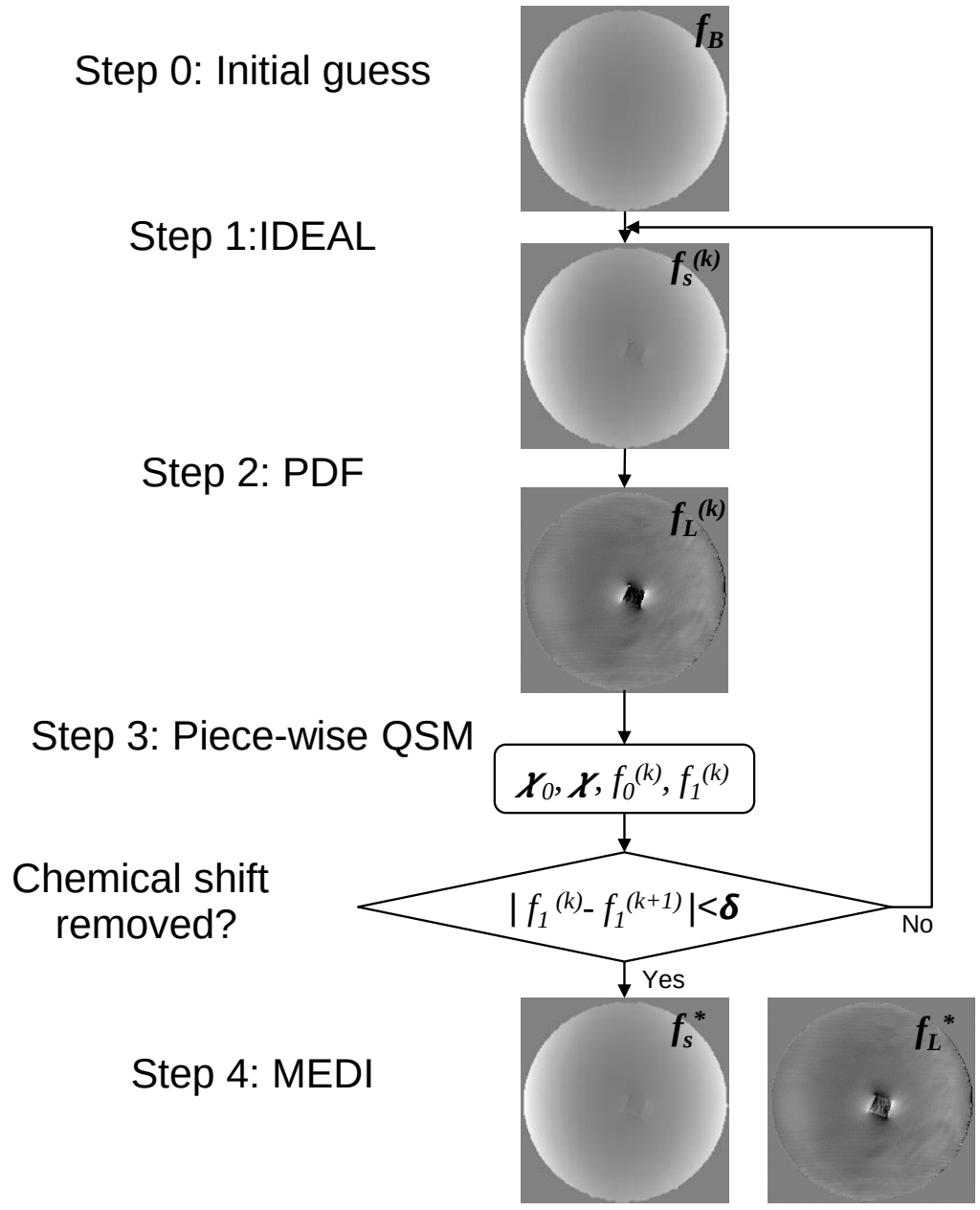

Figure 3.1: Flowchart of the proposed algorithm. Symbols are defined in the text. Note that local field is updated at step 4 compared to step 2.

Step 3: Both water and fat were assumed to have constant, but unknown chemical shifts and magnetic susceptibilities. With this assumption, a previously reported piece-wise constant inversion of the magnetic field distribution [4, 46] was implemented to estimate these susceptibilities and chemical shifts. The difference Δf_1 in the chemical shift between water and fat estimated in this step was then used to update the chemical shift of fat for the next iteration: $f_1^{(k)} = f_1^{(k-1)} + \Delta f_1^{(k)}$. The assumption that water and fat components have constant susceptibilities is not satisfied in general but is only made in this step to simplify the problem of the chemical shift update. This assumption is not made at the final susceptibility estimation step.

Step 4: steps 1-3 were repeated using the new chemical shift estimate $f_1^{(k)}$ until the chemical shift update $\Delta f_1^{(k)}$ was smaller than a certain preset threshold. Otherwise, the field map $f_s^{(k)}$ was passed to the morphology enabled dipole inversion (MEDI) method [45] for per-voxel QSM.

3.3.2 Numerical phantom simulations

Two numerical phantoms with a $128 \times 128 \times 64$ matrix size were constructed to test the feasibility of the proposed approach and evaluate its performance in different conditions. For the first simulation, the phantom consisted of a centered $109 \times 109 \times 49$ voxel volume of water with an imbedded cylinder of fat with a diameter of 7 voxels, oriented perpendicularly to the main magnetic field B_0 ($B_0 = 3T$) (Fig. 3.2A). The fat chemical shift was assumed to consist of a single peak at f1 = -3.60 ppm, while its susceptibility was assumed to be 0.6 ppm. The background field was modeled as a linear gradient across the phan-

tom. The second phantom consisted of $109 \times 109 \times 49$ volume of water centered in the field of view. It contained eight cylinders with different diameters (3, 7 and 10 voxels were used) each having a mixture of water and fat in different proportions, leading to 100%, 95%, 87.5%, 75%, 62.5%, 50%, 37.5% and 25% fat fractions. Fat was assumed to have a multi-peak spectrum with frequencies f_k = {-3.82, -3.46, -2.74, -1.86, -0.50, 0.53} ppm and corresponding relative amplitudes α_k=0.01{$9.45e^{-i\pi 0.181}$, 64.66, $9.67e^{i\pi 0.046}$, $2.26e^{-i\pi 0.567}$, $2.22e^{-i\pi 0.244}$, $8.83e^{-i\pi 0.089}$}. These relative amplitudes were reported in a previous study [35]. All cylinders were oriented perpendicularly to the B_0 field (B_0 = $3T$). The background field was modeled by imposing a linear field gradient across the phantom. The susceptibility of fat was still assumed to be 0.6 ppm. For both phantoms, MRI data was simulated using the following scan parameters: TE_1 = 2.5ms, TE spacing ΔTE=0.75ms, Number of echoes #TE = 15, and voxel size = $1 \times 1 \times 1$ mm^3. In all simulations, complex Gaussian noise was added to the signal, producing a peak signal-to-noise ratio (PSNR) of 30. The proposed algorithm which assumed a single fat peak used an initial guess of -3.46 ppm (main peak of the multi-peak spectrum) for the chemical shift $f_1^{(0)}$.

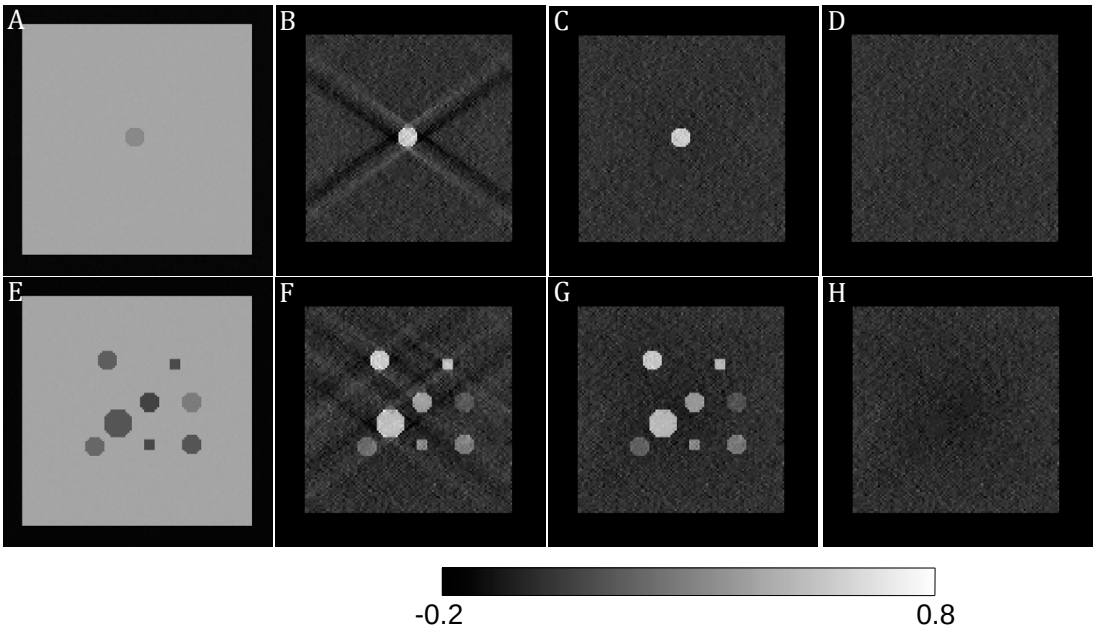

Figure 3.2: Results of the numerical experiments: comparison of QSM maps reconstructed using conventional T_2^*-IDEAL and proposed algorithm (first row: one-peak fat spectrum, second row: multi-peak fat spectrum). (A), (E): T2*-weighted images of the simulated phantoms. (B), (F): QSM images reconstructed from the susceptibility field fs estimated with assumption of the chemical shift value f_1 = -3.46 ppm. (C), (G): QSM images reconstructed from the susceptibility field f_s estimated with proposed iterative algorithm. (H), (I): Difference between QSM maps reconstructed from the susceptibility fields fs estimated with proposed algorithm and the true susceptibility maps. Note that significant suppression of the streaking artifacts was achieved using the proposed algorithm in (C) and (G).

3.3.3 Lard phantom experiment

To validate the accuracy of estimated susceptibility using the proposed method, a phantom experiment was performed using a susceptibility matching approach as the reference standard. The phantom experiment was performed on a 3T MRI system (GE Excite HD, Milwaukee, WI) using an 8-channel head coil. The phantom consisted of a container filled with a known volume of water and a fixed stick of lard (Pinnacle Foods Group LLC, Parsippany, NJ). A series of acquisitions with identical scan parameters ($TE_1 = 2.7$ms, $\Delta TE = 3.3$ms, $\#TE = 8$, TR = 29.4ms, FA = 15°, BW = ±62.5kHz) were performed. Between successive acquisitions, a solution with a fixed and known concentration of Gd was added to the water, thus gradually increasing the susceptibility of the water surrounding the lard. The range of obtained susceptibilities was between 0 and 0.5ppm, with a step size of 0.01ppm between 0.23 ppm to 0.43 ppm. Three analyses were performed:

a) When the susceptibility of the water solution matched that of lard, no or very low variations of the local magnetic field are expected, since the characteristic paramagnetic dipole pattern of fat vanishes in this situation. This susceptibility match was found by computing the norm of the local magnetic field (obtained with linear fitting alone) outside the lard fat region and selecting the acquisition with the smallest norm. The susceptibility of lard was then obtained by converting the Gd concentration in the phantom into susceptibility using the following formula: $\chi_{solution} = \chi_{mol,Gd} \cdot [Gd]$, where $\chi_{mol,Gd}$ is the molar susceptibility of Gd, $\chi_{mol,Gd} = 326\ ppm/M$

b) For each acquisition, the lard susceptibility relative to the phantom Gd solution was obtained using a piece-wise constant method previously pro-

posed [4], except for the background field removal step, which was performed using the projection onto dipole fields method. Gd concentrations were converted to susceptibility as in a).

c) Finally, for each acquisition, a field map was obtained with the proposed method (using -3.46 ppm as an initial guess) and then used to reconstruct a susceptibility map using MEDI. The lard susceptibility relative to Gd solution was derived from the Gd concentration as in a).

3.3.4 Bovine tissue experiment

A piece of excised bovine tissue containing intramuscular fat was scanned on a 3T MRI system (GE Excite HD, Milwaukee, WI) using an 8-channel head coil. A multi-echo 3D SPGR sequence was used for data acquisition with imaging parameters: TE_1=2.5ms, ΔTE=2.25ms, 7 echoes, 3 acquisitions with TE_1 incremented by 0.75ms between acquisitions, TR=19ms, FA=20°, BW=±62.50 kHz, voxel size = $0.94 \times 0.94 \times 1\ mm^3$ and scan time ≈9 minutes. The proposed algorithm was performed on the first 15 of the acquired echoes and used an initial guess of -3.46 ppm for the chemical shift $f_1^{(0)}$. We also performed the reconstruction using 6 of the acquired echoes with an echo spacing ΔTE=3ms to test the robustness of the proposed technique with respect to the choice of echo spacing and echo number.

3.3.5 Volunteer breast scan

After obtaining informed consent, four female volunteers were scanned. All exams were performed under protocols approved by the Institutional Review Board. Images were obtained using a 3T MRI system (MAGNETOM Verio, Siemens Healthcare, Erlangen, Germany) using a 16 channels (8 channels per breast) breast coil (Invivo, Gainesville, FL). A multi-echo spoiled gradient echo sequence was used for the exams using the following imaging parameters: TE_1= 3.3ms, ΔTE=3.3ms, #TE=8, TR=35ms, FA=20°, BW=±62.50 kHz, and voxel size = $1 \times 1 \times 1$ mm^3. The proposed algorithm was performed on the resulting images and used an initial guess of -3.46 ppm for the chemical shift $f_1^{(0)}$.

3.3.6 Image processing and analysis

In the iterative correction of the fat chemical shift, a precision of 1 Hz was set as the convergence level for all the experiments. In the numerical simulations, where the ground truth was available, the improvements after the chemical shift correction were assessed by calculating the difference between the estimated (χ^*) and true (χ_0) susceptibility maps relative to the noise level. This measure was defined as

$$\|\chi^* - \chi_0\|_2^2 / \sigma^2 \tag{3.7}$$

where σ^2 is the expected energy of noise on the reconstructed susceptibility map. This value was estimated as $\sigma^2 \approx \|\chi_t - \chi_0\|_2^2$, where χ_t is the susceptibility map reconstructed from the noisy field map with the chemical shift fixed to its ground truth value. When the algorithm converges to the correct chemical shift, this measure should be 1.

For the phantom experiments, image artifacts were assessed by measuring the standard deviation of susceptibility values in uniform regions, such as the Gd solution region outside the lard in the lard experiment, and the muscle region in the bovine tissue experiment.

For in vivo experiments, fitting residuals

$$Res\left(f_1^{(k)}\right) = \sum_{n=1}^{N} \left\| s(TE_n) - e^{-i2\pi f_s^{(k)} TE_n} e^{-R_2^* TE_n} \left(\rho_0^{(k)} + \rho_1^{(k)} e^{-i2\pi f_1^{(k)} TE_n}\right) \right\|_2^2 \qquad (3.8)$$

were recorded, where $f_s^{(k)}$, $R_2^{*(k)}$, $\rho_0^{(k)}$ and $\rho_1^{(k)}$ were estimated from T_2^*-IDEAL [32] once $f_1^{(k)}$ was known.

3.4 Results

3.4.1 Numerical experiments

In each case, the convergence of the updated chemical shift value was reached within 10 iterations. Reconstructed QSM maps are shown in Fig. 3.2. It can be noted that the one-peak model with the use of chemical shift correction was able to produce improved results compared to the non-corrected models (Fig. 3.2, B and C, F and G). Reconstruction of the single-peak phantom using the fixed one peak model (-3.46 ppm) resulted in a relative error of 1.656; the proposed chemical shift update, which converged to ≈-3.6 ppm, led to an error reduction down to 1.01. Reconstruction of the multi-peak phantom using the fixed main peak model (-3.46 ppm) resulted in the relative error of 1.304, and proposed chemical shift update, which converged to -3.55 ppm, allowed to reduce this value to 1.01.

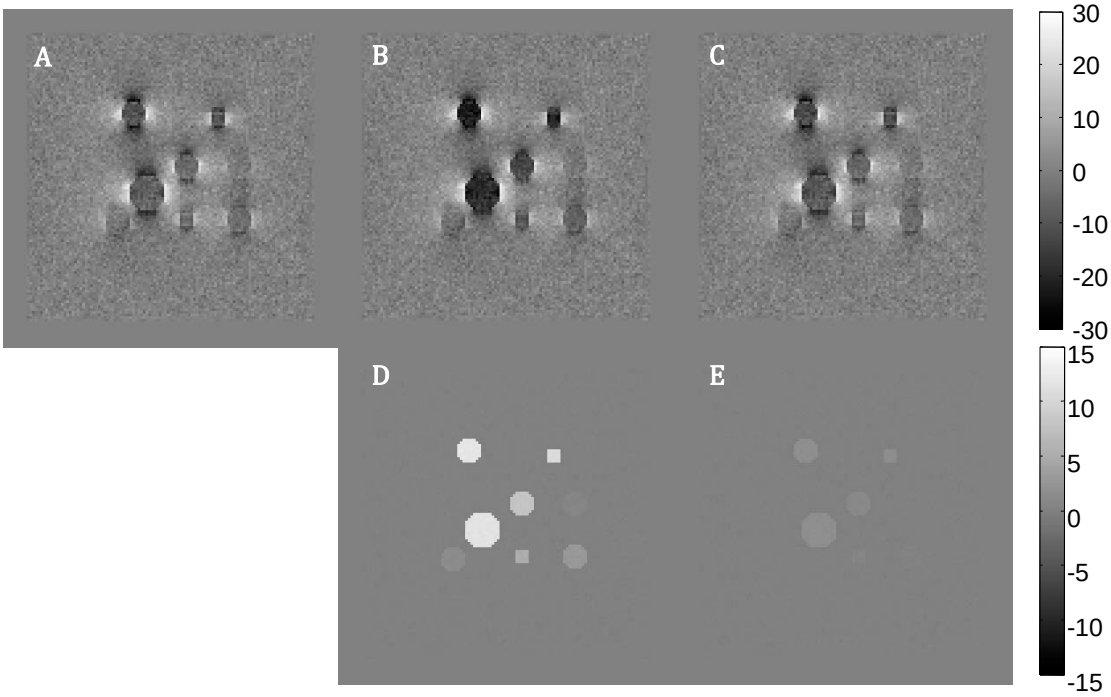

Figure 3.3: Results of the numerical experiments: comparison of local field maps reconstructed using conventional T_2^*-IDEAL and proposed algorithm. (A): local field map reconstructed with the true spectrum. (B): local field map reconstructed with assumption of the chemical shift value f_1 = -3.46 ppm. (C): local field map reconstructed using the proposed algorithm. (D), (E): Difference between (A) and (B), and (A) and (C), respectively. It can be seen that frequency offset in regions with high fat content is reduced after correction of the chemical shift in (C) and (E).

Fig. 3.3 shows a comparison of the local field maps estimated using the true multi-peak chemical spectrum, the fixed one peak model (main peak) and the proposed algorithm. The assumption of a fixed peak led to an absolute error on the order of 10 Hz in the fat region pointed by arrows. The proposed method reduced this error down to 1.5 Hz.

Finally, Fig. 3.4 shows a comparison between the true fat fraction map used in the numerical simulation and the fat fraction map estimated using the fixed

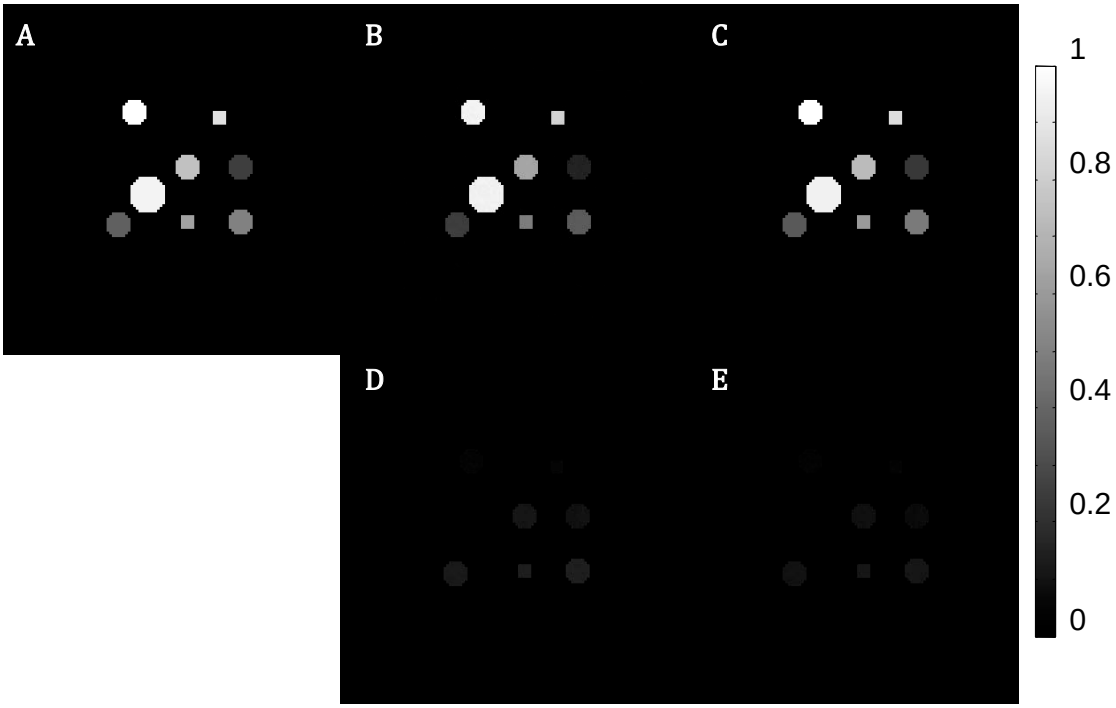

Figure 3.4: Results of the numerical experiments: comparison of fat fraction maps reconstructed with different assumed spectra. A: true fat fraction map. B: fat fraction maps reconstructed with assumption of the chemical shift value f_1 = -3.46 ppm. C: fat fraction maps reconstructed using the proposed chemical shift update. D, E: Difference between A and B, and A and C, respectively. Both B and C showed similar fat fraction maps with respect to the truth.

main peak and using the proposed algorithm. The error in the voxels containing mixtures of species was around 10% both for the fixed model and the proposed method.

3.4.2 Lard phantom results

Results of the lard susceptibility matching measurement are shown in the Fig. 3.5. It was found that the norm of the local field was minimal when the

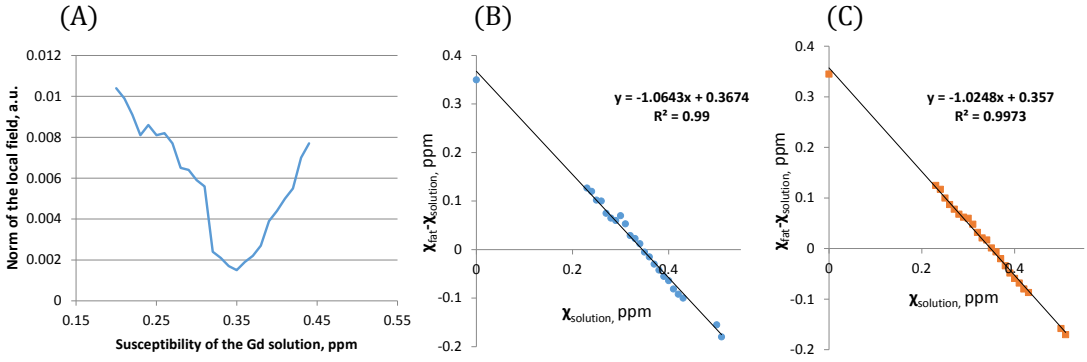

Figure 3.5: Lard experiment. (A): Dependence of the lard susceptibility field variation on the susceptibility of the Gd solution. (B): Results of the piece-wise estimation of the lard susceptibility relative to the background solution for different concentrations of Gd. (C): Results of the lard susceptibility using the proposed algorithm for different concentrations of Gd. The susceptibility values of lard estimated using three different techniques were in good agreement.

susceptibility of the background Gd solution was equal to 0.35 ppm (Fig. 3.5A). Results of the piece-wise estimation of the lard relative susceptibility are shown in Fig. 3.5B. The plot shows that the susceptibility difference between lard and the phantom background decreases linearly with increasing Gd concentration. The susceptibility of lard (0.37 ppm) is obtained by taking the intercept of the linear fit of this data. Results of the susceptibility estimation using the proposed algorithm are shown in the Fig. 3.5C. For each acquisition, the chemical shift converged to a value of -3.65 ppm. Again, the estimated relative susceptibility of lard followed the same linear trend, with an intercept of 0.36 ppm.

The QSM and corresponding field maps without added Gd are shown in Fig. 3.6. A considerable reduction in streaking artifact was observed with the proposed method (Fig. 3.6C, standard deviation outside lard was 0.01 ppm)

compared to using a fixed chemical shift (Fig. 3.6B, standard deviation outside lard was 0.05 ppm).The accuracy of the estimated susceptibility of lard was improved in the proposed method (0.35 ppm) compared to using a fixed chemical shift (0.27 ppm).

3.4.3 Bovine tissue experiment results

Fig. 3.7 shows a comparison of the QSM maps obtained for the bovine tissue scan without and with the use of the chemical shift update both for the 15 and 6 echo datasets. A marked reduction of streaking artifacts was noticed, with the standard deviation of the susceptibility values within a muscle region reduced from 0.27 to 0.12 ppm for the 15 echo data and from 0.26 to 0.15 ppm for the 6 echo data. Good visual agreement was observed between these two reconstructions with chemical shift update (Figs. 3.7C&E), although the SNR appeared to be higher in Fig. 3.7C that utilized more echoes. Overall improved preservation of the complex anatomical structure was observed in the updated chemical shift model, which converged to -3.6 ppm, compared to the fixed chemical shift reconstruction, which used -3.46 ppm).

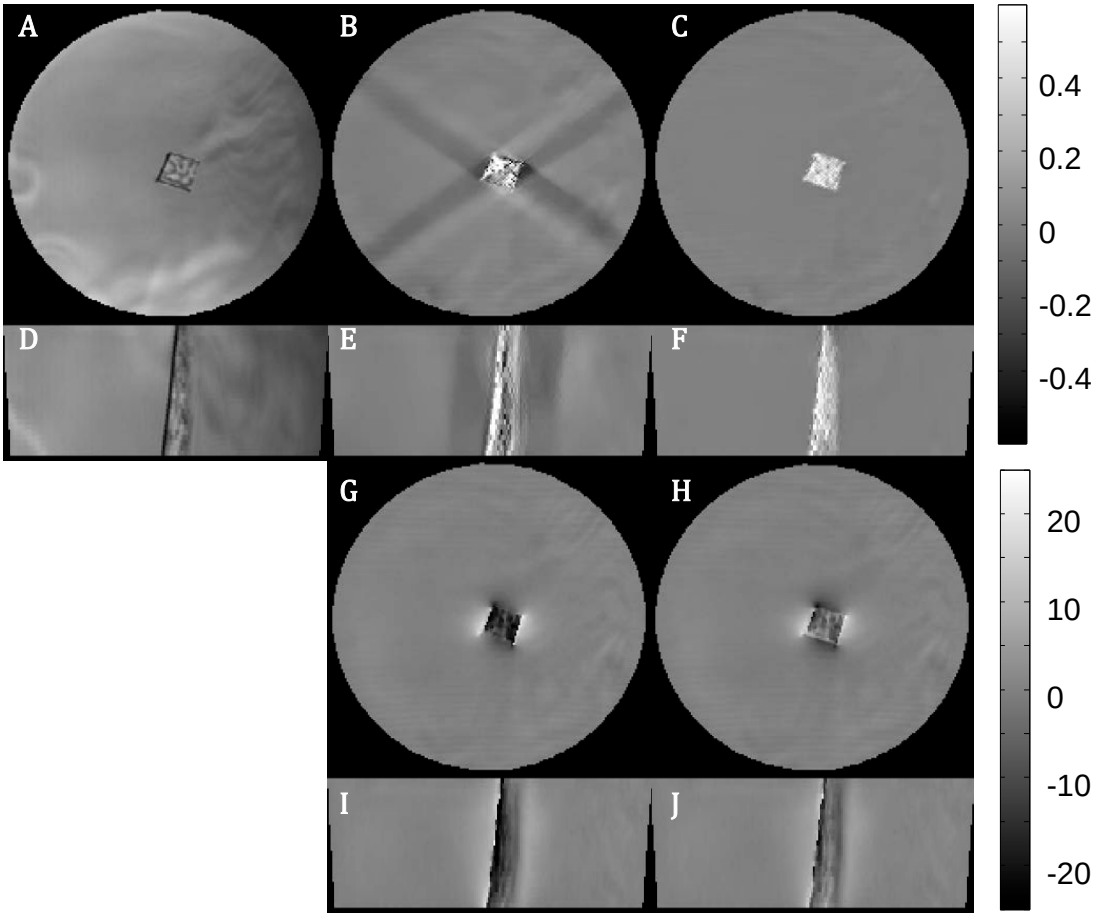

Figure 3.6: Reconstructed local field maps and QSM of the lard experiment. (A), (D): Magnitude image. (B), (E): QSM image reconstructed from the susceptibility field f_s estimated with assumption of the chemical shift value f_1 = -3.46 ppm. (C), (F): QSM image reconstructed from the susceptibility field fs estimated with proposed iterative algorithm. (G), (I): local field map corresponding to (B), (E), and (H), (J): the local field map corresponding to (C), (F). Images (A)-(C), (G), and (H) are coronal views. Images (D)-(F), (I), and (J) are sagittal views. Note the frequency offset in the lard region in the local field (G), (I) and the resulting artifact in the susceptibility map (B), (E) for the fixed chemical shift reconstruction. These are similar to those observed in numerical simulations in Fig. 3.3, and the artifacts are suppressed using the proposed algorithm as shown in (C) and (F).

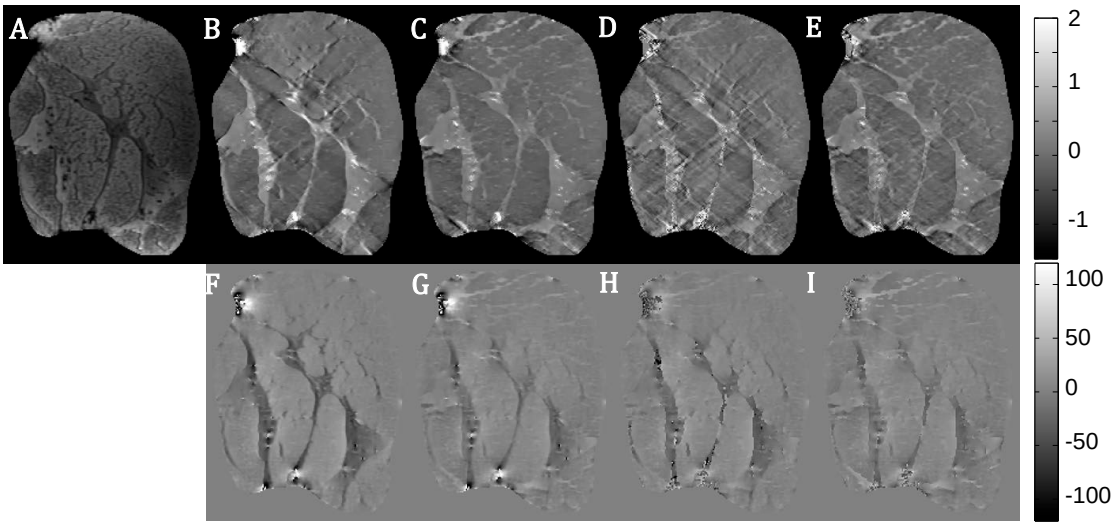

Figure 3.7: Results of the bovine tissue experiment: comparison of QSM maps reconstructed using conventional T_2^*-IDEAL and the proposed algorithm from 15 and 6 echo data. A: T_2^*-weighted image. (B), (D): QSM image reconstructed from the susceptibility field f_s estimated with assumption of the chemical shift value f_1 = -3.46 ppm using 15 and 6 echoes, respectively. (C), (E): QSM image reconstructed using the proposed iterative algorithm using 15 and 6 echoes, respectively, (F)-(I) are the local fields corresponding to (B)-(E), respectively. The proposed chemical shift update suppresses streaking artifacts for both datasets, although the use of more echoes resulted in a higher quality susceptibility map.

3.4.4 Volunteer breast scan

Results of the breast QSM experiments are shown in the Fig. 3.8 and Fig. 3.9. Fig. 3.8 shows a comparison of the QSM maps obtained without (-3.46 ppm) and with using the proposed chemical shift update algorithm, which converged to -3.3 ppm, with the results of the mammography study. The detected hypointensities in the QSM image correspond to the hyperintensities in the x-ray image and were confirmed by an experienced radiologist to be calcifications.

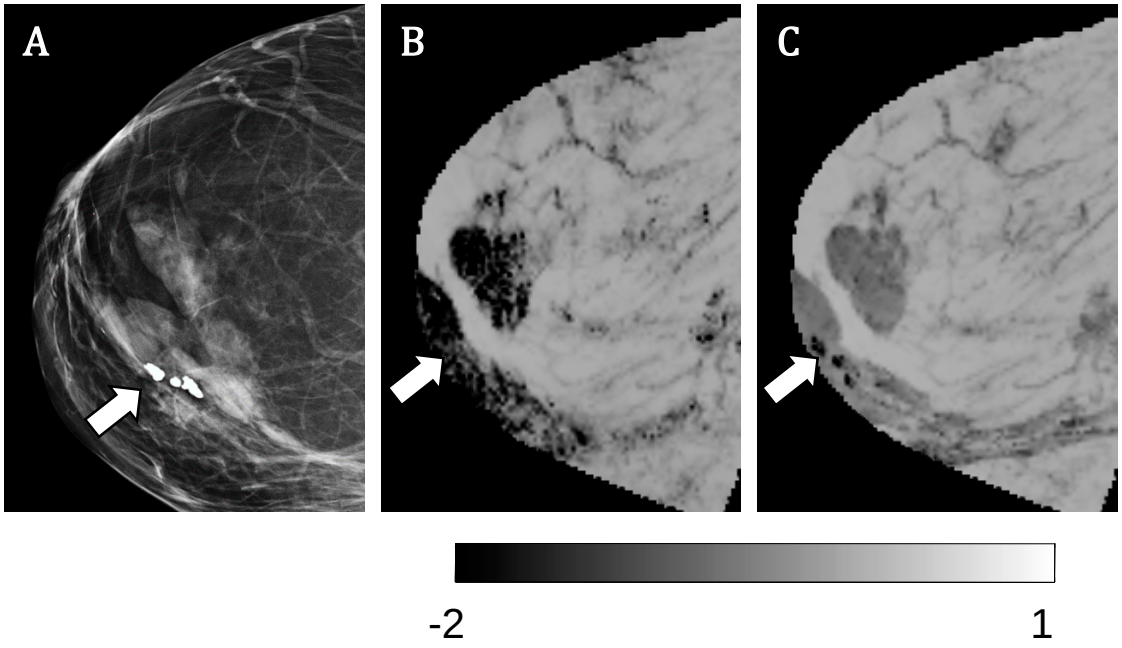

Figure 3.8: Comparison of mammogram (A) with minimal intensity projections of breast QSMs reconstructed without (B) and with (C) the proposed algorithm. Arrows point to the detected calcifications, which are better seen in the map reconstructed with the proposed method as compared to that reconstructed with the fixed chemical shift reconstruction.

Fig. 3.9 shows a comparison of the QSM maps obtained for the breast exam in a second subject without (-3.46 ppm) and with the use of the chemical shift update, which converged to -3.3 ppm. In QSM, a high susceptibility structure (1.3 ppm) was identified, and was confirmed to be a biopsy clip. Fig. 3.10 shows the residual as a function of the chemical shift value for this data set, with each "+" representing consecutive steps of the proposed algorithm starting from an initial guess for f_1 that was intentionally set to -3.8 ppm.

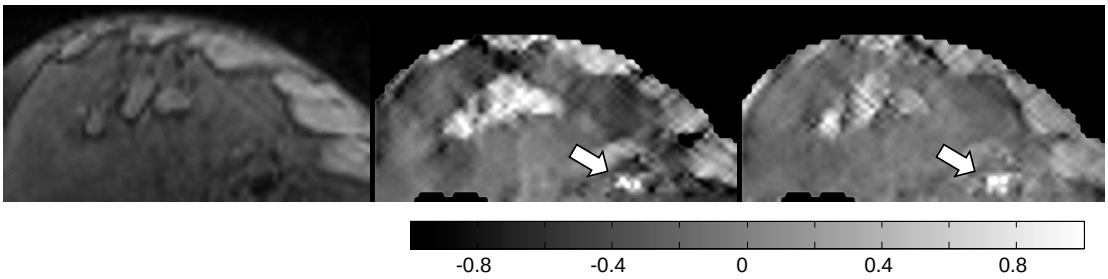

Figure 3.9: Results of a volunteer breast contrast exam (post Gd injection images are shown): comparison of QSM maps reconstructed using a fixed chemical shift (B) and the proposed algorithm (C). A T_2^*-weighted image (A) is provided as a reference. Arrows point to the location of a biopsy clip. Note the more homogeneous distribution of the fat susceptibility values and the brighter appearance of the metal object relative to fat after application of the chemical shift correction.

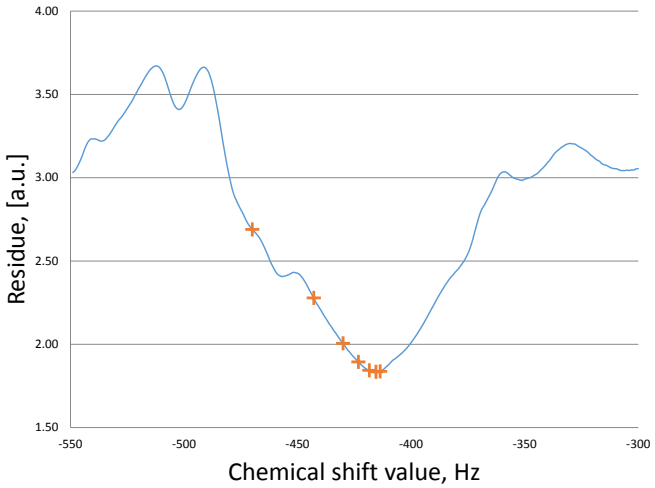

Figure 3.10: Model residual as a function of the chemical shift; the + symbols indicate the location of the successive iterations of the proposed algorithm for the data in Fig. 3.9. This demonstrates that the proposed method finds the global minimum of the combined fat, water and chemical shift minimization problem.

3.5 Discussion

In this chapter, a fully automated iterative algorithm for quantitative susceptibility mapping (QSM) within tissues with significant fat content has been presented. The algorithm assumes that the field inhomogeneity is caused by the susceptibility of two species water and fat and their chemical shifts. It utilizes the updated prior information about tissue structure and penalizes the discrepancy between modeled and measured signals. Simulations, phantom validation and in vivo results suggest that the proposed chemical shift correction effectively reduces streaking artifacts and preserves fine anatomical structures in the final QSM.

QSM involves solving an ill-posed inverse problem that is sensitive to error propagation, so it has a high accuracy requirement for the input field map. Taking the brain QSM as an example, the noise standard deviation on the estimated field map is on the order of $1/\mathrm{SNR}/(2\pi\mathrm{TE})$ = 0.1 Hz with SNR=50 assumed at TE=30ms. Although field map estimation may appear to be simple even in the presence of chemical shift, a straightforward application of T_2^*-IDEAL proves to be insufficient to reach the accuracy level required for the field map, leading to substantial streaking artifacts. One key revelation here is that error in the presumed chemical shift (0.1 ppm, translated to 6.4Hz at 1.5T or 12.7Hz at 3T) leads to a substantial error in the estimated field map as demonstrated by 3.4. It was shown in the experimental results that only the chemical shift resulting from an iterative data fitting procedure was able to reach the accuracy level of the field map required by QSM.

The uncertainty in the chemical shift has been reported in literature. Publi-

cations [35–37] demonstrate an increased interest in the multi-component modeling of the chemical shift. However, different fat components are generally assumed to be correlated with fixed relative amplitudes and spectral shifts, and ambiguity exists in how to assign the main components of the spectrum: the reported location of the central line (containing 60-85% of the overall fat signal) varies within a 0.2 ppm range [35–37]. To obtain an accurate measurement of the chemical shift, additional NMR spectroscopy may be required. Nevertheless, there is evidence that fat may cause bulk magnetic susceptibility effects [47], shifting spectral components, and thus rendering ineffective otherwise precise spectral models. Depending on the fat compartmentalization, its resonance frequencies might shift depending on orientation relative to the direction of magnetic field, as suggested in references [33,47,48]. Additionally, it is inconvenient or impossible to perform a spectroscopy for each individual subject or organ examined.

The uncertainty in chemical shift also causes errors in the water and fat fraction maps. However, it did not lead to substantial noticeable artifacts on the water and fat images. This robustness may be due to the fact that the off-resonance frequency is only used to demodulate the recorded MRI signal, which is followed by a well-posed least squares fitting problem to estimate ρ_0 and ρ_1 [31]. In contrast, QSM, which requires solving an ill-posed inverse problem, is much more sensitive to inaccuracies. Errors in a single voxel may propagate to its surroundings, causing streaking artifacts. Therefore, the calibration of chemical shift appeared to be a critical step for QSM.

The proposed algorithm is useful in clinical and research applications where the knowledge of field distribution is crucial. The ability to calculate precise

field distributions may be important for active shimming or MR-based thermography. Although only breast QSM is shown in this study, we expect the proposed algorithm will show similar improvements in other organs where chemical shift is present. Further improvements of the current implementation are possible. Although multiple fat species can be handled as formulated in Eq. 3.1, the current implementation requires a segmentation of water region and fat region, which is automatically obtained using T_2^*-IDEAL. When multiple types of fat are imaged within the same FOV, the automatic segmentation of different types of fat may be challenging, considering that the frequency difference between them are small. However, if prior information is available on the locations of different types of fat, then the water/fat separation problem can be solved independently in different regions. This allows extending the proposed method to the case of multiple fat types. This limitation did not appear to have undermined the quality of reconstructed phantom and in vivo susceptibility maps presented in this work. This may be due to the fact that only a single type of fat was present within the FOV (e.g., lard or fatty breast tissue). Additionally, the assumption of a fixed fat spectrum across the FOV is made by most existing water/fat separation methods. In the numerical simulations, a single peak model was used to fit the data generated by a multi-peak spectrum, with minimal effect on the estimated field map accuracy. It is noted that the updated chemical shift is different from the main peak. Thus, the proposed algorithm finds an effective frequency which results in the lowest fitting residual. Regarding the imaging parameters, carefully chosen TEs may improve the SNR of the water and fat maps [49], which is useful for the automatic segmentation. In our experiments, bandwidth was on the order of 500Hz per pixel, corresponding to a shift of less than one voxel at 3T. Switching to lower band-

width such as 16.25kHz would improve SNR, but at the expense of voxel shifts up to 4 voxels that would require further correction. Additionally, only a single R_2^* was assigned for each voxel, although water and fat may have different R_2^*. This limitation did not seem to have affected the reconstructed QSM images, which may be due to 1) most of the voxels contain a single species, and 2) R_2^*, which affects signal amplitude, has minimal effect on the field estimation step that mainly utilizes signal phase.

In conclusion, a joint estimation of fat content and magnetic susceptibility using a fully automated iterative chemical shift update is proposed. Numerical simulations, phantom and volunteer studies showed that the proposed iterative algorithm markedly reduced artificial signal variation on the QSM image and improved the accuracy of the estimated susceptibility in numerical simulation and phantom experiments.

CHAPTER 4

BONE QUANTITATIVE SUSCEPTIBILITY MAPPING USING A CHEMICAL SPECIES SPECIFIC R_2^* SIGNAL MODEL WITH ULTRASHORT AND CONVENTIONAL ECHO DATA

Purpose: To develop quantitative susceptibility mapping (QSM) of bone using an ultra-short echo time (UTE) gradient echo (GRE) sequence for signal acquisition and a bone-specific R2* to model fat/water MR signals for field mapping.

Methods: 3D radial UTE data (TEs $\geq 40\,\mu s$) was acquired on a 3T scanner and fitted with a bone-specific signal model to map the chemical species and susceptibility field. Experiments were performed ex vivo on a porcine hoof and in vivo on healthy human subjects (n=7). For water/fat separation, a bone-specific model assigning R_2^* decay mostly to water was compared with the standard models which assigned the same decay for both fat and water. In the ex vivo experiment, bone QSM was correlated with CT.

Results: Compared to standard models, the bone-specific R_2^* method significantly reduced errors in the fat fraction within the cortical bone in all tested datasets, leading to reduced artifacts in QSM. Good correlation was found between bone CT and QSM values in the porcine hoof ($R^2 = 0.77$). Bone QSM was successfully generated in all subjects.

Conclusion: QSM of bone is feasible using UTE with a conventional TE GRE acquisition and a bone-specific R_2^* signal model.

4.1 Introduction

Magnetic susceptibility is a fundamental tissue property that can be observed in MRI [50]. Densely calcified tissues such as bone have strong diamagnetic susceptibility [4,51–56]. Quantitative susceptibility mapping (QSM) [7,10, 57–59] can provide quantitative, reproducible images of magnetic susceptibility sources to assess the health and disease of many tissues [5,8,16,20,22,51,59–64], but its application in bone has been limited. Given the importance of measuring bone mineral density for assessing bone fracture risks in postmenopausal women and the elderly [65], QSM may become a useful diagnostic tool for non-invasive imaging of bone health without the use of ionizing radiation.

QSM of the bone has been challenging because it requires complete measurements of phase everywhere within the region of interest (ROI) and cortical bone typically has very low signal at conventional echo times in gradient echo (GRE) imaging. Although water is abundant in cortical bone (~15% by volume [66]), it mostly exists in the bound form, that is, connected to the crystalline mineral structures or the collagen matrix. As a result, bound bone water has an ultra-short apparent transverse relaxation time (T_2^* ~300 μs [67]), resulting in no meaningful phase for QSM reconstruction on conventional MRI. Due to these limitations, previous work in musculoskeletal applications of QSM was either focused on cartilage, or utilized piece-wise estimations of bone susceptibility [4, 68–73]. An additional problem arises from intermingling of fat and water protons in the bone marrow necessitating application of water/fat separation techniques for field mapping.

The purpose of this preliminary study was to investigate the feasibility of us-

ing QSM for measuring bone MRI signal and to highlight the inherent technical issues involved in this application. To that end, we measured bone MRI signal using an ultra-short echo time (UTE) pulse sequence with TE $\ll$ 1 ms [74,75] and investigated chemical shift and R_2^* components to properly model bone MRI signal in both UTE and conventional GRE.

4.2 Theory

Magnetic field estimation is an essential initial step for QSM. For QSM of anatomical regions where magnetic susceptibility is the predominant contributor to the proton phase accrual such as in the brain, the field can be estimated from the MRI signal phase. For QSM on regions with high fat content, such as in bone with marrow, a complex MRI signal model is needed for estimating the inhomogeneous field generated by susceptibility through robust separation of water and fat signals [31,32,35,36].

In a multi-echo GRE sequence, the temporal behavior of the signal originating from the voxel $\vec{r}$ that contains multiple species can be expressed in general form as:

$$s(\vec{r},t) = \sum_k \rho_k(\vec{r}) \sum_n \alpha_n^k e^{-i2\pi f_n^k t} e^{-R_{2n}^{*k} t} \cdot e^{-i2\pi f_s(\vec{r})t} \tag{4.1}$$

Here, ρ_k is the complex signal originating from the k^{th} chemical species within the voxel at time $t = 0$, α_n^k is the relative amplitude of the nth peak in the chemical spectrum of the k^{th} species, f_n^k and R_{2n}^{*k} are the corresponding chemical shift and R_2^* decay rate for the n^{th} spectral peak of the k^{th} species respectively, and $f_s(\vec{r})$ is a spatially varying field induced by susceptibility sources, or the sus-

ceptibility field. Extracting multiple parameters from the MRI signal is highly sensitive to noise propagation, and reducing the number of parameters in Eq. 4.1 is critical for robust estimation. We propose the following reduction in parameter numbers.

In many clinical applications, water and fat are the dominant species and 4.1 becomes

$$s(\vec{r},t) = \left(\rho_w(\vec{r})e^{-R^*_{2w}t} + \rho_f(\vec{r})\sum_n \alpha^f_n e^{-i2\pi f^f_n t}e^{-R^{*f}_{2n}t}\right)e^{-i2\pi f_s(\vec{r})t} \tag{4.2}$$

Here α^f_n is the relative amplitude of the n^{th} spectral peak of fat, ρ_f and ρ_w are fat and water complex amplitude at time $t = 0$, R^*_{2w} and R^{*f}_{2n} are water and the n^{th} spectral component of fat transverse decay rates.

Although there is some variation in R^*_2 decay rates among spectral peaks, an approximation is made here that it is constant. This simplifies Eq. 4.2:

$$s(\vec{r},t) = \left(\rho_w(\vec{r})e^{-R^*_{2w}t} + \rho_f(\vec{r})e^{-R^{*f}_2 t}\sum_n \alpha^f_n e^{-i2\pi f^f_n t}\right)e^{-i2\pi f_s(\vec{r})t} \tag{4.3}$$

In many applications, the difference in water and fat R^*_2 within a voxel $\vec{r}$ are commonly neglected [31,32]:

$$s(\vec{r},t) = \left(\rho_w(\vec{r}) + \rho_f(\vec{r})\sum_n \alpha^f_n e^{-i2\pi f^f_n t}\right)e^{-R^*_2 t}e^{-i2\pi f_s(\vec{r})t} \tag{4.4}$$

Unfortunately, in bone tissue, water is distributed through a porous mineral matrix, and fat in the marrow tends to aggregate, and we have $R^*_{2bone} \gg R^*_{2fat}$. Consequently, the use of 4.4 to fit the bone MRI signal may lead to very large errors in the estimation of fat fraction, susceptibility field, and QSM.

Therefore, we propose to avoid the R_2^* simplification in 4.4. The water signal is the main component acquired in cortical bone voxels. In our experiments (see below), the largest echo time is much shorter than the T_2^* of surrounding soft tissues, including marrow. Therefore, the bone water is the only species experiencing significant decay during acquisition. Accordingly, we further propose a bone-specific R_2^* model with the following reduction of parameters:

$$s(\vec{r},t) = \left(\rho_w(\vec{r})e^{-R_{2w}^* t} + \rho_f(\vec{r})\sum_n \alpha_n^f e^{-i2\pi f_n^f t}\right) e^{-i2\pi f_s(\vec{r})t} \tag{4.5}$$

4.3 Methods

4.3.1 Pulse sequence

A radial 3D GRE UTE sequence with $TE \geq 40\ \mu s$ was implemented on a clinical 3T scanner (GE Excite HD, Milwaukee, WI). The sequence used a nonselective hard pulse (rectangular pulse of 100 μs duration) to achieve volumetric excitation and two readouts per TR to accelerate acquisition (Fig. 4.1). On successive TRs, the echo times were shifted to achieve four unique echo times, two of which were considered ultra-short.

4.3.2 Porcine specimen experiment

A phantom was constructed from a porcine hoof specimen (length 16 cm, thickness 6.5 cm) embedded in 1% agarose gel (container height 20 cm, average diameter 11 cm) and, for comparison purposes, was imaged using an MR

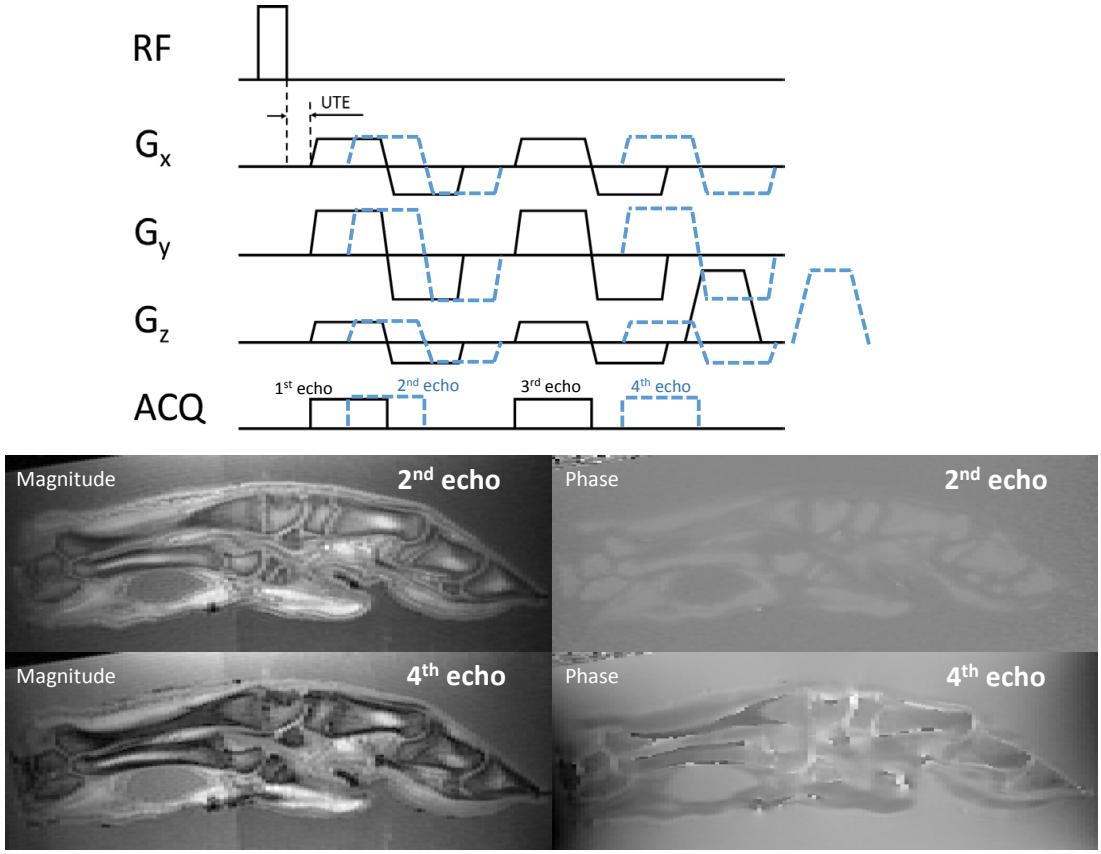

Figure 4.1: Top: Dual echo gradient echo acquisition for acquiring one ultra-short echo and one conventional echo image. Both echoes are shifted between successive TRs to acquire four unique echo time values. Echoes acquired in the same TR are shown using the same line type. The images below compare the magnitudes and phases of two of the acquired echoes. The phase of the first echo is set to zero during coil combination to eliminate phase offsets of different channels.

scanner (3T, GE Excite HD, Milwaukee, WI) and a clinical CT system (LightSpeed Xtra, GE Milwaukee, WI). MR imaging parameters included the following: TE=0.04, 0.24, 3.0, 4.0 ms, TR=12 ms, FA=15°, FOV=18 cm, 32000 radial projections per echo, voxel size 0.7×0.7×1.4 mm^3, BW = ±62.5 kHz, total acquisition time = 13 min. CT data was acquired using the following parameters: 120 kVp, 200mA, 0.625 mm slice thickness, 512×512 matrix, achieving nearly

isotropic resolution.

4.3.3 Volunteer MR imaging

After obtaining written informed consent, 7 healthy volunteers (6 male, 1 female age range 25 - 32 years, mean = 30) were scanned. All exams were performed under protocols approved by the Institutional Review Board and were HIPAA compliant. Images (11 distal femurs, 1 distal radius and 1 proximal tibia) were obtained on a 3T MRI system using an 8 channel transmit-receive knee coil and 8 channel transmit-receive wrist array. The 3D UTE GRE sequence was used with the following parameters: TE=0.04, 0.24, 3.0, 4.0 ms, TR=12 ms (echoes 1 and 3 and echoes 2 and 4 were acquired in successive TRs in interleaved manner in this experiment), FA=15°, FOV=18 cm, 32000 radial projections per echo, voxel size = 0.7×0.7×1.4 mm^3, total acquisition time for all echoes = 13 min.

4.3.4 Image processing and analysis

Each radial MR dataset was reconstructed using regridding [76], which interpolates the measured signal from radial spokes onto a Cartesian grid. In this work, NUFFT [77] with Kaiser-Bessel kernel and min-max interpolation was implemented. Because of the non-uniform sampling density of our radial trajectory, density compensation [78] was applied to the measured signal prior to re-gridding. Each data set was reconstructed on a coil-by-coil and echo-by echo basis.

For each coil, the phase of the 1st echo was subtracted from the phase of each

of the following echoes in order . This allowed a complex coil combination by simply summing the complex data across all coils for each echo. Finally, the phase of this summed signal was used as the phase for the corresponding echo.

Water, fat and inhomogeneity components were then obtained using IDEAL-based techniques [31, 32, 36]. For this iterative method, it is important to use an initial guess for the inhomogeneity field that is reasonably close to the true solution in order to avoid convergence to a local minimum. A preliminary field map estimation was carried out using SPURS [79] assuming a single chemical shift peak with value f=-3.5ppm$\cdot\gamma B_0$ Hz. An initial estimation of the distribution of R_2^* values was produced by mono-exponential fitting [80]. The complex data was then fitted to Eqs. 4.4 and 4.5 assuming different models for the fat chemical spectrum: single peak model (Δf = -3.46 ppm) and multi-peak model ($\Delta \vec{f}$ ={-3.82, -3.46, -2.74, -1.86, -0.5, 0.5} ppm) [35]. From the resulting inhomogeneity field f_s, a susceptibility map was obtained using the morphology enabled dipole inversion (MEDI) pipeline [8]. Projection onto Dipole Fields (PDF) [44] was utilized for background field removal. All susceptibility values reported in this work were referenced to adjacent homogenious muscle tissue)

CT images of the porcine hoof were resampled and registered to the reconstructed susceptibility map using the FLIRT algorithm in the FSL toolbox [81]. ROI analysis was performed on co-registered volumes to correlate the CT signal (in Hounsfield units, HU) with the MR signal (calculated susceptibility values). For this, 58 in-slice regions of interest were manually drawn in flexor tendon, and trabecular and cortical areas of metacarpal and phalanx bones. QSM and CT volumetric averages for the ROIs were recorded and used for correlation analysis.

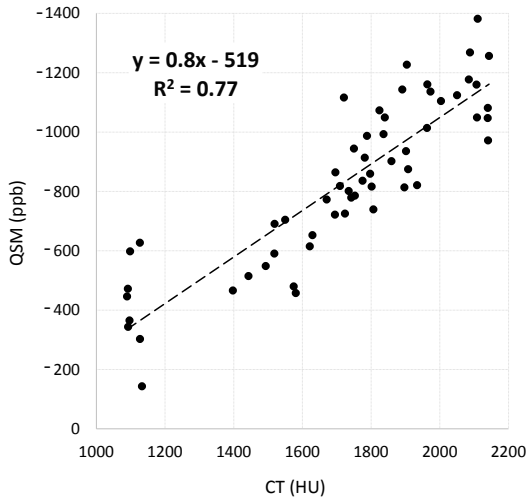

Figure 4.2: Regression of QSM vs. CT for the ROI values in the porcine hoof phantom. Good correlation was observed between estimated susceptibility and Hounsfield units.

4.4 Results

4.4.1 Porcine phantom results

A susceptibility map of the specimen was successfully reconstructed. Comparison of CT and QSM images is shown in Fig. 4.3 along with results of the ROI analysis (Fig. 4.2). It should be noted that the good correspondence between diamagnetic regions in QSM and regions of high Hounsfield values in CT images is supported by a strong linear correlation (correlation coefficient R^2 = 0.77).

Figure 4.3: Comparison of CT images (A,C) with correspondent planes of reconstructed QSM (B,D) and ultra-short (40 μs) echo magnitude (E,F). Note the homogeneous diamagnetic appearance of cortical bones and overall fair correspondence between regions of high HU and low susceptibility values.

4.4.2 Volunteer results

QSM reconstruction using the proposed method with water-specific R_2^* and multi-peak fat spectrum modelling was successful in all volunteers (see example in Fig. 4.4). Fig. 4.5 shows a comparison of the field maps estimated with different techniques and the corresponding calculated susceptibility distributions. Systematic overestimations of the fat fraction within the bone and tendon (up to 80% above the negligible lipid content expected in healthy bone) areas were observed in maps calculated using conventional estimators. This led to errors in the field and, subsequently, the susceptibility map with significant errors in bone and tendon susceptibility values . This was most notable when assum-

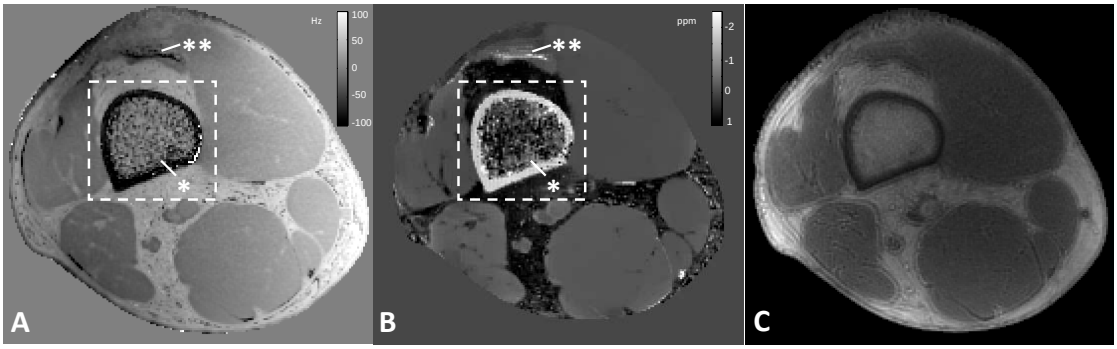

Figure 4.4: Results of field map reconstruction (A), susceptibility (B), and magnitude of the ultra-short (40 μs) echo (C) using femur data from a healthy volunteer. Note the homogeneous diamagnetic appearance of the cortical bone and the visible trabeculation in both the field map and QSM (*), and strong diamagnetism of the quadriceps tendon (**). Please refer to Fig. 4.5 for further details on the selected area (dashed line).

ing either a single fat peak or a common $R2^*$ between fat and water. In this case, the cortical bone region of the femur erroneously appeared to be paramagnetic (Fig. 4.5). It should also be noted that the proposed technique yielded the best visualization of trabecular bone (Fig. 4.4, 4.5).

Fig. 4.6 shows a minimum intensity projection of the reconstructed QSM of the knee joint in one healthy subject. Homogeneous diamagnetic appearance of thick cortical areas of the femoral (top yellow arrow) and tibial (bottom yellow arrow) shafts are visible. Throughout the entire FOV, trabeculation is well depicted by QSM, with a clear appearance of the epiphyseal plate (red arrow) and the area of transition from diaphyseal to metaphyseal bone (blue arrow). Observed nearly homogeneous appearance of the susceptibility throughout the bone is expected, given the likely absence of red marrow in the distal femur in this 28 y/o male volunteer .

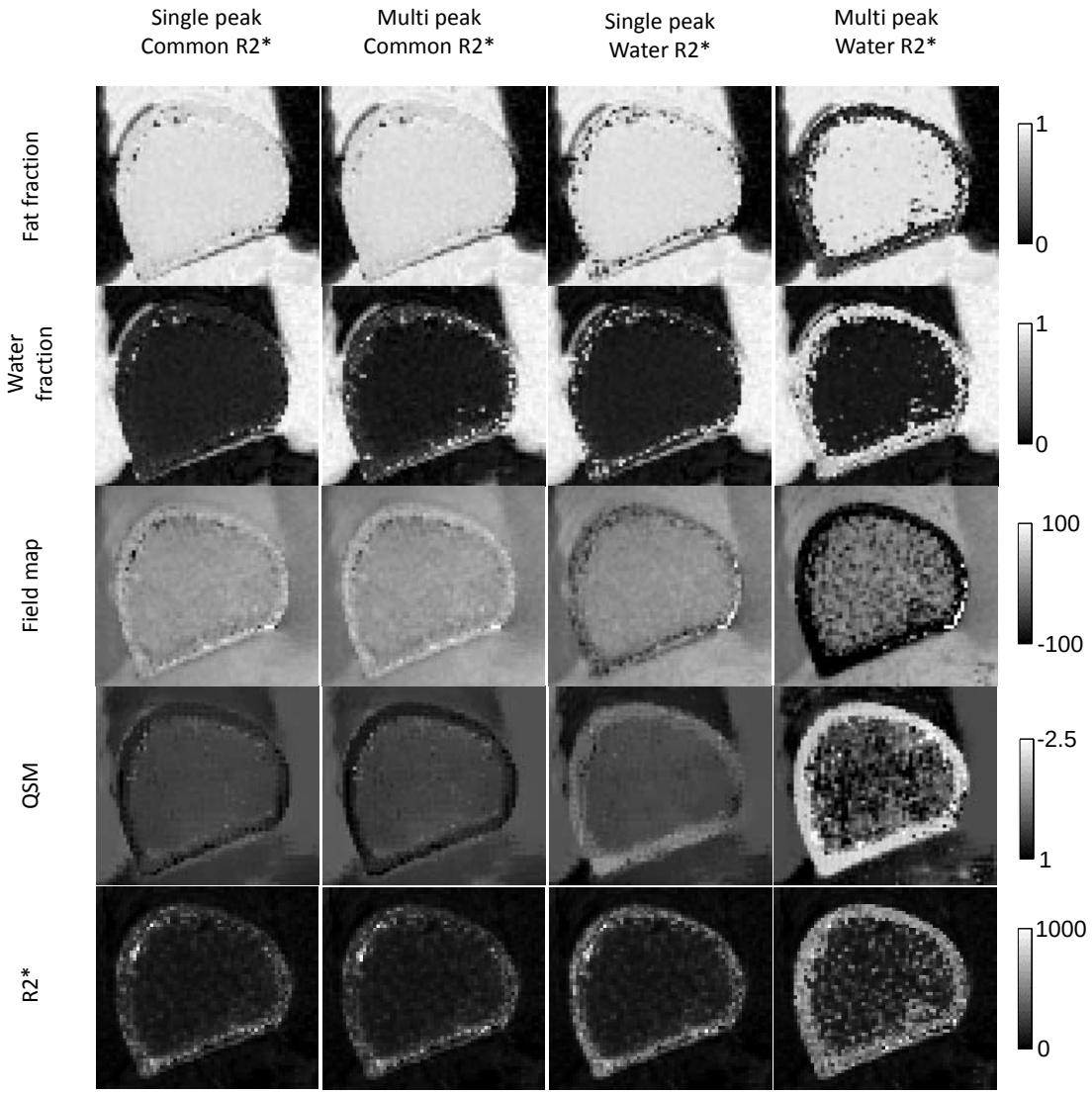

Figure 4.5: Comparison of fat and water fraction maps, field maps, QSM and estimated tissue signal decay rates for different signal models, including single- and multi-peak fat spectrum and common and water-only R_2^* modeling

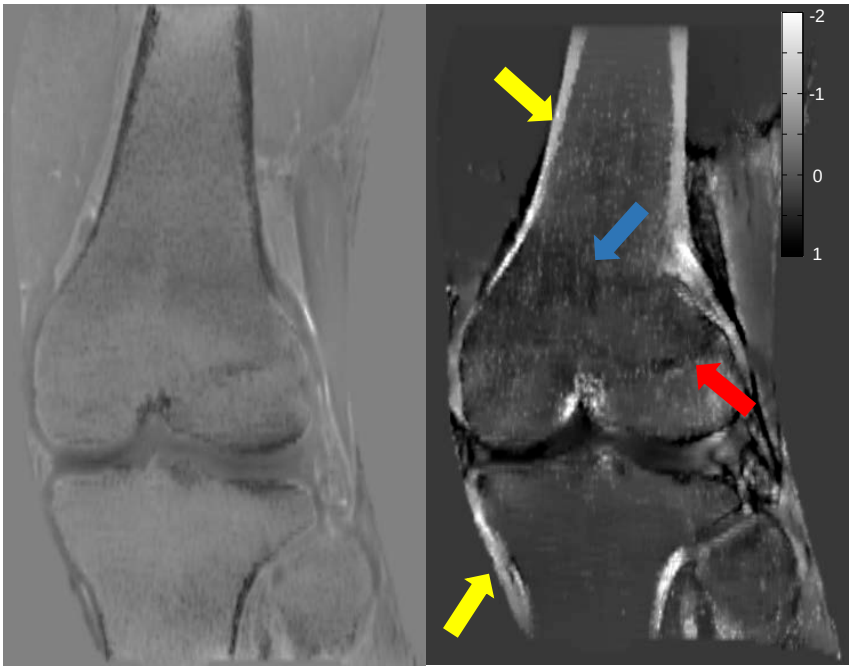

Figure 4.6: Local field (left) and thin slab maximum intensity projection of knee joint QSM (right), reconstructed using the proposed technique. A minimum intensity projection of the reconstructed QSM of the knee joint is shown in one healthy subject. Note the delineation of cortical areas of the femur and tibia (yellow arrows), the depiction of trabeculation, the epiphyseal line (red arrow), and the area of transition from diaphyseal to metaphyseal bone (blue arrow) in the femur, and reduced contrast between the bone and surrounding joint tissue.

The results of the volunteer scans (Table 1) reveal good intra-and inter-subject agreement of susceptibility values for cortical bone (inter-subject average χ_{bone}=-1.4±0.2 ppm).

Subject	Sex	Bone	Estimated Susceptibility
1	M	Femur (left)	-1.29 ± 0.27
		Femur (right)	-1.21 ± 0.33
2	M	Femur (left)	-1.19 ± 0.38
		Femur (right)	-1.38 ± 0.46
3	M	Femur (left)	-1.23 ± 0.41
		Femur (right)	-1.16 ± 0.19
4	M	Femur (left)	-1.49 ± 0.49
		Femur (right)	-1.4 ± 0.47
5	M	Femur (left)	-1.41 ± 0.4
6	F	Femur (left)	-1.8 ± 0.87
		Tibia (left)	-1.76 ± 0.64
7	M	Femur (left)	-1.39 ± 0.31
		Radius (right)	-1.44 ± 0.63

Table 4.1: Measured susceptibility values of cortical bone in the distal femur, proximal tibia, and distal radius of 7 healthy volunteers

4.5 Discussion

Our data demonstrate the feasibility of mapping bone magnetic susceptibility including cortical bone, trabecular bone, and marrow. This method utilizes a radial UTE gradient echo (GRE) sequence to acquire the rapidly decaying signal of bone water, and a novel bone-specific-R_2^* in signal modeling to achieve accurate water/fat separation. Results in an ex vivo porcine hoof show excellent correlation with CT. By comparing QSM reconstructions using the current standard signal model with a common R_2^* for both fat and water components, the bone-specific-R_2^* approach reduces fat fraction estimation errors within cortical bone and generates susceptibility maps in which cortical bone is correctly identified as diamagnetic [55,56]. As the highly concentrated calcification is the dominant susceptibility source, QSM allows noninvasive quantitative mapping of bone mineralization without the need for radiation.

Field estimation from UTE and conventional echo GRE data using the classic T_2^*-IDEAL is non-trivial, and is prone to noise propagation and bias. The robust extraction of biophysical parameters from GRE data require proper signal modeling with a minimal number of parameters. Standard GRE signal models assign identical R_2^* to both water and fat species [31,32] fail to correctly estimate the field, consequently generating bone QSM with grossly erroneous values (such as paramagnetic bone), because rapid signal decay of bone is misinterpreted as dephasing due to the high fat fraction. Over the echo times acquired in this study, there is negligible R_2^* decay of the fat signal but rapid R_2^* decay of signal in cortical bone due to collagen bound water [82]. This led us to the bone-specific R_2^* model that accurately reflects the underlying tissue physics, attributing signal decay exclusively to the water component. Both the porcine hoof and human volunteer data show that this bone-specific R_2^* model when combined with iterative least squares fitting provides reliable estimation of chemical species distribution as well as a biologically plausible field map. Additionally, the application of the multi-peak fat spectrum model further improves the quality of the water/fat separation and, consequently, the susceptibility map.

Previous studies show bone magnetic susceptibility can be estimated by a highly regularized piece-wise inversion of the local magnetic field [4], which may be problematic when there is local variation in tissue susceptibility. A masked iterative calculation of susceptibility can also be used to estimate distribution of strong magnetic sources in tissue [52], but the iteration tends to enforce both uniformity and underestimation of high susceptibility structures. Above all, these attempts do not properly account for the underlying fat water biophysics in the MRI signal generation, nor do they acquire signal within bone using UTE, as illustrated in this work. For trabecular bones with densities much

lower than those of cortical bones, QSM may be straightforwardly applied using conventional echo times [83].

Bone mineral density (BMD) assessment is central to the diagnosis of osteoporosis [84, 85]. Currently, BMD is measured using dual energy X-ray absorptiometry (DXA), which may be confounded by factors including degenerative changes, small bone size, and overlaying anatomic structures [65]. Quantitative CT (QCT) has been proposed to overcome these limitations of DXA, but it requires a much higher X-ray dose [65]. A number of non-invasive non-ionizing radiation based methods for characterizing bone tissue are also available: ultrasound can be used to characterize bone and assess osteoporosis but may only provide correlative not absolute bone density quantification [86]. MRI-based techniques, including ZTE and UTE, can be used to detect water bound to the organic matrix of the bone, but bone-bound water quantification requires separation of bound and free water signal components of different relaxation rates and signal scaling [82, 87–91]. Conventional MRI may be used to assess bone quality but not mineral density [65].

The MRI-based bone QSM presented here suggest the possibility of BMD assessment without X-ray radiation. Therefore, our results warrant future research in comparing bone QSM with DXA on patients including those suffering from osteoporosis to establish an accurate non-X-ray BMD assessment for predicting fracture risk and guiding therapy. A comprehensive comparison of QSM as a biomarker with other non-ionizing radiation based measures falls outside of the scope of this preliminary study, which has been focused on establishing feasibility of using QSM. Additional investigation is required to assess the clinical utility of bone QSM.

The main limitation of including UTE in QSM is the relatively long acquisition time, about 13 minutes in this study. Scan time may be reduced substantially using data acquisition acceleration strategies in Bayesian MRI [50, 92–96]. Another potential limitation stems from the assumption that water is the only species experiencing significant decay by the time the last echo is acquired. Although this is correct in many practical situations when bone matrix bound water is present, this assumption may break down under conditions of strong field inhomogeneity, such as imaging near the abdominal cavity. These field variations can lead to strong spin dephasing and, as a result, rapid R_2^* decay in soft tissue regions. In this situation, high order shimming might be required. An additional limiting factor not taken in the account in the present work is the image blurring inherent in radial imaging induced by field inhomogeneity and chemical shift [97]. If Cartesian imaging had been used, the bandwidth chosen in this work would correspond to a shift for fat slightly below one pixel. The image blurring here is expected to affect final QSM results, and the application of off-resonance correction methods appropriate for non-Cartesian acquisition [97,98] may be required. Finally, as has previously been reported, QSM is prone to underestimation of strong susceptibility sources [99], and further adjustments of the imaging protocol such as matrix size and resolution, may be necessary to minimize error.

A comparison of the results obtained with the proposed technique with those previously reported in the literature [54–56, 100] demonstrates possible underestimation of bone magnetic susceptibility. For example, in [55, 56] the authors report bone susceptibility χ_{bone} ≈-2.4 ppm obtained in an in vitro experiment. An in vivo estimation performed in [4, 100] yielded a fairly wide range of values χ_{bone} ≈-1.8~-2.3 ppm depending on the reconstruction method. This

underestimation is most notably observed around the joints (Fig. 6). The exact nature of this underestimation may be related to partial volume effects (volume fraction of water in the cortical bone, for example) and abovementioned limitations of the technique, although this issue requires further investigation.

A future direction of this work can be an investigation of the anisotropic properties of bone, tendon, and cartilage susceptibilities. Although strong magnetic anisotropy in bone and cartilage has been previously reported [54,72,73], it has not been accounted for in the signal model in this preliminary study. The use of scalar susceptibility model even in the magnetically anisotropic cartilage may contribute to errors in the estimated susceptibility of nearby tissue regions.

In conclusion, quantitative magnetic susceptibility maps across the entire bone cross-section are feasible using a combination of UTE, a conventional TE gradient echo acquisition, and a bone-specific R_2^* signal model.

CHAPTER 5

HIGH RESOLUTION QSM FOR FUNCTIONAL AND STRUCTURAL DEPICTION OF SUBTHALAMIC NUCLEI IN DBS PRE-SURGICAL MAPPING

Objective: Faithful depiction of the subthalamic nucleus (STN) is critical for planning deep brain stimulation (DBS) surgery in patients with Parkinsons disease (PD). Quantitative susceptibility mapping (QSM) has shown to be superior to traditional T2 weighted spin echo imaging (T2w). The aim of the study was to describe sub-millimeter QSM for preoperative imaging of the STN in planning of DBS.

Methods: 7 healthy volunteers were included in this study. T2w and QSM were obtained for all healthy volunteers, and images of different resolutions were reconstructed. Image quality and visibility of STN anatomical features were analyzed by a radiologist using a 5 point scale, and contrast properties of the STN and surrounding tissue were calculated. Additionally, data from 10 retrospectively and randomly selected PD patients who underwent 3T MRI for DBS were analyzed for STN size and susceptibility gradient measurements.

Results: Higher contrast-to-noise (CNR) values were observed in both high and low resolution QSM images. Inter-resolution comparison demonstrated improvement in CNR for QSM, but not for T2w images. QSM provided higher inter-quadrant contrast ratios (CR) within the STN, and depicted a gradient in the distribution of susceptibility sources not visible in T2w images.

Conclusions: For 3T MRI, sub-millimeter QSM provides accurate delineation of the functional and anatomical STN features for DBS targeting.

5.1 Introduction

The subthalamic nucleus (STN) is a deep gray matter structure, located in the midbrain and known to be involved in regulation of cognitive and motor functions [101, 102]. Therefore, it has been a primary target in deep brain stimulation (DBS) to improve parkinsonian symptoms [103–105]. Success of DBS is critically dependent on accurate placement of the stimulation electrodes [106]. However, precise targeting of the STN is a challenging task due to its small size, oblique orientation, and variations in anatomical location [107–110]. The STN is rich with iron that not only serves as a co-factor to generate glutamate for neurotransmission [111, 112], but also provides tissue contrast in MRI [113]. Consequently, spin echo T2-weighted (T2w) sequence has traditionally been used for identification of the STN in pre-surgical DBS planning [107, 114–116].

Recently, gradient echo (GRE) sequences have been found to provide more sensitive contrast than T2w sequences for depicting the STN [108]. The GRE magnitude sensitizes iron with the T2* hypointensity and the GRE phase is proportional to the magnetic field generated by tissue iron. But, both magnitude and phase signal at one location are affected by iron distribution in the surrounding tissue [50]. These non-local blooming artifacts are removed in quantitative susceptibility mapping (QSM) [10], a post-processing technique employing deconvolution of gradient echo phase data for faithful depiction of tissue iron distribution [57, 117]. QSM is regarded as the most promising technique for functional and stereotactic imaging of the STN [63, 118–121].

A detailed QSM data acquisition protocol has yet to be described for the DBS community. Here, we present a high resolution QSM protocol for sub-

millimeter imaging of deep gray matter structures that would improve identification and demarcation of STN sub-regions for DBS targeting.

5.2 Methods

Major parameters targeted in the protocol design include: sub-millimeter acquired voxel size, whole brain coverage, and clinically acceptable scan time (acquisition time less than 15 minutes). Since high resolution MR data might suffer from noise, additional tests were carried out to test the performance of QSM with millimeter-scale voxel sizes.

Imaging protocol

A 3T MR system (General Electric Healthcare, Milwaukee, USA) with an 8-channel head coil was used to acquire all the MR images. Sagittal 3D T2w (CUBE) and axial 3D GRE imaging were performed. Detailed parameters are summarized in Table 5.1. Both GRE and CUBE sequences were used to acquire data from healthy volunteers. Only GRE sequences were used to acquire data from PD patients.

Population characteristics

Seven healthy volunteers (7 men, age range 25-46 years, mean age of 31 years) were included in this study. Additionally, data from 10 randomly chosen PD patients (5 men, 5 women, age range 51-67 years, mean age of 58 years) who received MRIs for pre-surgical DBS planning from May 2016 to August 2016 were retrospectively analyzed. Indications for STN-DBS surgery included refractory motor fluctuations, medically refractory tremors, and drug-induced

Parameter	3D T2w	3D GRE
Imaging Plane	Sagittal	Axial
TR (ms)	3000	44.1
TE (ms)	92.3	$TE_1 = 3.8, \Delta TE = 4.06, \#TE = 10$
ETL	100	-
Bandwidth (kHz)	±62.5	±62.5
NEX	1	0.75
Acceleration factor	Slice=2	ASSET=2
FOV (cm)	25.6	25.6
Phase FOV	1	0.8
Acquisition matrix	$320 \times 320 \times 220$	$320 \times 320 \times 180$
Voxel (mm^3) acquired	$0.8 \times 0.8 \times 0.8$	$0.8 \times 0.8 \times (0.8 - 1.0)$
Voxel (mm^3) reconstructed	$0.5 \times 0.4 \times 0.5$	$0.5 \times 0.4 \times 0.5$
Scan time	13 min	13 min

Table 5.1: Imaging parameters.

dyskinesias. This study was approved by local IRB and the prospective subjects gave written consent.

Image analysis

QSM was reconstructed from the acquired high resolution GRE data at 0.5 mm isotropic resolution. Then, additional datasets for each contrast were synthesized with thicker axial slices to simulate low resolution acquisition by cropping in k-space along the kz direction. The final axial slice thickness of this low resolution data was set to 2 mm for QSM reconstruction. All resulting images (original and down-sampled) were then co-registered using FSL toolbox 22 to high-resolution T2*w images for further analyses.

Qualitative evaluation

A radiologist with 11 years of experience evaluated the appearance of the STN on T2w and QSM images from healthy volunteers and visually graded the

overall image quality on a 5-point scale based on the demarcation of the STN margins and definition of the intensity gradient due to changes in iron concentration: grade 4, all STN borders are clearly defined, and the gradient along the STN is visible; grade 3, all STN borders are clearly defined, but the gradient is not visible; grade 2, one or more border(s) are poorly defined, gradient is clearly visible; grade 1, one or more border(s) are poorly defined, gradient is not visible; grade 0, STN is not visible in the image.

Quantitative analysis

STNs were identified by their signal intensities (hypointense on T2w images and hyperintense on QSM) and locations relative to the anterior commissure (AC) posterior commissure (PC) line. Using a multimodal approach on the original high-resolution images, STNs were segmented manually in ITK-SNAP [122] on two consecutive axial slices located approximately 3.2 mm below the AC-PC line. This segmentation (approximately 0.25 cm^2 per STN on each slice) was further subdivided into four quadrants anterolateral (AL), anteromedial (AM), posterolateral (PL) and posteromedial (PM) based on main axes of the STN octagon in the axial plane (Fig. 5.1). To create ROIs containing adjacent white matter, a 1.5 mm thick band immediately surrounding the STN was drawn. To characterize visibility of each STN quadrant on QSM and T2w images, their CNRs with respect to immediately adjacent white matter (WM) were calculated for each slice resolution according to the following definition: $CNR_{WM} = \frac{|I_j - I_{wm}|}{\sigma_{wm}}$. Here I_j is the average intensity of one of the four STN quadrants, I_{wm} is average WM intensity and σ_{wm} is the standard deviation of intensity within the closest white matter sector. To assess the sensitivity of each sequence to the heterogeneous distribution of iron within the STN, contrast ratios be-

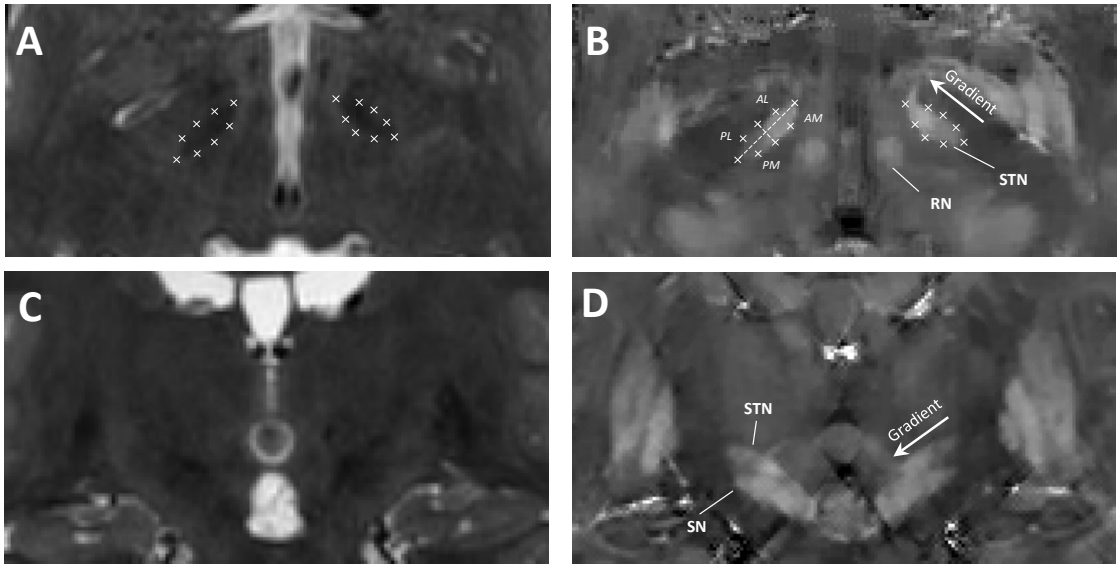

Figure 5.1: Axial and coronal views of the STN in T2w (A,C) and QSM (B,D) images from a healthy 25-year-old man showing the subthalamic nucleus (STN), substantia nigra (SN) and red nucleus (RN). Border points indicated by (x) were used to create bilateral masks of the nuclei (A) and to define the four STN quadrants: anterolateral (AL), anteromedial (AM), posterolateral (PL) and posteromedial (PM) (A). STN susceptibility gradient (shown with arrows) is clearly visible in the QSM images.

tween adjacent quadrants were estimated. The contrast ratio between regions i and j was defined as $CR_{ij} = \frac{I_i - I_j}{I_j}$.

Statistical analysis

Statistical analysis was performed using MATLAB routines. The data was reported as mean±SD. Comparisons of CNR values for each resolution were performed using the Wilcoxon signed rank test. For visualization scores, the Wilcoxon rank sum test was employed to test the difference between imaging methods for both resolutions.

5.3 Results

5.3.1 Healthy subjects study

Qualitative results

The STN was successfully imaged in all 7 volunteers. The average visualization scores for QSM and T2w images in high/low resolutions were, 3.86/2.0 and 1.886/1.0, respectively. The difference between scores for high resolution QSM and T2w images was significant ($p < 0.005$), while no significance was observed in the low resolution image sets. Switching to high resolution led to a significant increase in the radiologists assessment of the QSM images ($p < 0.005$), but not the T2w images. According to the scores, an intensity gradient was observed in 6 out of 7 high resolution QSM cases and 1 out of 7 low resolution cases. The gradient was not visible in any T2w images.

Quantitative results

The results of the CNR evaluation are summarized in Table 5.4. For 0.5 mm slice thickness, the CNRs of all STN quadrants on axial QSM images were higher than those of STN quadrants on axial T2w images ($p < 0.05$). The CNR in QSM was increased compared to T2w by an average factor of 1.94±0.42. For the 2 mm slice resolution, a statistically significant increase in the CNR of QSM relative to that of T2w was observed only in the lateral quadrants in both left and right STN. When comparing low and high resolutions, an increase in voxel size negatively affects the CNR in QSM ($p < 0.05$) in all quadrants. In T2w images, statistical significance was achieved only for anterolateral quadrants of the right STN. A representative comparison of the two different resolutions is shown in

Fig 5.2.

	Image	QSM		T2w	
Quadrant	**Slice thickness**	**0.5 mm**	**2 mm**	**0.5 mm**	**2 mm**
Anterolateral	Right STN	4.5 ± 1.7	4.0 ± 1.3*	2.2 ± 0.8	1.7 ± 0.6*
	Left STN	4.6 ± 1.4	4.0 ± 1.1*	2.3 ± 1.1	1.8 ± 0.9*
Anteromedial	Right STN	4.9 ± 0.8	2.7 ± 0.5*	3.4 ± 1.3	3.3 ± 1.2
	Left STN	5.0 ± 0.8	3.2 ± 0.3*	3.6 ± 2.0	3.6 ± 1.7
Posterolateral	Right STN	5.1 ± 1.8	3.9 ± 1.0*	2.3 ± 0.4	2.2 ± 0.4
	Left STN	4.9 ± 1.4	4.1 ± 1.2*	1.8 ± 0.3	1.7 ± 0.3
Posteromedial	Right STN	3.7 ± 0.6	2.6 ± 0.7*	1.9 ± 1.1	1.9 ± 0.6
	Left STN	4.1 ± 1.7	3.4 ± 1.8*	2.3 ± 0.8	2.2 ± 1.2

Table 5.2: Characterization of the STN quadrants contrast-to-noise ratios (CNR) relative to adjacent tissue. (*) indicates statistically significant difference ($p<0.05$) between resolutions.

For both resolutions, QSM demonstrated a higher contrast ratio between the anterior and posterior quadrants than T2w for all considered pairs of STN quadrants (with the exception of right AL-AM) (Table 5.4). Figure 5.3 shows a comparison of intensity profiles extracted from representative T2w and QSM images of one healthy volunteer along the axis connecting medial-inferior and posterior-lateral poles of the STN. Contrast between the anterior and posterior regions of the STN, and a gradual decrease in the concentration of susceptibility sources are more obvious in the profile for the susceptibility map than in T2w data (Fig. 5.3). STN sizes along its three main axes (mediodorsal-lateroventral, dorsolateral-ventromedial and rostro-caudal) were (3.2±0.3)×(5.3±0.3)×(11.8±0.9) mm^3 for the left and (3.1±0.2)×(5.3±0.4)×(11.0±0.9) mm^3 for the right STN. The STN susceptibility gradient over all subjects was -0.022±0.004 ppm/mm.

	Image	QSM		T2w	
	Slice thickness	**0.5 mm**	**2 mm**	**0.5 mm**	**2 mm**
PL to PM	Right STN	−0.7 ± 0.6	−0.7 ± 0.7	0.0 ± 0.1	0.0 ± 0.1
	Left STN	−1.0 ± 0.8	−0.8 ± 0.6	0.0 ± 0.1	0.0 ± 0.1
PL to AL	Right STN	−0.8 ± 0.3	−0.8 ± 0.3	0.2 ± 0.1	0.2 ± 0.1
	Left STN	−0.9 ± 0.2	−0.8 ± 0.3	0.2 ± 0.1	0.2 ± 0.1
AL to AM	Right STN	−0.2 ± 0.1	−0.2 ± 0.2	−0.2 ± 0.1	−0.1 ± 0.1
	Left STN	−0.2 ± 0.04	−0.2 ± 0.1	−0.02 ± 0.1	−0.1 ± 0.1
PM to AM	Right STN	−0.7 ± 0.2	−0.7 ± 0.2	0.1 ± 0.1	0.0 ± 0.03
	Left STN	−0.6 ± 0.2	−0.6 ± 0.2	0.1 ± 0.1	0.1 ± 0.1

Table 5.3: STN inter-quadrant contrast ratios

5.3.2 Patient study

QSM was successfully reconstructed in all 10 patient cases. Figure 5.4 shows QSM of the STN in the axial and coronal planes. In all cases, high contrast between STN and white matter, and the ability to distinguish it from the SN were achieved. The measured dimensions were (3.2±0.2)×(5.6±0.6)×(12.5±1.7) mm^3 for the left and (3.1±0.2)×(5.5±0.5)×(11.8±1.8) mm^3 for the right nucleus. The average QSM STN gradients were -0.026±0.009 ppm/mm and -0.029±0.008 ppm/mm for the left and right nuclei, respectively.

5.4 Discussion

The results of the current study suggest that contrast in QSM is superior to that of T2w for delineation of the STN with respect to surrounding white matter. Sub-millimeter voxel size QSM faithfully depicts high iron content within the deep gray matter nuclei, allowing for confident localization of borders and observation of iron content heterogeneity linked to functional subdivisions of

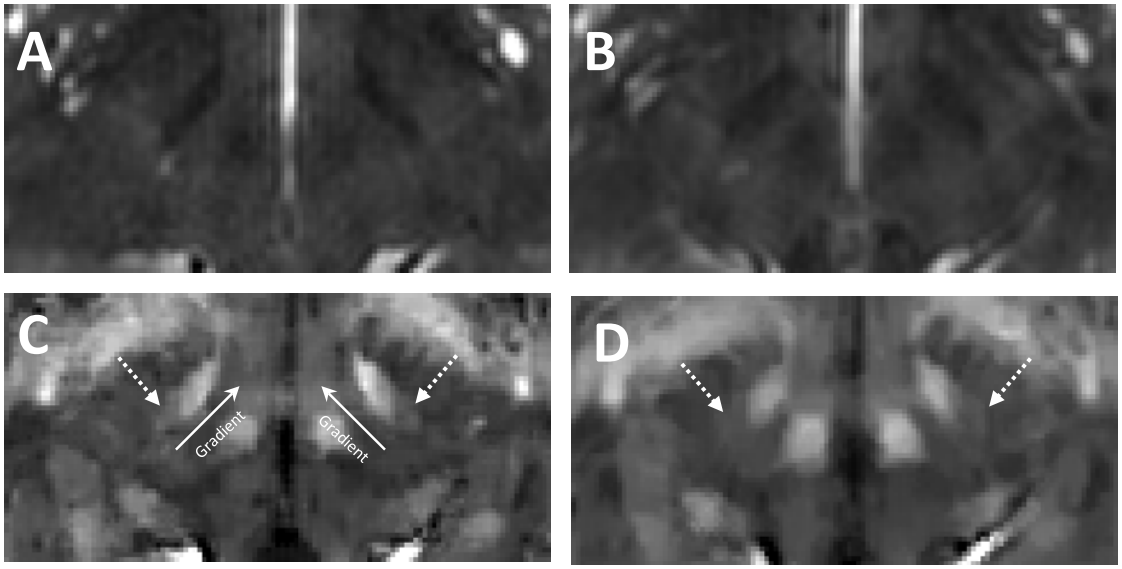

Figure 5.2: Effects of slice thickness on STN-vs-tissue contrast in T2w and QSM images in a healthy 33 year-old man. Left column T2w (A) and QSM (C) images with slice thickness of 0.5 mm; (B) and (D) T2w and QSM images, respectively, with slice thickness of 2 mm. Visibility of STN in T2w is relatively insensitive to slice thickness, as indicated by CNR measurements and the T2w image scores given by the radiologist. However, low resolution results in susceptibility underestimation in QSM, led to significantly reduced contrast in the posterolateral quadrant (dashed arrows). Unlike T2w, QSM demonstrates a clearly visible gradient towards the caudal STN pole (-0.024 ppm/mm) in both hemispheres.

the STN. High resolution QSM may be used for precise neurosurgical targeting in planning DBS, such as STN and globus pallidus internus (GPi) DBS for medically-complicated Parkinsons disease and GPi DBS for dystonia.

Over the last decade, direct visualization of the STN for preoperative planning has been established using MRI to map anatomical details [123–125]. High image quality is imperative to ensure efficacy of this patient-specific approach; given the variability between patients and complexity of the region, it is of great

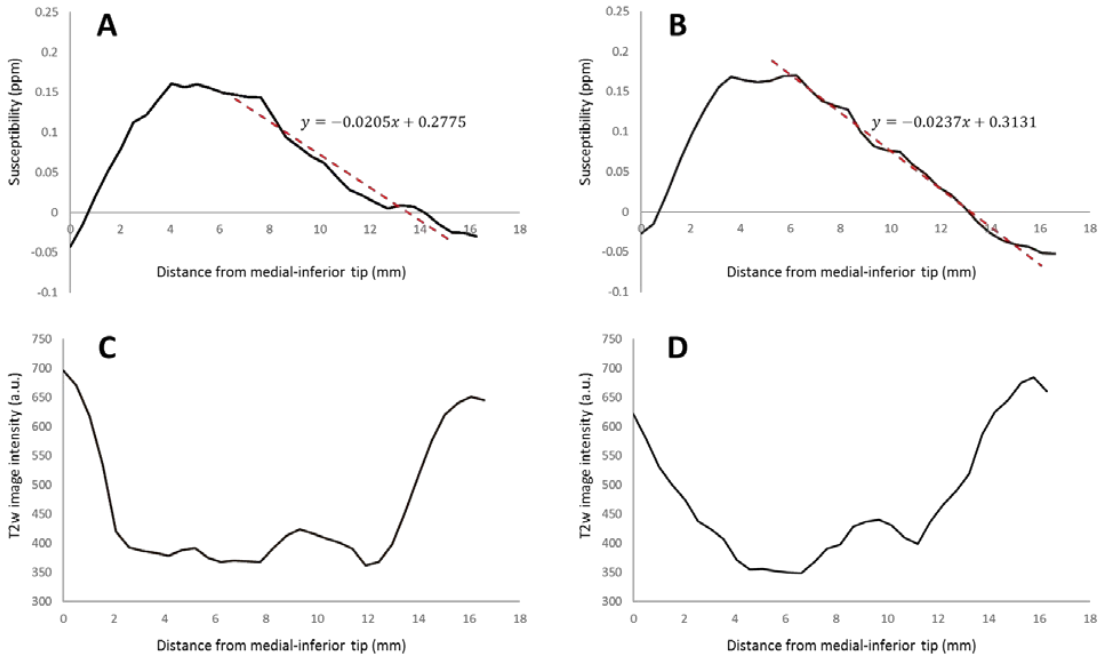

Figure 5.3: Comparison of intensity profiles extracted from sub-millimeter resolution QSM (A, B) and T2w (C, D) images of STN along the rostro-caudal axis. (A, C) left STN; (B, D) right STN. QSM consistently indicates a linear decrease in iron concentration (red dashed line), with an average susceptibility gradient of -0.022 ppm/mm.

importance to have sub-millimeter resolution and high-contrast images that provide visibility of all parts of the STN. Traditional T2w MRI has been used in STN targeting for DBS. High iron content within the subthalamic nuclei shortens the transverse relaxation time, making the STN appear hypointense in these images. Recently, inconsistencies between the STN borders estimated on T2w images, histology, and intraoperative microelectrode recordings (MERs) have been reported in multiple studies [107, 126–130]. One of the sources for these inconsistences is thought to be the inhomogeneous distribution of iron within the STN [107, 120], with the lowest iron concentration typically observed in the

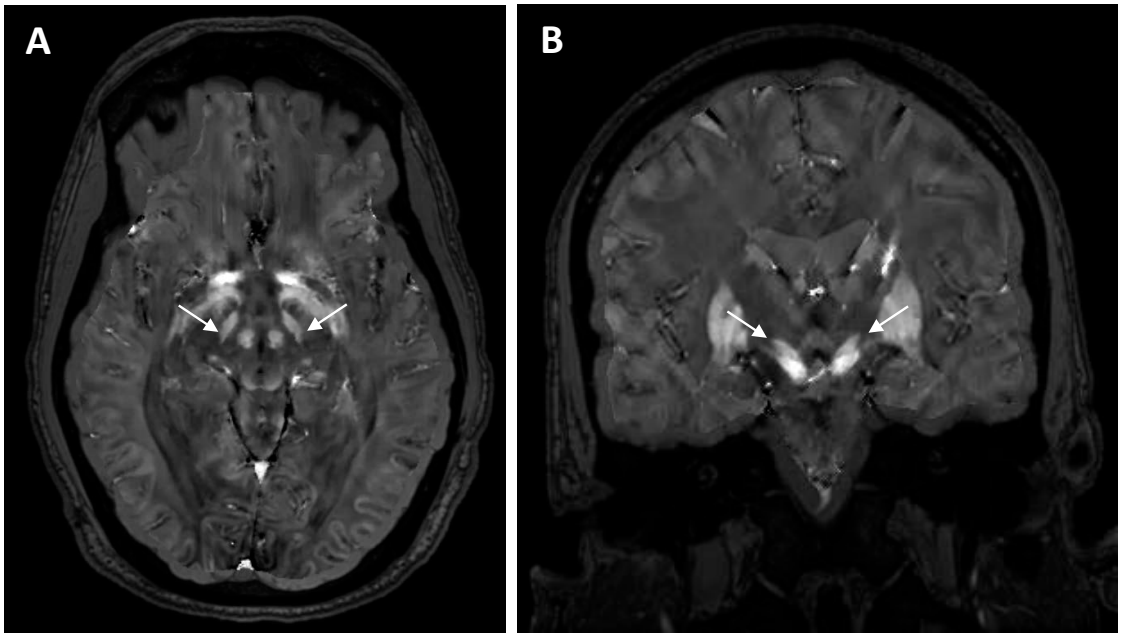

Figure 5.4: QSM of STN (arrows) in axial (A) and coronal (B) planes in a 58 year-old male with PD. QSM provided good spatial definition of STN geometry; ability to differentiate between STN, SN and surrounding white matter; and visualized a decrease in iron towards the dorsolateral portion of the nucleus.

dorsolateral region usually targeted in PD patients due to its correspondence to the sensorimotor area [131–133]. This heterogeneous iron distribution in the STN is blurred on T2w MRI (Fig. 5.3). Fundamentally, T2 shortening is caused by field variance experienced by water protons during diffusion and chemical exchange, as known in the Solomon-Bloembergen-Morgan theory for relaxation enhancement by a paramagnetic substance [50, 134, 135]; field is always blurred as a weighted sum of contributions from all surrounding iron. This blurring in T2w MRI explains the small improvement in STN contrast as T2w imaging resolution increases (Tables and). The blurring in T2w may be worsened in PD patients that have elevated levels of iron in their deep gray matter nuclei [136].

The STN is known to be involved in regulation of limbic, associative, and motor functions [101, 102, 137]. Fibers from functionally distinct cortical areas converge in the STN according to the tripartite model: motor subdivision in the dorsolateral region, associative subdivision the central region, and the limbic subdivision in the medial tip, with functional overlap existing between these three subdivisions [127, 138, 139]. Iron plays a significant role in regulations of glutamate production and secretion, and is an important co-factor for the neurochemistry of these functional regions of the STN [111, 112]. Iron is heterogeneously distributed in STN [121], and strong correlation between iron concentration measured by QSM and densities of axonal passage measured on diffusion tensor imaging has been reported [140]. These understandings of STN function and anatomy are consistent with clinical evidence that the dorsolateral region of the STN that appears to be less paramagnetic compared to the other STN regions may be the optimal site for DBS targeting to avoid negative side effects while maximizing effects on the motor system [106, 141, 142].

QSM can be used to overcome inadequacies of relaxation-based contrasts in T2w MRI [63]. Due to the sensitivity of QSM to the presence of biometals, this technique has been used extensively in studying the iron-rich structures of deep gray matter. Particularly, QSM has been successfully used in STN targeting [131], where its application resulted a single intraoperative MER in over 85% of cases. The comparative analyses of QSM and T2w presented here suggest that susceptibility mapping is better suited for high resolution preoperative STN imaging. QSM can offer better visualization of iron distribution within the STN, providing identification of optimal DBS targeting sites. The qualitative and quantitative results also suggest that QSM unlike T2w benefits from high resolution acquisition, which makes it valuable for accurate segmentation of the

target areas without the need for image interpolation.

High resolution QSM-based estimation of STN dimensions (3×5×12 mm3) agree with histological studies and microelectrode recordings [109,130,143–145]. QSM with sub-millimeter resolution can provide adequate spatial resolution to guide the DBS electrode that is typically 1.3 mm in diameter and 1.5 mm in height. MER is arguably the reference standard for measuring STN dimensions in vivo, but it is invasive and may only provide size along one direction. In contrast, high resolution QSM is noninvasive and provides direct 3D visualization of STN subdivisions. In this study, the comparison between QSM and T2w was limited to healthy volunteers; it was not possible on patient data because T2w MRI had been discarded from the preoperative pre-surgical DBS imaging protocol. Furthermore, raw GRE data was not retained, making it impossible to compare the effects of change in image resolution. For large brain volume coverage in the patient study, increased slice thickness (to 1 mm) at the same scan time was chosen; an alternative option would be to increase scan time while maintaining isotropic acquisition resolution. In summary, high resolution QSM provides better definition of the STN from surrounding tissue and between its sub-regions than traditional T2w MRI. Furthermore, sub-millimeter QSM of the STN may be beneficial in DBS targeting.

CHAPTER 6

CONCLUSIONS AND RECOMMENDATIONS

6.1 Joint estimation of chemical shift and quantitative susceptibility mapping

In this study, a fully automated iterative algorithm for quantitative susceptibility mapping (QSM) within tissues with significant fat content has been presented.

One major improvement to this technique is to incorporate more advanced water/fat separation algorithms. Particularly, presented implementation uses naive initialization of IDEAL solver, where magnitude-guided field unwrapping is utilized. This approach might lead to substantial errors, if areas of low SNR or sharp susceptibility interfaces are present within the region of interest. In order to avoid this, initialization can be done using graph-cut based algorithms such as SPURS [79].

6.2 Bone quantitative susceptibility mapping

This preliminary study has shown that QSM can be used to study bone mineralization level. However, several developments and research extentions are still required to make this technique ready for clinical use.

First, it is necessary to address the main limitation of the UTE sequence - its longer acquisition time (around 13 minutes). This issue can be addressed

if Bayesian MRI data acquisition acceleration strategies are employed [92–96]. Second major improvement would be to incorporate advanced off-resonance correction techniques [97,98] to minimize unwanted image blurring (inherent in radial imaging) due to field inhomogeneity and chemical shift. Third, it might be necessary to optimize acquisition parameters (such as matrix size and image resolution), since it has been shown that QSM is prone to underestimation of strong susceptibility sources [99]. Finally, preconditioned total field inversion [146] can be utilized in order to increase QSM precision in presence of high susceptibility sources such as bone

A future direction of this work can be an investigation of the anisotropic properties of bone, tendon, and cartilage susceptibilities. Although strong magnetic anisotropy in bone and cartilage has been previously reported [54,72,73], it has not been accounted for in the signal model in this preliminary study. The use of a scalar susceptibility model even in the magnetically anisotropic cartilage may contribute to errors in the estimated susceptibility of nearby tissue regions. Continuation of the work should also include studies on larger patient and healthy volunteer cohorts in order to characterize changes in QSM observed in pathological states. Sensitivity of QSM to these changes should be assessed.

6.3 High resolution QSM for STN imaging

The results of this study suggest that contrast in QSM is superior to that of T2w for delineation of the STN with respect to surrounding white matter. Sub-millimeter voxel size QSM faithfully depicts high iron content within the deep gray matter nuclei, allowing for confident localization of borders and observa-

tion of iron content heterogeneity linked to functional subdivisions of the STN.

Major step forward from this work will be establishment of the relation between measured QSM values and MR tractography. In its current state, this project is based on two major empirical findings in DBS: 1) compared to the rest of the STN, its sensimotor subdivision tend to have lower levels of iron concentration [107], and 2) due to the anterolateral location of the sensimotor area [101], this STN part can be viewed as a preferential target in DBS [106,141]. Accordingly, image evaluation was based on the ability of QSM and traditional T2w images to depict changes in iron within the subthalamic nuclei and nuclei border definition. While preliminary work demonstrates improvements associated with QSM-based targeting [131], further research is required for rigorous assessment of QSM's role in DBS planning. Spatial information from QSM, augmented by tractography-derived STN connectivity maps, may provide a neurosurgeon with valuable insights about patient specific "sweetspots".

BIBLIOGRAPHY

[1] Li L, Leigh JS. *Quantifying arbitrary magnetic susceptibility distributions with MR.* Magn Reson Med, 2004;51:1077-1082.

[2] Marques JP, Bowtell R. *Application of a Fourier-based method for rapid calculation of field inhomogeneity due to spatial variation of magnetic susceptibility.* Concepts Magn Reson Part B Magn Reson Eng, 2005;25B:65-78.

[3] Haacke EM, Cheng NY, House MJ, Liu Q, Neelavalli J, Ogg RJ, Khan A, Ayaz M, Kirsch W, Obenaus A. *Imaging iron stores in the brain using magnetic resonance imaging.* Magn Reson Imaging, 2005;23:1-25.

[4] de Rochefort L, Brown R, Prince MR, Wang Y. *Quantitative MR susceptibility mapping using piece-wise constant regularized inversion of the magnetic field.* Magn Reson Med, 2008;60:1003-1009.

[5] Liu T, Spincemaille P, de Rochefort L, Kressler B, Wang Y. *Calculation of susceptibility through multiple orientation sampling (COSMOS): a method for conditioning the inverse problem from measured magnetic field map to susceptibility source image in MRI.* Magn Reson Med, 2009;61:196-204.

[6] Shmueli K, de Zwart JA, van Gelderen P, Li TQ, Dodd SJ, Duyn JH. *Magnetic susceptibility mapping of brain tissue in vivo using MRI phase data.* Magn Reson Med, 2009;62:1510-1522.

[7] Kressler B, de Rochefort L, Liu T, Spincemaille P, Jiang Q, Wang Y. *Nonlinear regularization for per voxel estimation of magnetic susceptibility distributions from MRI field maps.* IEEE Trans Med Imaging, 2010;29:273-281.

[8] Liu J, Liu T, de Rochefort L, et al. *Morphology enabled dipole inversion for quantitative susceptibility mapping using structural consistency between the magnitude image and the susceptibility map.* Neuroimage, 2012;59:2560-2568.

[9] Schweser F, Deistung A, Lehr BW, Reichenbach JR. *Differentiation between diamagnetic and paramagnetic cerebral lesions based on magnetic susceptibility mapping.* Med Phys, 2010;37:5165.

[10] de Rochefort LP, Liu T, Kressler B, Liu J, Spincemaille P, Lebon V, Wu J, Wang Y. *Quantitative susceptibility map reconstruction from MR phase data using bayesian regularization: validation and application to brain imaging.* Magn Reson Med, 2010;63:194-206.

[11] Wharton S, Schafer A, Bowtell R. *Susceptibility mapping in the human brain using threshold-based k-space division.* Magn Reson Med, 2010;63:1292-1304.

[12] Liu T, Liu J, de Rochefort L, Spincemaille P, Khalidov I, Ledoux JR, Wang Y. *Morphology enabled dipole inversion (MEDI) from a single-angle acquisition: comparison with COSMOS in human brain imaging.* Magn Reson Med, 2011;66:777-783.

[13] Schweser F, Deistung A, Lehr BW, Reichenbach JR. *Quantitative imaging of intrinsic magnetic tissue properties using MRI signal phase: an approach to in vivo brain iron metabolism?* Neuroimage, 2011;54:2789-2807.

[14] Li W, Wu B, Liu CL. *Quantitative susceptibility mapping of human brain reflects spatial variation in tissue composition.* Neuroimage, 2011;55:1645-1656.

[15] Liu CL. *Susceptibility tensor imaging.* Magn Reson Imaging, 2010;63:1471-1477.

[16] Liu T, Spincemaille P, de Rochefort L, Wong R, Prince M, Wang Y. *Unambiguous identification of superparamagnetic iron oxide particles through quantitative susceptibility mapping of the nonlinear response to magnetic fields.* Magn Reson Imaging, 2010;28:1383-1389.

[17] Ropele S, de Graaf W, Khalil M, et al. *MRI Assessment of iron deposition in multiple sclerosis.* J Magn Reson Imaging, 2011;34:13-21.

[18] Bilgic B, Pfefferbaum A, Rohlfing T, Sullivan EV, Adalsteinsson E. *MRI estimates of brain iron concentration in normal aging using quantitative susceptibility mapping.* Neuroimage, 2012;59:2625-2635.

[19] Liu T, Surapaneni K, Lou M, Cheng LQ, Spincemaille P, Wang Y. *Cerebral microbleeds: burden assessment by using quantitative susceptibility mapping.* Radiology, 2012;262:269-278.

[20] Langkammer C, Schweser F, Krebs N, et al. *Quantitative susceptibility mapping (QSM) as a means to measure brain iron? A post mortem validation study.* Neuroimage, 2012;62:1593-1599.

[21] Deistung A, Schafer A, Schweser F, Biedermann U, Turner R, Reichenbach JR. *Toward in vivo histology: a comparison of quantitative susceptibility map-*

ping (QSM) with magnitude-, phase-, and R2-imaging at ultra-high magnetic field strength.* Neuroimage, 2013;65:299-314.

[22] Wisnieff C, Liu T, Spincemaille P, Wang S, Zhou D, Wang Y. *Magnetic susceptibility anisotropy: cylindrical symmetry from macroscopically ordered anisotropic molecules and accuracy of MRI measurements using few orientations.* Neuroimage, 2013;70:363-376.

[23] Langkammer C, Liu T, Khalil M, Enzinger C, Jehna M, Fuchs S, Fazekas F, Wang Y, Ropele S. *Quantitative susceptibility mapping in multiple sclerosis.* Radiology, 2013;267:551-559.

[24] Li W, Wu B, Avram AV, Liu CL. *Magnetic susceptibility anisotropy of human brain in vivo and its molecular underpinnings.* Neuroimage, 2012;59:2088-2097.

[25] Haacke EM, Ye Y. *The role of susceptibility weighted imaging in functional MRI.* Neuroimage, 2012;62:923-929.

[26] Reichenbach JR, Venkatesan R, Schillinger DJ, Kido DK, Haacke EM. *Small vessels in the human brain: MR venography with deoxyhemoglobin as an intrinsic contrast agent.* Radiology, 1997;204:272-277.

[27] Lamb WE. *Internal diamagnetic fields.* Phys Rev, 1941;60:817-819.

[28] Ramsey NF. *Magnetic shielding of nuclei in molecules.* Phys Rev, 1950;78:699-703.

[29] Schindler M, Kutzelnigg W. *Theory of magnetic-susceptibilities and NMR chemical-shifts in terms of localized quantities. 3. Application to hydrocarbons and other organic-molecules.* J Am Chem Soc, 1983;105:1360-1370.

[30] Gadian DG. *Nuclear magnetic resonance and its applications to living systems.* New York: Oxford University Press, 1982. x, 197 p.

[31] Reeder SB, Wen ZF, Yu HZ, Pineda AR, Gold GE, Markl M, Pelc NJ. *Multi-coil Dixon chemical species separation with an iterative least-squares estimation method.* Magn Reson Med, 2004;51:35-45.

[32] Yu H, McKenzie CA, Shimakawa A, Vu AT, Brau AC, Beatty PJ, Pineda AR, Brittain JH, Reeder SB. *Multiecho reconstruction for simultaneous water-*

fat decomposition and T2 estimation.* J Magn Reson Imaging, 2007;26:1153-1161.

[33] Schick F, Eismann B, Jung WI, Bongers H, Bunse M, Lutz O. *Comparison of localized proton NMR signals of skeletal muscle and fat tissue in vivo: two lipid compartments in muscle tissue.* Magn Reson Med, 1993;29:158-167.

[34] Barany M, Venkatasubramanian PN, Mok E, Siegel IM, Abraham E, Wycliffe ND, Mafee MF. *Quantitative and qualitative fat analysis in human leg muscle of neuromuscular diseases by 1H MR spectroscopy in vivo.* Magn Reson Med, 1989;10:210-226.

[35] Hernando D, Liang ZP, Kellman P. *Chemical shift-based water/fat separation: a comparison of signal models.* Magn Reson Med, 2010;64:811-822.

[36] Yu H, Shimakawa A, McKenzie CA, Brodsky E, Brittain JH, Reeder SB. *Multiecho water-fat separation and simultaneous R2* estimation with multifrequency fat spectrum modeling.* Magn Reson Med, 2008;60:1122-1134.

[37] Hernando D, Kellman P, Haldar JP, Liang ZP. *Robust water/fat separation in the presence of large field inhomogeneities using a graph cut algorithm.* Magn Reson Med, 2010;63:79-90.

[38] Hernando D, Sharma SD, Kramer H, Reeder SB. *On the confounding effect of temperature on chemical shift-encoded fat quantification.* Magn Reson Med, 2014;72:464-470.

[39] Funai AK, Fessler JA, Yeo DTB, Olafsson VT, Noll DC. *Regularized field map estimation in MRI.* IEEE transactions on medical imaging, 2008;27:1484-1494.

[40] Dixon WT. *Simple proton spectroscopic imaging.* Radiology, 1984;153:189-194.

[41] Salomir R, de Senneville BD, Moonen CTW. *A fast calculation method for magnetic field inhomogeneity due to an arbitrary distribution of bulk susceptibility.* Concepts Magn Reson, 2003;19B:26-34.

[42] Jackson JD. *Classical electrodynamics.* New York: Wiley, 1999. xxi, 808 p.

[43] Morozov VA. *Solution of functional equations by regularization method.* Dokl Akad Nauk SSSR, 1966;167:510.

[44] Liu T, Khalidov I, de Rochefort L, Spincemaille P, Liu J, Tsiouris AJ, Wang Y. *A novel background field removal method for MRI using projection onto dipole fields (PDF).* NMR Biomed, 2011;24:1129-1136.

[45] Liu T, Wisnieff C, Lou M, Chen W, Spincemaille P, Wang Y. *Nonlinear formulation of the magnetic field to source relationship for robust quantitative susceptibility mapping.* Magn Reson Med, 2013;69:467-476.

[46] de Rochefort L, Nguyen T, Brown R, Spincemaille P, Choi G, Weinsaft J, Prince MR, Wang Y. *In vivo quantification of contrast agent concentration using the induced magnetic field for time-resolved arterial input function measurement with MRI.* Med Phys, 2008;35:5328-5339.

[47] Szczepaniak LS, Dobbins RL, Stein DT, McGarry JD. *Bulk magnetic susceptibility effects on the assessment of intra- and extramyocellular lipids in vivo.* Magn Reson Med, 2002;47:607-610.

[48] Boesch C, Slotboom J, Hoppeler H, Kreis R. *In vivo determination of intramyocellular lipids in human muscle by means of localized 1H-MR-spectroscopy.* Magn Reson Med, 1997;37:484-493.

[49] Pineda AR, Reeder SB, Wen Z, Pelc NJ. *Cramer-Rao bounds for three-point decomposition of water and fat.* Magn Reson Med, 2005;54:625-635.

[50] Wang Y. *Principles of Magnetic Resonance Imaging: Physics Concepts, Pulse Sequences, & Biomedical Applications.* CreateSpace Independent Publishing Platform, 2012.

[51] Chen W, Zhu W, Kovanlikaya I, Kovanlikaya A, Liu T, Wang S, Salustri C, Wang Y. *Intracranial calcifications and hemorrhages: characterization with quantitative susceptibility mapping.* Radiology, 2014;270:496-505.

[52] Buch S, Liu S, Ye Y, Cheng YC, Neelavalli J, Haacke EM. *Susceptibility mapping of air, bone, and calcium in the head.* Magn Reson Med, 2015;73:2185-2194.

[53] Deistung A, Schweser F, Wiestler B, et al. *Quantitative susceptibility mapping differentiates between blood depositions and calcifications in patients with glioblastoma.* PloS One, 2013;8:e57924.

[54] Hwang SN, Wehrli FW. *The calculation of the susceptibility-induced magnetic-*

field from 3D NMR images with applications to trabecular bone. J Magn Reson Ser B, 1995;109:126-145.

[55] Hopkins JA, Wehrli FW. *Magnetic susceptibility measurement of insoluble solids by NMR: magnetic susceptibility of bone.* Magn Reson Med, 1997;37:494-500.

[56] Hwang SN, Wehrli FW, Chung HW. *Experimental validation of theoretical field maps in human trabecular bone.* Proceedings of the 4th Annual Meeting of ISMRM, New York, NY, 1996. p. 1371.

[57] Wang Y, Liu T. *Quantitative susceptibility mapping (QSM): decoding MRI data for a tissue magnetic biomarker.* Magn Reson Med, 2015;73:82-101.

[58] Bilgic B, Fan AP, Polimeni JR, Cauley SF, Bianciardi M, Adalsteinsson E, Wald LL, Setsompop K. *Fast quantitative susceptibility mapping with l1-regularization and automatic parameter selection.* Magn Reson Med, 2014;72:1444-1459.

[59] Liu CL, Li W, Tong KA, Yeom KW, Kuzminski S. *Susceptibility-weighted imaging and quantitative susceptibility mapping in the brain.* J Magn Reson Imaging, 2015;42:23-41.

[60] Chen W, Gauthier SA, Gupta A, Comunale J, Liu T, Wang S, Pei M, Pitt D, Wang Y. *Quantitative susceptibility mapping of multiple sclerosis lesions at various ages.* Radiology, 2014;271:183-192.

[61] Xu B, Liu T, Spincemaille P, Prince M, Wang Y. *Flow compensated quantitative susceptibility mapping for venous oxygenation imaging.* Magn Reson Med, 2014;72:438-445.

[62] Wisnieff C, Ramanan S, Olesik J, Gauthier S, Wang Y, Pitt D. *Quantitative susceptibility mapping (QSM) of white matter multiple sclerosis lesions: interpreting positive susceptibility and the presence of iron.* Magn Reson Med, 2015;74:564-570.

[63] Liu T, Eskreis-Winkler S, Schweitzer AD, Chen W, Kaplitt MG, Tsiouris AJ, Wang Y. *Improved subthalamic nucleus depiction with quantitative susceptibility mapping.* Radiology, 2013;269:216-223.

[64] Deistung A, Schweser F, Reichenbach JR. *Overview of quantitative susceptibility mapping.* NMR Biomed, 2016. doi: 10.1002/nbm.3569.

[65] Link TM. *Radiology of osteoporosis.* Can Assoc Radiol J, 2016;67:28-40.

[66] Wehrli FW, Song HK, Saha PK, Wright AC. *Quantitative MRI for the assessment of bone structure and function.* NMR Biomed, 2006;19:731-764.

[67] Du J, Hermida JC, Diaz E, Corbeil J, Znamirowski R, D'Lima DD, Bydder GM. *Assessment of cortical bone with clinical and ultrashort echo time sequences.* Magn Reson Med, 2013;70:697-704.

[68] Khalidov I, Liu T, Prince MR, Wang Y. *Susceptibility mapping: computation of the field map using water-fat separation at 7T.* Proceedings of the 19th Annual Meeting of ISMRM, Montreal, QC, Canada, 2011. p. 4475.

[69] Dimov AV, Liu Z, Spincemaille P, Du J, Wang Y. *Quantitative susceptibility mapping of bone using ultra-short TE sequence.* Proceedings of the 23th Annual Meeting of ISMRM, Toronto, ON, Canada, 2015. p. 938.

[70] Nissi MJ, Toth F, Wang LN, Carlson CS, Ellermann JM. *Improved visualization of cartilage canals using quantitative susceptibility mapping.* PloS One, 2015;10:e0132167.

[71] Wang L, Nissi MJ, Toth F, Johnson CP, Garwood M, Carlson CS, Ellermann J. *Quantitative susceptibility mapping detects abnormalities in cartilage canals in a goat model of preclinical osteochondritis dissecans.* Magn Reson Med, 2016. doi: 10.1002/mrm.26214.

[72] Wei H, Wang B, Zong X, Lin W, Wang N, Liu C. *Imaging magnetic susceptibility of the human knee joint at 3 and 7 Tesla.* Proceedings of the 23th Annual Meeting of ISMRM, Toronto, ON, Canada, 2015. p. 288.

[73] Wei H, Dibb R, Decker K, Wang N, Zhang Y, Zong X, Lin W, Nissman DB, Liu C. *Investigating magnetic susceptibility of human knee joint at 7 Tesla.* Magn Reson Med, 2017. doi: 10.1002/mrm.26596.

[74] Du J, Bydder M, Takahashi AM, Carl M, Chung CB, Bydder GM. *Short T2 contrast with three-dimensional ultrashort echo time imaging.* Magn Reson Imaging, 2011;29:470-482.

[75] Rahmer J, Bornert P, Groen J, Bos C. *Three-dimensional radial ultrashort echo-time imaging with T_2 adapted sampling.* Magn Reson Med, 2006;55:1075-1082.

[76] Jackson JI, Meyer CH, Nishimura DG, Macovski A. *Selection of a convolution function for fourier inversion using gridding.* IEEE Trans Med Imaging, 1991;10:473-478.

[77] Fessler JA, Sutton BP. *Nonuniform fast Fourier transforms using min-max interpolation.* IEEE Trans Signal Proces, 2003;51(2):560-574.

[78] Rasche V, Proksa R, Sinkus R, Bornert P, Eggers H. *Resampling of data between arbitrary grids using convolution interpolation.* IEEE Trans Med Imaging, 1999;18:385-392.

[79] Dong JW, Liu T, Chen F, Zhou D, Dimov A, Raj A, Cheng Q, Spincemaille P, Wang Y. *Simultaneous phase unwrapping and removal of chemical shift (SPURS) using graph cuts: application in quantitative susceptibility mapping.* IEEE Trans Med Imaging, 2015;34:531-540.

[80] Pei MC, Nguyen TD, Thimmappa ND, Salustri C, Dong F, Cooper MA, Li JQ, Prince MR, Wang Y. *Algorithm for fast monoexponential fitting based on auto-regression on linear operations (ARLO) of data.* Magn Reson Med, 2015;73:843-850.

[81] Smith SM, Jenkinson M, Woolrich MW, et al. *Advances in functional and structural MR image analysis and implementation as FSL.* NeuroImage, 2004;23:S208-S219.

[82] Biswas R, Bae W, Diaz E, Masuda K, Chung CB, Bydder GM, Du J. *Ultrashort echo time (UTE) imaging with bi-component analysis: bound and free water evaluation of bovine cortical bone subject to sequential drying.* Bone, 2012;50:749-755.

[83] Diefenbach MN, Van AT, Meineke J, Kooijman H, Haase A, Rummeny EJ, Kirschke JS, Baum T, Karampinos DC. *On the feasibility of quantitative susceptibility mapping for trabecular bone volume density mapping at 3T.* Proceedings of the 24th Annual Meeting of ISMRM, Singapore, 2016. p. 677.

[84] *Assessment of fracture risk and its application to screening for postmenopausal osteoporosis. Report of a WHO study group.* World Health Organ Tech Rep Ser, 1994;843:1-129.

[85] Kanis JA. *Diagnosis of osteoporosis and assessment of fracture risk.* Lancet, 2002;359:1929-1936.

[86] Langton CM, Njeh CF. *Acoustic and ultrasonic tissue characterizationassessment of osteoporosis.* Proc Inst Mech Eng H, 1999;213:261-269.

[87] Wiesinger F, Sacolick LI, Menini A, Kaushik SS, Ahn S, Veit-Haibach P, Delso G, Shanbhag DD. *Zero TE MR bone imaging in the head.* Magn Reson Med, 2016;75:107-114.

[88] Weiger M, Pruessmann KP, Bracher AK, Kohler S, Lehmann V, Wolfram U, Hennel F, Rasche V. *High-resolution ZTE imaging of human teeth.* NMR Biomed, 2012;25:1144-1151.

[89] Weiger M, Wu MM, Wurnig MC, Kenkel D, Boss A, Andreisek G, Pruessmann KP. *ZTE imaging with long-T_2 suppression.* NMR Biomed, 2015;28:247-254.

[90] Idiyatullin D, Corum C, Park JY, Garwood M. *Fast and quiet MRI using a swept radiofrequency.* J Magn Reson, 2006;181:342-349.

[91] Li C, Magland JF, Zhao X, Seifert AC, Wehrli FW. *Selective in vivo bone imaging with long-T_2 suppressed PETRA MRI.* Magn Reson Med, 2016. doi: 10.1002/mrm.26178.

[92] Pruessmann KP, Weiger M, Scheidegger MB, Boesiger P. *SENSE: sensitivity encoding for fast MRI.* Magn Reson Med, 1999;42:952-962.

[93] Griswold MA, Jakob PM, Heidemann RM, Nittka M, Jellus V, Wang JM, Kiefer B, Haase A. *Generalized autocalibrating partially parallel acquisitions (GRAPPA).* Magn Reson Med, 2002;47:1202-1210.

[94] Codella NCF, Spincemaille P, Prince M, Wang Y. *A radial self-calibrated (RASCAL) generalized autocalibrating partially parallel acquisition (GRAPPA) method using weight interpolation.* NMR Biomed, 2011;24:844-854.

[95] Sodickson DK, Manning WJ. *Simultaneous acquisition of spatial harmonics (SMASH): fast imaging with radiofrequency coil arrays.* Magn Reson Med, 1997;38:591-603.

[96] Pruessmann KP, Weiger M, Bornert P, Boesiger P. *Advances in sensitivity encoding with arbitrary k-space trajectories.* Magn Reson Med, 2001;46:638-651.

[97] Brodsky EK, Holmes JH, Yu HZ, Reeder SB. *Generalized k-space decomposition with chemical shift correction for non-cartesian water-fat imaging.* Magn Reson Med, 2008;59:1151-1164.

[98] Moriguchi H, Lewin JS, Duerk JL. *Dixon techniques in spiral trajectories with off resonance correction: a new approach for fat signal suppression without spatial-spectral RF pulses.* Magn Reson Med, 2003;50:915-924.

[99] Zhou D, Cho J, Zhang J, Spinsmaille P, Wang Y. *Susceptibility underestimation in a high-susceptibility phantom: Dependence on imaging resolution, magnitude contrast, and other parameters.* Magn Reson Med, 2017;78:1080-1086.

[100] de Rochefort L, Brown R, Prince MR, Wang Y. *Bone susceptibility quantification: in vivo feasibility with MR source quantification by inverting the dipole field.* Proceedings of the 16th Annual Meeting of ISMRM, Toronto, ON, Canada, 2008. p. 540.

[101] Haynes WI, Haber SN. *The organization of prefrontal-subthalamic inputs in primates provides an anatomical substrate for both functional specificity and integration: implications for Basal Ganglia models and deep brain stimulation.* J Neurosci, 2013;33:4804-4814.

[102] Lambert C, Zrinzo L, Nagy Z, Lutti A, Hariz M, Foltynie T, et al. *Confirmation of functional zones within the human subthalamic nucleus: patterns of connectivity and sub-parcellation using diffusion weighted imaging.* Neuroimage, 2012;60:83-94.

[103] Benabid AL, Chabardes S, Mitrofanis J, Pollak P. *Deep brain stimulation of the subthalamic nucleus for the treatment of Parkinson's disease.* Lancet Neurol, 2009;8:67-81.

[104] Deep-Brain Stimulation for Parkinson's Disease Study Group. *Deep-brain stimulation of the subthalamic nucleus or the pars interna of the globus pallidus in Parkinson's disease.* N Engl J Med, 2001;345:956-963.

[105] Wichmann T, Delong MR. *Deep brain stimulation for neurologic and neuropsychiatric disorders.* Neuron, 2006;72:494-506.

[106] Wodarg F, Herzog J, Reese R, Falk D, Pinsker MO, Steigerwald F, et al. *Stimulation site within the MRI-defined STN predicts postoperative motor outcome.* Movement Disorders, 2012;27:874-879.

[107] Dormont D, Ricciardi KG, Tande D, Parain K, Menuel C, Galanaud D, et al. *Is the subthalamic nucleus hypointense on T2-weighted images? A correlation study using MR imaging and stereotactic atlas data.* American Journal of Neuroradiology, 2004;25:1516-1523.

[108] Kerl HU, Gerigk L, Pechlivanis I, Al-Zghloul M, Groden C, Nolte I. *The subthalamic nucleus at 3.0 Tesla: choice of optimal sequence and orientation for deep brain stimulation using a standard installation protocol.* Journal of Neurosurgery, 2012;117:1155-1165.

[109] Massey LA, Miranda MA, Zrinzo L, Al-Helli O, Parkes HG, Thornton JS, et al. *High resolution MR anatomy of the subthalamic nucleus: imaging at 9.4 T with histological validation.* Neuroimage, 2012;59:2035-2044.

[110] Richter EO, Hoque T, Halliday W, Lozano AM, Saint-Cyr JA. *Determining the position and size of the subthalamic nucleus based on magnetic resonance imaging results in patients with advanced Parkinson disease.* Journal of Neurosurgery, 2004;100:541-546.

[111] Abbruzzese G, Cossu G, Balocco M, Marchese R, Murgia D, Melis M, et al. *A pilot trial of deferiprone for neurodegeneration with brain iron accumulation.* Haematologica, 2011;96:1708-1711.

[112] McGahan MC, Harned J, Mukunnemkeril M, Goralska M, Fleisher L, Ferrell JB. *Iron alters glutamate secretion by regulating cytosolic aconitase activity.* Am J Physiol Cell Physiol, 2005;288:C1117-1124.

[113] Wang Y, Spincemaille P, Liu Z, Dimov A, Deh K, Li J, et al. *Clinical quantitative susceptibility mapping (QSM): Biometal imaging and its emerging roles in patient care.* Magn Reson Imaging, 2017.

[114] Bejjani BP, Dormont D, Pidoux B, Yelnik J, Damier P, Arnulf I, et al. *Bilateral subthalamic stimulation for Parkinson's disease by using three-dimensional stereotactic magnetic resonance imaging and electrophysiological guidance.* Journal of Neurosurgery, 2000;92:615-625.

[115] Lemaire JJ, Coste J, Ouchchane L, Caire F, Nuti C, Derost P, et al. *Brain mapping in stereotactic surgery: A brief overview from the probabilistic targeting to the patient-based anatomic mapping.* Neuroimage, 2007;37:S109-S115.

[116] Longhi M, Ricciardi G, Tommasi G, Nicolato A, Foroni R, Bertolasi L, et al. *The Role of 3T Magnetic Resonance Imaging for Targeting the Human Subthala-*

mic Nucleus in Deep Brain Stimulation for Parkinson Disease. Journal of Neurological Surgery Part A - Central European Neurosurgery, 2015;76:181-189.

[117] Li J, Chang S, Liu T, Wang Q, Cui D, Chen X, et al. *Reducing the object orientation dependence of susceptibility effects in gradient echo MRI through quantitative susceptibility mapping.* Magn Reson Med, 2012;68:1563-1569.

[118] Alkemade A, de Hollander G, Keuken MC, Schafer A, Ott DVM, Schwarz J, et al. *Comparison of T2*-weighted and QSM contrasts in Parkinson's disease to visualize the STN with MRI.* PLoS One, 2017;12:e0176130.

[119] Chandran AS, Bynevelt M, Lind CR. *Magnetic resonance imaging of the subthalamic nucleus for deep brain stimulation.* Journal of Neurosurgery, 2016;124:96-105.

[120] de Hollander G, Keuken MC, Bazin PL, Weiss M, Neumann J, Reimann K, et al. *A Gradual Increase of Iron Toward the Medial-Inferior Tip of the Subthalamic Nucleus.* Human Brain Mapping, 2014;35:4440-4449.

[121] Schafer A, Forstmann BU, Neumann J, Wharton S, Mietke A, Bowtell R, et al. *Direct visualization of the subthalamic nucleus and its iron distribution using high-resolution susceptibility mapping.* Human Brain Mapping, 2012;33:2831-2842.

[122] Yushkevich PA, Piven J, Hazlett HC, Smith RG, Ho S, Gee JC, et al. *User-guided 3D active contour segmentation of anatomical structures: Significantly improved efficiency and reliability.* Neuroimage, 2006;31:1116-1128.

[123] Andrade-Souza YM, Schwalb JM, Hamani C, Hoque T, Saint-Cyr J, Lozano AM. *Comparison of T2*-weighted and QSM contrasts in Parkinson's disease to visualize the STN with MRI.* Surgical Neurology, 2005;63:357-362.

[124] Dormont D, Seidenwurm D, Galanaud D, Cornu P, Yelnik J, Bardinet E. *Neuroimaging and Deep Brain Stimulation.* American Journal of Neuroradiology, 2010;31:15-23.

[125] Schlaier J, Schoedel P, Lange M, Winkler J, Warnat J, Dorenbeck U, et al. *Reliability of atlas-derived coordinates in deep brain stimulation.* Acta Neurochirurgica, 2005;147:1175-1180.

[126] Cuny E, Guehl D, Burbaud P, Gross C, Dousset V, Rougier A. *Lack of*

agreement between direct magnetic resonance imaging and statistical determination of a subthalamic target: the role of electrophysiological guidance. Journal of Neurosurgery, 2002;97:591-597.

[127] Hamani C, Richter EO, Andrade-Souza Y, Hutchison W, Saint-Cyr JA, Lozano AM. *Correspondence of microelectrode mapping with magnetic resonance imaging for subthalamic nucleus procedures.* Surgical Neurology, 2005;63:249-253.

[128] Polanski WH, Martin KD, Engellandt K, von Kummer R, Klingelhoefer L, Fauser M, et al. *Accuracy of subthalamic nucleus targeting by T2, FLAIR and SWI-3-Tesla MRI confirmed by microelectrode recordings.* Acta Neurochirurgica, 2015;157:479-486.

[129] Schlaier JR, Habermeyer C, Warnat J, Lange M, Janzen A, Hochreiter A, et al. *Discrepancies between the MRI- and the electrophysiologically defined subthalamic nucleus.* Acta Neurochirurgica, 2011;153:2307-2318.

[130] Verhagen R, Schuurman PR, van den Munckhof P, Contarino MF, de Bie RMA, Bour LJ. *Comparative study of microelectrode recording-based STN location and MRI-based STN location in low to ultra-high field (7.0T) T2-weigthed MRI images.* Journal of Neural Engineering, 2016;13 066009.

[131] Rasouli J, Ramdhani R, Panov FE, Dimov A, Zhang Y, Cho C, et al. *Utilization of Quantitative Susceptibility Mapping for Direct Targeting of the Subthalamic Nucleus During Deep Brain Stimulation Surgery.* Operative Neurosurgery, 2017.

[132] Rodriguez-Oroz MC, Rodriguez M, Guridi J, Mewes K, Chockkman V, Vitek J, et al. *The subthalamic nucleus in Parkinson's disease: somatotopic organization and physiological characteristics.* Brain, 2001;124:1777-1790.

[133] Theodosopoulos PV, Marks WJ, Christine C, Starr PA. *Locations of movement-related cells in the human. subthalamic nucleus in Parkinson's disease.* Movement Disorders, 2003;18:791-798.

[134] Bloembergen N, Morgan LO. *Proton relaxation times in paramagetic solutions. Effects of electron spin relaxation.* J. Chem. Phys., 2000;34:8.

[135] Solomon I. *Relaxation processes in a system of two spins.* Physical Review, 1955;99:559-565.

[136] Dexter DT, Carayon A, Javoy-Agid F, Agid Y, Wells FR, Daniel SE, et al. *Alterations in the levels of iron, ferritin and other trace metals in Parkinson's disease and other neurodegenerative diseases affecting the basal ganglia.* Brain, 1991;114:1953-1975.

[137] Wichmann T, Bergman H, Delong MR. *The Primate Subthalamic Nucleus (1): Functional-Properties in Intact Animals.* Journal of Neurophysiology, 1994;72:494-506.

[138] Aravamuthan BR, Muthusamy KA, Stein JF, Aziz TZ, Johansen-Berg H. *Topography of cortical and subcortical connections of the human pedunculopontine and subthalamic nuclei.* Neuroimage, 2007;37:694-705.

[139] Nambu A, Tokuno H, Inase M, Takada M. *Corticosubthalamic input zones from forelimb representations of the dorsal and ventral divisions of the premotor cortex in the macaque monkey: comparison with the input zones from the primary motor cortex and the supplementary motor area.* Neuroscience Letters, 1997;239:13-16.

[140] Patel W, Dimov A, Wang Y, Yao Y, Kopell BH, O'Halloran R. *Is iron concentration linked to structural connectivity in the subrhalamic nucleus? Implications for planning of deep brain stimulation.* Proceedings of the 25th Annual Meeting of ISMRM, Honolulu, HI, 2017, p 5277.

[141] Akram H, Sotiropoulos SN, Jbabdi S, Georgiev D, Mahlknecht P, Hyam J, et al. *Subthalamic deep brain stimulation sweet spots and hyperdirect cortical connectivity in Parkinson's disease.* Neuroimage, 2017;158:332-345.

[142] Bronstein JM, Tagliati M, Alterman RL, Lozano AM, Volkmann J, Stefani A, et al. *Deep brain stimulation for Parkinson disease: an expert consensus and review of key issues.* Arch Neurol, 2011;68:165.

[143] Bubnov AN. *[Individual anatomic variability of the subthalamic nucleus in frontal sections].* Arkh Anat Gistol Embriol, 1975;68:85-87.

[144] Mavridis I, Boviatsis E, Anagnostopoulou S. *Anatomy of the Human Subthalamic Nucleus: A Combined Morphometric Study*. Anatomy Research International, 2013;2013:8.

[145] Yelnik J, Percheron G. *Subthalamic neurons in primates: A quantitative and comparative analysis.* Neuroscience, 1979;4:1717-1743.

[146] Liu Z, Kee Y, Zhou D, Wang Y, Spincemaille P. *Preconditioned total field inversion (TFI) method for quantitative susceptibility mapping*. Magn Reson Med, 2017;78:303-315.